

Jordan Journal of Mechanical and Industrial Engineering (JJMIE)

JJMIE is a high-quality scientific journal devoted to fields of Mechanical and Industrial Engineering. It is published by Hashemite University in cooperation with the Jordanian Scientific Research and Innovation Support Fund, Ministry of Higher Education and Scientific Research.

EDITORIAL BOARD

Editor-in-Chief

Prof. Moh'd Sami Ashhab

Assistant Editors

Dr. Ahmad AlMigdady

Dr. Mohammad Jreissat

Editorial Board

Prof. Tariq A. ALAzab

Al Balqa Applied University

Prof. Jamal Jaber

Al- Balqa Applied University

Prof. Mohamad Al-Widyan

Jordan University of Science and Technology

Prof. Mohammed Taiseer Hayajneh

Jordan University of Science and Technology

Prof. Mohammad Al-Tahat

The University of Jordan

Dr. Ali M. Jawarneh

The Hashemite University

THE INTERNATIONAL ADVISORY BOARD

Abu-Qudais, Mohammad

Jordan University of Science & Technology, Jordan

Tzou, Gow-Yi

Yung-Ta Institute of Technology and Commerce, Taiwan

Abu-Mulaweh, Hosni

Purdue University at Fort Wayne, USA

Jubran, Bassam

Ryerson University, Canada

Afaneh Abdul-Hafiz

Robert Bosch Corporation, USA

Kakac, Sadik

University of Miami, USA

Afonso, Maria Dina

Institute Superior Tecnico, Portugal

Khalil, Essam-Eddin

Cairo University, Egypt

Badiru, Adedji B.

The University of Tennessee, USA

Mutoh, Yoshiharu

Nagaoka University of Technology, Japan

Bejan, Adrian

Duke University, USA

Pant, Durbin

Iowa State University, USA

Chalhoub, Nabil G.

Wayne State University, USA

Riffat, Saffa

The University of Nottingham, U. K

Cho, Kyu-Kab

Pusan National University, South Korea

Saghir, Ziad

Ryerson University, Canada

Dincer, Ibrahim

University of Ontario Institute of Technology,
Canada

Sarkar, MD. Abdur Rashid

Bangladesh University of Engineering &
Technology, Bangladesh

Douglas, Roy

Queen's University, U. K

Siginer, Dennis

Wichita State University, USA

El Bassam, Nasir

International Research Center for Renewable
Energy, Germany

Sopian, Kamaruzzaman

University Kebangsaan Malaysia, Malaysia

Haik, Yousef

United Arab Emirates University, UAE

EDITORIAL BOARD SUPPORT TEAM

Language Editor

Dr. Baker M. Bani-khair

Publishing Layout

Eng. Ali Abu Salimeh

SUBMISSION ADDRESS:

Prof. Moh'd Sami Ashhab, Editor-in-Chief
Jordan Journal of Mechanical & Industrial Engineering,
Hashemite University,
PO Box 330127, Zarqa, 13133, Jordan
E-mail: jjmie@hu.edu.jo



Hashemite Kingdom of Jordan



Hashemite University

Jordan Journal of
Mechanical and Industrial Engineering

JJMIE

An International Peer-Reviewed Scientific Journal
Financed by Scientific Research Support Fund

<http://jjmie.hu.edu.jo/>

ISSN 1995-6665

Jordan Journal of Mechanical and Industrial Engineering (JJMIE)

JJMIE is a high-quality scientific journal devoted to fields of Mechanical and Industrial Engineering. It is published by The Jordanian Ministry of Higher Education and Scientific Research in cooperation with Hashemite University.

Introduction: The Editorial Board is very committed to build the Journal as one of the leading international journals in mechanical and industrial engineering sciences in the next few years. With the support of the Ministry of Higher Education and Scientific Research and Jordanian Universities, it is expected that a heavy resource to be channeled into the Journal to establish its international reputation. The Journal's reputation will be enhanced from arrangements with several organizers of international conferences in publishing selected best papers of the conference proceedings.

Aims and Scope: *Jordan Journal of Mechanical and Industrial Engineering (JJMIE)* is a refereed international journal to be of interest and use to all those concerned with research in various fields of, or closely related to, mechanical and industrial engineering disciplines. *Jordan Journal of Mechanical and Industrial Engineering* aims to provide a highly readable and valuable addition to the literature which will serve as an indispensable reference tool for years to come. The coverage of the journal includes all new theoretical and experimental findings in the fields of mechanical and industrial engineering or any closely related fields (Materials, Manufacturing, Management, Design, Thermal and Fluid, Energy, Control, Mechatronics, and Biomedical). The journal also encourages the submission of critical review articles covering advances in recent research of such fields as well as technical notes.

Guide for Authors

Manuscript Submission:

High-quality submissions to this new journal are welcome now and manuscripts may be either submitted online or email.

Online: For online and email submission upload one copy of the full paper including graphics and all figures at the online submission site, accessed via <http://jjmie.hu.edu.jo>. The manuscript must be written in MS Word 2010 Format. All correspondence, including notification of the Editor's decision and requests for revision, takes place by e-mail and via the Author's homepage, removing the need for a hard-copy paper trail.

Submission address and contact:

Prof. Moh'd Sami Ashhab
Editor-in-Chief
*Jordan Journal of Mechanical & Industrial
Engineering*, Hashemite University
PO Box 330127, Zarqa, 13115, Jordan
E-mail: jjmie@hu.edu.jo

Types of contributions: Original research papers and Technical reports

Corresponding author: Clearly indicate who is responsible for correspondence at all stages of refereeing and publication, including post-publication. Ensure that telephone and fax numbers (with country and area code) are provided in addition to the e-mail address and the complete postal address. Full postal addresses must be given for all co-authors.

Original material: Submission of an article implies that the work described has not been published previously (except in the form of an abstract or as part of a published lecture or academic thesis), that it is not under consideration for publication elsewhere, that its publication is approved by all authors and that, if accepted, it will not be published elsewhere in the same form, in English or in any other language, without the written consent of the Publisher. Authors found to be deliberately contravening the submission guidelines on originality and exclusivity shall not be considered for future publication in this journal.

Withdrawing: If the author chooses to withdraw his article after it has been assessed, he shall reimburse JJMIE with the cost of reviewing the paper.

Manuscript Preparation:

General: Editors reserve the right to adjust style to certain standards of uniformity. Original manuscripts are discarded after publication unless the Publisher is asked to return original material after use. Please use MS Word 2010 for the text of your manuscript.

Structure: Follow this order when typing manuscripts: Title, Authors, Authors title, Affiliations, Abstract, Keywords, Introduction, Main text, Conclusions, Acknowledgements, Appendix, References, Figure Captions, Figures and then Tables. Please supply figures imported into the text AND also separately as original graphics files. Collate acknowledgements in a separate section at the end of the article and do not include them on the title page, as a footnote to the title or otherwise.

Text Layout: Use 1.5 line spacing and wide (3 cm) margins. Ensure that each new paragraph is clearly indicated. Present tables and figure legends on separate pages at the end of the manuscript. If possible, consult a recent issue of the journal to become familiar with layout and conventions. All footnotes (except for table and corresponding author footnotes) should be identified with superscript Arabic numbers. To conserve space, authors are requested to mark the less important parts of the paper (such as records of experimental results) for printing in smaller type. For long papers (more than 4000 words) sections which could be deleted without destroying either the sense or the continuity of the paper should be indicated as a guide for the editor. Nomenclature should conform to that most frequently used in the scientific field concerned. Number all pages consecutively; use 12 or 10 pt font size and standard fonts.

Corresponding author: Clearly indicate who is responsible for correspondence at all stages of refereeing and publication, including post-publication. The corresponding author should be identified with an asterisk and footnote. Ensure that telephone and fax numbers (with country and area code) are provided in addition to the e-mail address and the complete postal address. Full postal addresses must be given for all co-authors. Please consult a recent journal paper for style if possible.

Abstract: A self-contained abstract outlining in a single paragraph the aims, scope and conclusions of the paper must be supplied.

Keywords: Immediately after the abstract, provide a maximum of six keywords (avoid, for example, 'and', 'of'). Be sparing with abbreviations: only abbreviations firmly established in the field may be eligible.

Symbols: All Greek letters and unusual symbols should be identified by name in the margin, the first time they are used.

Units: Follow internationally accepted rules and conventions: use the international system of units (SI). If other quantities are mentioned, give their equivalent in SI.

Maths: Number consecutively any equations that have to be displayed separately from the text (if referred to explicitly in the text).

References: All publications cited in the text should be presented in a list of references following the text of the manuscript.

Text: Indicate references by number(s) in square brackets in line with the text. The actual authors can be referred to, but the reference number(s) must always be given.

List: Number the references (numbers in square brackets) in the list in the order in which they appear in the text.

Examples:

Reference to a journal publication:

[1] M.S. Mohsen, B.A. Akash, "Evaluation of domestic solar water heating system in Jordan using analytic hierarchy process". Energy Conversion & Management, Vol. 38 (1997) No. 9, 1815-1822.

Reference to a book:

[2] Strunk Jr W, White EB. The elements of style. 3rd ed. New York: Macmillan; 1979.

Reference to a conference proceeding:

[3] B. Akash, S. Odeh, S. Nijmeh, "Modeling of solar-assisted double-tube evaporator heat pump system under local climate conditions". 5th Jordanian International Mechanical Engineering Conference, Amman, Jordan, 2004.

Reference to a chapter in an edited book:

[4] Mettam GR, Adams LB. How to prepare an electronic version of your article. In: Jones BS, Smith RZ, editors. Introduction to the electronic age, New York: E-Publishing Inc; 1999, p. 281-304

Free Online Color : If, together with your accepted article, you submit usable color and black/white figures then the journal will ensure that these figures will appear in color on the journal website electronic version.

Tables: Tables should be numbered consecutively and given suitable captions and each table should begin on a new page. No vertical rules should be used. Tables should not unnecessarily duplicate results presented elsewhere in the manuscript (for example, in graphs). Footnotes to tables should be typed below the table and should be referred to by superscript lowercase letters.

Notification: Authors will be notified of the acceptance of their paper by the editor. The Publisher will also send a notification of receipt of the paper in production.

Copyright: All authors must sign the Transfer of Copyright agreement before the article can be published. This transfer agreement enables Jordan Journal of Mechanical and Industrial Engineering to protect the copyrighted material for the authors, but does not relinquish the authors' proprietary rights. The copyright transfer covers the exclusive rights to reproduce and distribute the article, including reprints, photographic reproductions, microfilm or any other reproductions of similar nature and translations.

Proof Reading: One set of page proofs in MS Word 2010 format will be sent by e-mail to the corresponding author, to be checked for typesetting/editing. The corrections should be returned within **48 hours**. No changes in, or additions to, the accepted (and subsequently edited) manuscript will be allowed at this stage. Proofreading is solely the author's responsibility. Any queries should be answered in full. Please correct factual errors only, or errors introduced by typesetting. Please note that once your paper has been proofed we publish the identical paper online as in print.

Author Benefits:

No page charges: Publication in this journal is free of charge.

Free offprints: One journal issues of which the article appears will be supplied free of charge to the corresponding author and additional offprint for each co-author. Corresponding authors will be given the choice to buy extra offprints before printing of the article.

PAGES**PAPERS**

- 161 - 166 **Olive Mill Wastewater as Cutting Fluids: Effect on Surface Roughness of Aluminum**
Nabeel Gharaibeh , Musa AlAjlouni , Ammar Al-Rousan
- 167 - 170 **Photovoltaic Cooling Using Phase Change Material**
Mohammad Hamdan , Mohammad Shehadeh, Ahmad Al Aboushi, Amer Hamdan, Eman Abdelhafez
- 171– 177 **MHD Tangent Hyperbolic Nanofluid with Zero Normal Flux of Nanoparticles at the Stretching Surface with Thermal Radiation**
Itedi Shrivani , Dodda Ramya , Sucharitha Joga
- 179– 188 **Proposed Inventory Strategy of NSR Material in Cikarang-Indonesia Oil and Gas**
Atma Yudha Prawira , Euis Nina Saparina Yuliani , Hardianto Iridiastadi
- 189– 196 **Solar Panel Cooling and Water Heating with an Economical Model Using Thermosyphon**
Laith Jaafer Habeeb, Dheya Ghanim Mutasher , Faez Abid Muslim Abd Ali
- 197– 213 **Prediction of Flow Parameters of Glass Beads-Water Slurry flow through Horizontal Pipeline using Computational Fluid Dynamics**
Shofique Ahmed, Rajesh Arora, Om Parkash
- 215– 229 **Exact Thermomechanical Characteristics of a Pressurized Rotating Circular Annulus or a Disc Made of Functionally Graded (FG) Hypothetical and Physical Materials**
Vebil Yıldırım
- 231– 243 **Nabatean Archaeometallurgy at Petra, Jordan**
Khraisat, Bilal, L.Campanella, D.Ferro, S.Bovani, T.Akasheh
-

Olive Mill Wastewater as Cutting Fluids: Effect on Surface Roughness of Aluminum

Nabeel Gharaibeh^a, Musa AlAjlouni^a, Ammar Al-Rousan^{b,*}

^aMechanical Engineering Department, Al-Balqa Applied University, Al-Huson University College, Irbid, Jordan

^bDepartment of Industrial Engineering, Hijawi Faculty for Engineering Technology, Yarmouk University.

Received 8 Apr. 2018

Abstract

In this experimental work, the use of olive mills' wastewater (OMW) as a cutting fluid in machining processes has been investigated. The experiments were performed on the most two common metal removing processes, namely turning and milling with the use of the proposed cutting fluid. In this present study, the performances of OMW were compared with that of mineral oil-based cutting fluid and dry conditions during the machining operation of Aluminum alloy. The effect of OMW as cutting fluid on the surface roughness of Aluminum alloy has been studied. The experiment involved the use of different parameters such as cutting speed, depth of cut and feed rate. The values of the measured surface roughness found to be in the range of good performance for turning and milling ($R_a = 0.4\text{--}2.5$ micron). R_a is the submicron size for good operation parameters (specifically when Depth of cut is less than 0.5 mm and spindle speed is more than 2200 rpm). The results of this work compared with different theoretical models from works of literature have been found to be in agreement with them. The proposed fluid worked very well as a cutting fluid. Based on these results, OMW is being recommended as viable alternative lubricants to the mineral oil during machining. More investigations need to be done to check the safety measures and chemical hazards of using it.

© 2018 Jordan Journal of Mechanical and Industrial Engineering. All rights reserved

Keywords: Cutting Fluid, Surface Roughness, Cutting speed, Feed, Depth of cut, Olive mill wastewater (OMW);

1. Introduction

Although Jordan ranks as the eighth largest olive oil producing country in the world, it still lacks proper facilities for the treatment of OMW (or Zibar as locally called), an oily waste generated during the olive oil extraction process [1]. Jordan has more than 15 million olive trees that produce over 130,000 tons of olives, 85 percent of which farmers send to the 128 olive presses spread across the country. Seventy percent of the mills are in the northern region. In 2012, the country's olive mills produced 212,418 cubic meters of zibar, which resulted from the processing of 115,282 tons of olives [1] and more detail for the northern part of Jordan can be found in Table 1 [2].

OMW is black or reddish black, with a strong offensive smell, a high percentage of fat, oil, and grease as well as a high organic load, which is 400 times higher than that of domestic wastewater. A remarkable study [1], warned from the disposal OMW. If it spreads on soil or is dumped in valleys, OMW (zibar) can cause serious environmental problems and reduce soil fertility as it contains many chemicals. The authors of this study [1] presented several recommendations to manage the disposal of zibar,

including the establishment of an olive oil wastewater treatment plant and evaporation ponds to serve all the presses across the country. One potential solution is to use OMW in irrigation. The effect of it on soil properties, olive tree performance, and oil quality had been studied [3]. They found that if it used in a controlled way it will with no negative effects. The ratio of dilution had been studied and from the data obtained, it is suggested that 1:20 OMW dilutions are still phytotoxic and that higher OMW dilutions should be used in order to use this waste for the irrigation of spinach plants [4]. Another study in Italy is to use OMW in the vermicomposting process. The results obtained from the photo-test showed that the OMW lose their toxicity and stimulate plant germination and growth [5]. One more application may be in the pharmaceutical industry by separation of polyphenols from Jordanian OMW [6]. A Review of the technologies for OMW treatment presented in the literature [7]. A more recent comprehensive review of OMW components extraction and management were present in reference [8]. In that work, the state of the art of OMW management was presented, with a focus on physicochemical processes, either alone or in combination, varying in complexity, ease of operation, and associated costs. Until now there has not been a defined management strategy that can be adopted

* Corresponding author e-mail: alrousana@yu.edu.jo.

on a global scale that is feasible in different socio-economic contexts and production scales. A plethora of reclamation practices, as well as combined treatments for OMW, have already been proposed and developed but have not led to completely satisfactory results [Details can be found in 8].

On the other side, many researchers studied the use of different types of vegetable oils such as rapeseed, canola, and coconut oil as an alternative for mineral oil in cooling machining processes. Vegetable Oil-Based Cutting Fluids had been used as a cutting fluid in machining operations [9-13]. The results of these studies encouraged to using OMW, which is a similar material, as a cutting fluid and this is the aim of the current work.

Cutting fluid plays a major role in machining operations. These roles include making cutting easy, improving tool life, improving surface finish, flushing away chips from the cutting zone, increasing the rate of productivity, and alleviating the negative effect on work environment and operators. The cutting fluid contributes significantly toward machining cost and also possesses environmental threats. The cutting fluids of the future have to be more environmentally adapted, have a higher level of performance, and lower total life-cycle cost (LCC) than commonly used cutting fluid today. The properties of the base fluids must be identified in order to be able to formulate. They can be divided into three groups, i.e., physical, chemical, and film formation properties. The fluid is used as a coolant and also as lubricates of the cutting surfaces. The selection of cutting fluid should also include considerations such as its effects on, workpiece material and machine tools, biological considerations and the environment [14-16]. There are a few challenges associated with the use of OMW as cutting fluids. The aim of this work is to achieve better surface quality with low machining cost with new fluid. As the OMW is free of charge waste material, it has been used as a cutting fluid for different cutting machines.

Table1. Quantities of Zibar water (in cubic meters) produced in Jordan [2].

	Number of extraction mills	2008	2009	2010	2011	2012	2013	2014
Irbid	53	6338	6374	35554	14154	18454	12447	17830
Mafraq	12	1089	2748	1906	2843	2394	4915	5955
Jerash	15	3433	4138	17011	4486	5071	3945	4960
Ajloun	15	3429	4672	13486	8440	8044	7409	6981
Total	95	14289	17932	67957	29923	33963	28716	35726

2. MATERIALS & METHODS

2.1. Workpiece material

Aluminum and its alloys are used in a huge variety of products because of its special properties. It is non-toxic, and has low density and high thermal conductivity, and it also has excellent corrosion resistance, and can be easily cast, machined and formed. The composition as well as the physical, mechanical, electrical, thermal, and processing properties of Aluminum alloys can be found in the literature [e.g. 14]. For these reasons, low-cost aluminum

alloy (5083) is used as workpiece material. The detail specification and composition of this alloy can be found in the open source through the internet.

2.2. The cutting fluid (OMW)

OMW (**Zibar**) is known as a liquid material "wastewater" black colored produced by pressing the olive into oil, and according to specialists; it has a very influential effect on both the environment and the economy together if it wasn't treated or being used. OMW contains a high rate of dangerous components that threaten human life. The most important of these are Phenol and Chemical Oxygen. OMW water becomes dangerous only if drained into the environment and interact with the heat and atmosphere. Environmentalists warn of the risk allowing owners of extraction factories of using OMW to irrigate trees because it may affect the groundwater. It also affects the environmental tourism and spreads bad smells. On the other side, OMW has many advantages if it is well treated. These include the manufacture of medicines and herbicides, Cosmetic industry, the manufacture of fertilizers and explained in this work, it can be used as cutting fluid. The OMW used in the experiments had been collected from one of the extraction mills after taking permission for that. After the tests, all waste of OMW together with chips were treated and safely disposed of.

2.3. Turning operation

A controlled turning experiment was conducted on 4-mm length sample cutting from 26-mm diameter rod of aluminum alloy to determine the relationship between the depth of cut, cutting speed and surface quality. The selected feed rate was held constant. The experiments were performed on a Benchtop Lathe — 160TCLi, powered with CNC machine at five levels of depth of cut and speed combinations as listed in Table 2. A Carbide pet cutting tool has been set up. This choice is because Aluminum has low hardness and good ductility, also this tool is relatively inexpensive. 3200 rev/min rotational speed with 0.5 mm depth of cut has been made for all samples to identify a specific reference to start with.

2.4. Milling operation

A controlled milling experiment was conducted on an aluminum block (with average face dimensions of 40 mm x 40 mm) to determine the relationship between the depth of cut and the surface quality. The selected feed rate was held constant. Numerous amounts of coolant were provided at the cutting zone throughout the experiment. The experiments were performed as conventional/ up milling at five levels of depth of cut and speed combinations as listed in Table 3. The tool was checked for wear after each run.

2.5. Surface Roughness Measurement

Surface roughness is a component of surface texture. Surface roughness (Ra) is the arithmetic average of the roughness profile. The surface roughness measurements of the workpiece were recorded using surfcom flex

measuring machine for measuring surface roughness. No other formal cleaning process was used, and care was taken not to scratch the surface of the samples during handling.

Table 1. Experimental setup (Turning): Speeds and depth of cut (Constant Feed rate).

Runs	Depth of cut (mm)	Speed (rpm)	Colling oil
1-5	0.2	3200, 3000, 2800, 2600, 2400	OMW
6-10	0.4	3200, 3000, 2800, 2600, 2400	OMW
11-15	0.6	3200, 3000, 2800, 2600, 2400	OMW
16-20	0.8	3200, 3000, 2800, 2600, 2400	OMW
21-25	1.0	3200, 3000, 2800, 2600, 2400	OMW
26-30	0.6	3200, 3000, 2800, 2600, 2400	Standard

Table 2. Experimental setup (Milling): Speeds and depth of cut (Feed rate= 30 mm/min).

Runs	Depth of cut (mm)	Speed (rpm)	Cooling oil
1-5	0.2	1800, 2000, 2200, 2400, 2600	OMW
6-10	0.5	1800, 2000, 2200, 2400, 2600	OMW
11-15	0.7	1800, 2000, 2200, 2400, 2600	OMW
16-20	1.0	1800, 2000, 2200, 2400, 2600	OMW
21-25	1.2	1800, 2000, 2200, 2400, 2600	OMW
26-30	1.2	1800, 2000, 2200, 2400, 2600	Standard

3. Experimental results and discussions

The measured values of surface roughness are plotted against the five cutting speeds for each of the depth of cut increments as shown in Figures (1-4). Figure (1) shows the effect of the cutting speed on surface roughness. As common, increasing the cutting speed improved surface quality. The best result found to be when the depth of cut was in the mid-range (around 0.5 mm). Additionally, the average surface roughness values are re-plotted with respect to the cutting speed to examine the effects of depth of cut. The effect of depth of cut (as shown in Figure (2)) is less significant. As expected, the surface quality of the machined surface reduction with increasing the depth of cut (Figure 2).

The same observations of the turning operation (Figures 1 and 2) can be noted, also, for milling operation (Figure 3 and 4). In these figures, the effect of increasing the speed is clear on the surface enhancement. The results after a speed of 2200 rpm and depth of cut of 0.7 mm become better and more stable. Figures (5 and 6) show the same results in three-dimensional representations. These figures show that the effects of both parameters are not clear because of using a constant feed rate. The most

effective parameter is the feed rate that aligns with the results of many references in the literature.

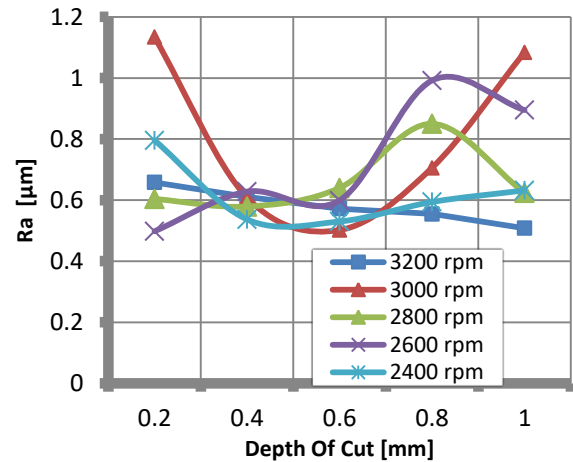


Figure 1. The plot of average surface roughness (μm) for the turning operations at different depth of cut (mm) and different speed. The feed rate is constant = 30 mm/min.

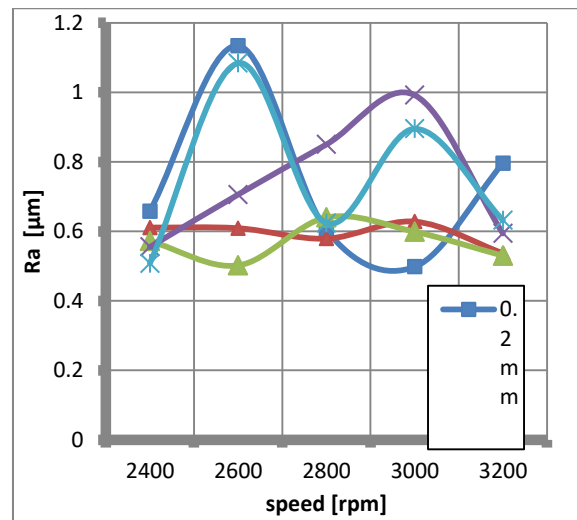


Figure 2. The plot of the average surface roughness (μm) for the turning operations at different speeds (rpm) and different depth of cut. The feed rate is constant.

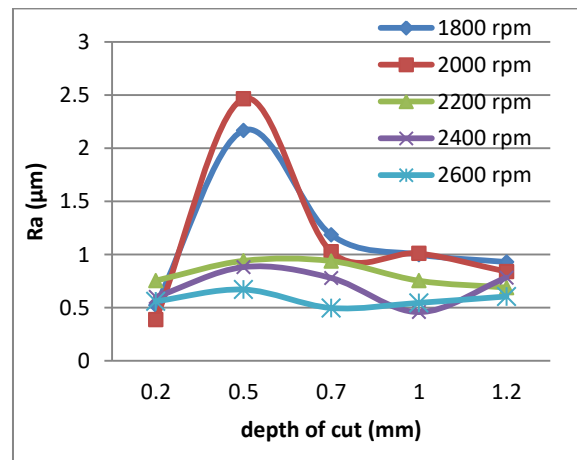


Figure 3. The plot of the average surface roughness (μm) for the milling operations at different depth of cut (mm). The feed rate is constant = 30 mm/min.

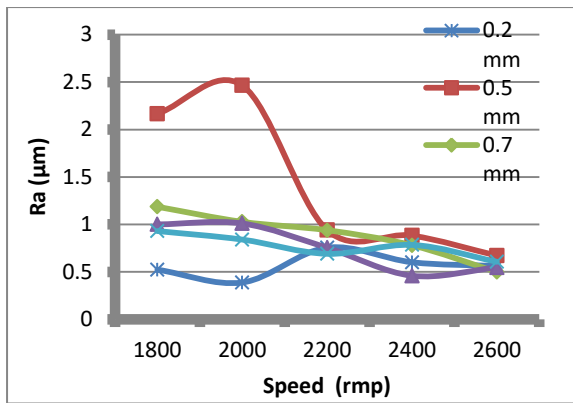


Figure 4. The plot of the average surface roughness (μm) for the milling operations at different speeds (rpm). The feed rate is constant.

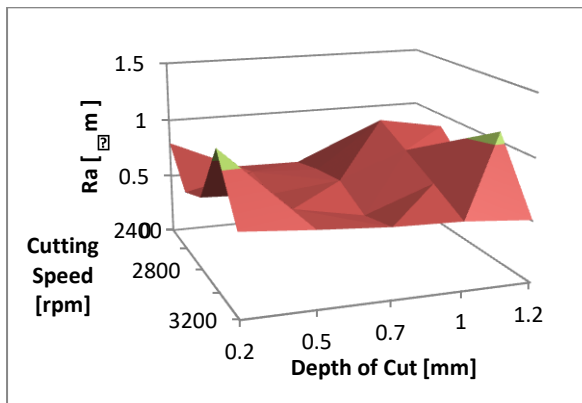


Figure 4. 3D Graph for turning operation at a constant feed rate.

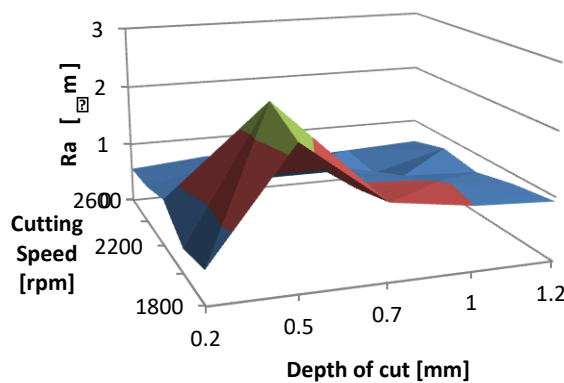


Figure 5. 3D Graph for milling operation at a constant feed rate.

Figures (7 and 8) show a comparison between the OMW as cutting fluid and standard sellable oil. The curves are close together with preference to OMW in the milling operation. Figure (8) shows a great effect on surface enhancement when using OMW especially at a speed of 2000 rpm.

Figure (9) compares the experimental results with two theoretical models based on the work of others [17 and 18]. The first model [17] which predicted the surface roughness with the effect of spindle speed, cutting feed rate and depth of cut. According to this model, the arithmetic average roughness (R_a) can be predicted by:

$$R_a = 3.179 + 9.826 * F - 0.009 * V - 0.922 * D \quad (1)$$

Where R_a : surface roughness in μm, V : cutting speed in m/min, F : cutting feed in m/min and D : depth of cut in mm.

The Second Model [18] using the following formula:
 $R_a = 1.52 - 0.00189 V + 0.000111 N + 1.33 F - 0.200 D \quad (2)$

Where R_a , V , F , and D are as before and N : spindle speed in rpm.

Figure (10) compares the milling results of this work with three mathematical models. The first model which includes the effect of spindle speed, cutting feed rate and depth of cut, and any two variable interactions, predicted the surface roughness [19]. Using these coefficients, the multiple regression equation could be expressed as:

$$R_a = 1.178854 - 0.000492 N + 0.009897 F - 0.17625 D - 0.000003 (N * F) + 0.000811 (N * D) - 0.003012 (F * D) \quad (3)$$

Where R_a , N , F , and D are as defined previously.

The second model was developed for dry and the third for Minimum Quantity Lubrication (MQL) machining using multiple regression analysis which can be applied to surface roughness prediction of end milling of aluminum under dry and MQL environments; analysis of variance (ANOVA) was used to determine the significance of cutting parameters on surface roughness [20]. The final prediction formulas for these models are

$$R_a = (12.68F^{0.69}D^{0.04})/N^{0.81} \quad (4)$$

$$R_a = (10.80F^{0.70}D^{0.04})/N^{0.82} \quad (5)$$

Where equation (4) is the mathematical model for dry condition and equation (5) is the mathematical model for MQL condition. The experimental results of this work, as shown in figures (9 and 10), are within the different models. This result proves that the use of OMW as a cutting fluid is an effective choice. The outlying points in the above figures can be qualified to factors such as the vibration of the machine, obliqueness in the workpiece, tool wear, the temperature of the workpiece, and variation in material composition.

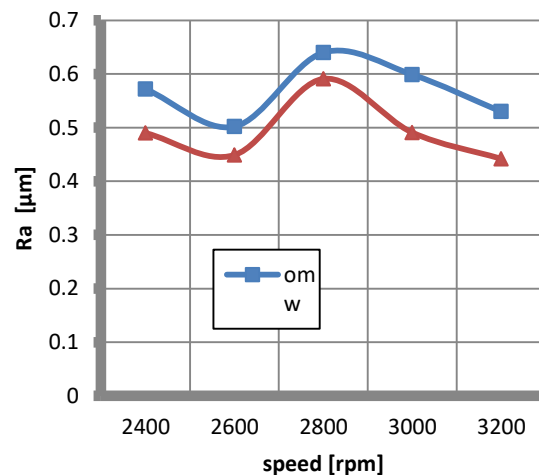


Figure 6. Plot of average surface roughness (μm) for the turning operations for different cooling fluid.

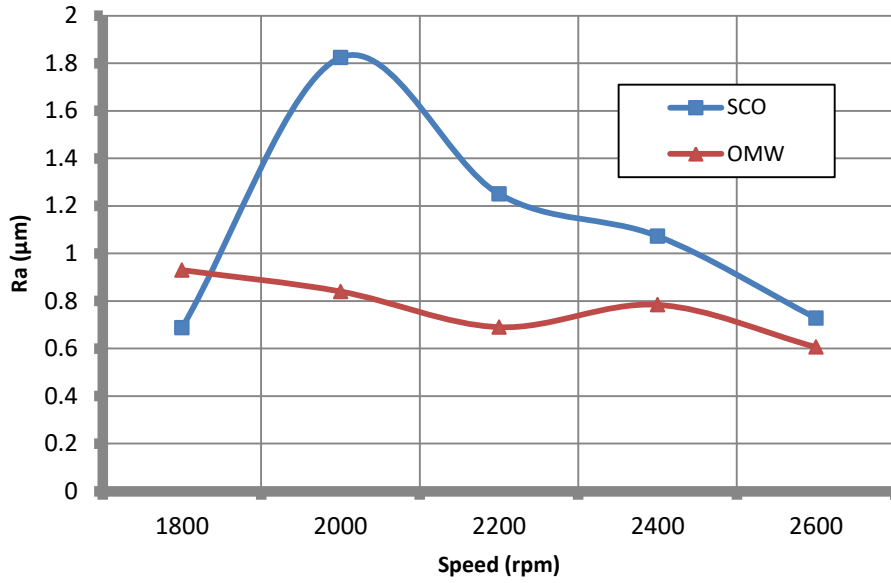


Figure 7. The plot of average surface roughness (μm) for the milling operations for different cooling fluid.

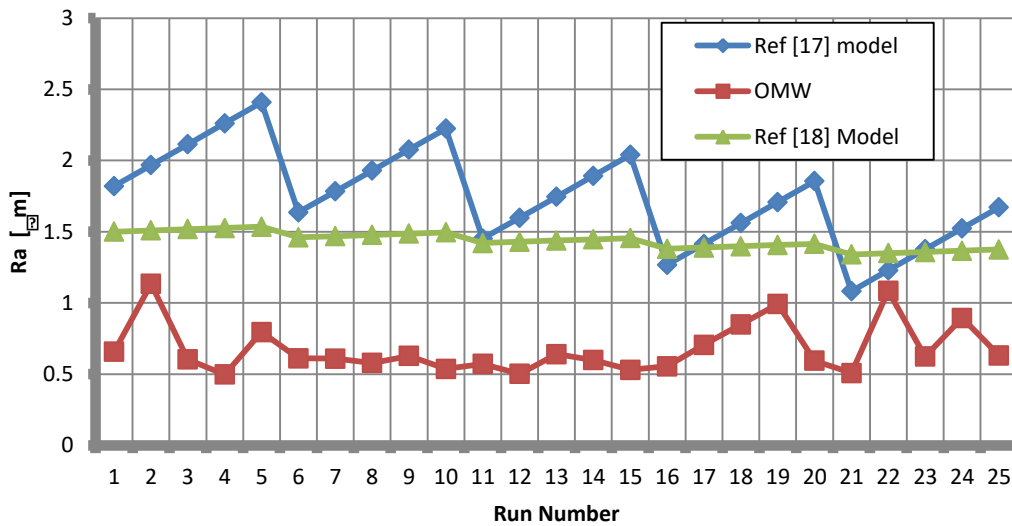


Figure 8. The plot of the average surface roughness (μm) for the turning operations for different methods.

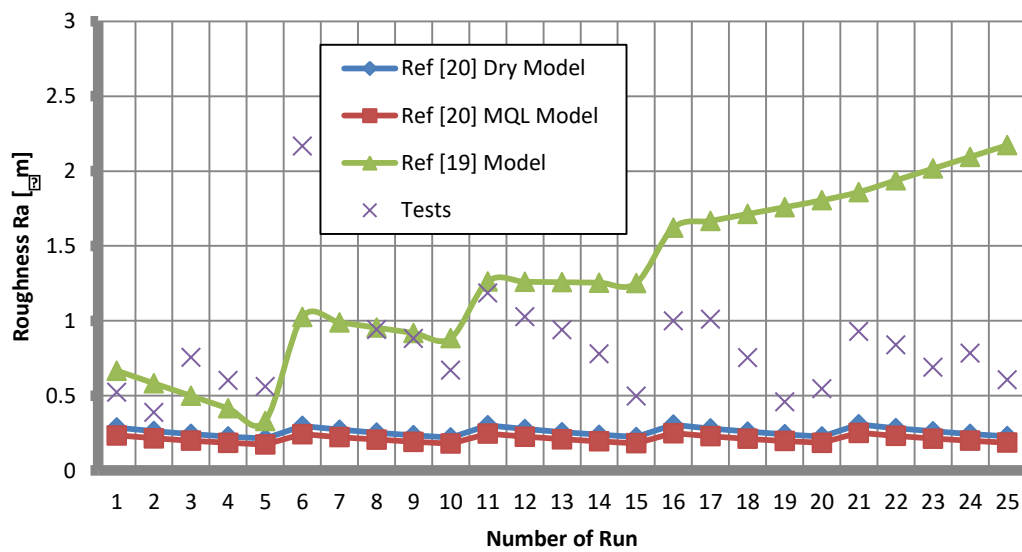


Figure 9. The plot of the average surface roughness (μm) for the milling operations for different prediction methods.

4. Conclusions

Jordan like other olive oil producing countries is facing severe environmental contamination problems due to the lack of full treatment of OMW at present. One possible use of OMW is to consume it in machining processes as a cutting fluid. Cutting fluid plays very important roles during the machining process. They are used to transfer heat, to lubricate the tool surface, and to transport the Chips. This article presents the roughness of the surface machined with the proposed cutting fluid, wherein the total number of measurements is equal to 60 trails. The results show that OMW worked effectively as a cutting fluid. Comparing with different theoretical and experimental models from literature, OMW worked very well. Detailed interpretation of the results is presented.

From this study, it may be concluded that the better surface finish may be achieved by turning and milling Aluminum alloy at low feed rate and high spindle speeds.

In conclusion, OMW can be used as a lubricant in turning and milling operations as an effective alternative to other conventional cutting fluids for environmental and health aspects. On further experiments, more investigations of the chemical hazard of this operation must be performed.

References

- [1] Royal department for protecting the environment (Rangers), Jordan, 2018, http://www.rangers.psd.gov.jo/sites/default/files/files/water_0.pdf
- [2] S. Ayoub, K.Al-Absi, S.Al-Shdiefat, D. Al-Majali, D. Hijazean, "Effect of olive mill wastewater land-spreading on soil properties, olive tree performance and oil quality". *Scientia Horticulturae* 175 (2014) 160–166. DOI:10.1016/j.scienta.2014.06.013
- [3] Maria Asfi & Georgia Ouzounidou & Michael Moustakas, Evaluation of olive oil mill wastewater toxicity on spinach, *Environmental Science and Pollution Research* Vol. 19, No. 6,2012, 2363–2371. DOI: 10.1007/s11356-012-0746-y
- [4] C.Macci, G.Masciandaro, B.Ceccanti, "Vermicomposting of olive oil mill wastewater". *Waste Management & Research*, Volume: 28, issue: 8, 2010, 738-747. DOI: 10.1177/0734242X09345278
- [5] [6] A. A. Deeb, M. K. Fayyad, M. A. Alawi, "Separation of Polyphenols from Jordanian Olive Oil Mill Wastewater," *Chromatography Research International*, vol. 2012, Article ID 812127, 2012, 1-8. DOI:10.1155/2012/812127
- [6] P.Paraskeva, E. Diamadopoulos, "Technologies for olive mill wastewater (OMW) treatment: a review". *Journal of Chemical Technology and Biotechnology* Vol. 81,2006, 1475–1485. DOI: 10.1002/jctb.1553
- [7] A. M. Gómez-Caravaca, A. Segura-Carretero, A.Martínez-Férez, J. M.Ochando-Pulido. Recovery of Phenolic Compounds from Olive Oil Mill Wastewaters by Physicochemical Methodologies. In: Grumezescu AM, Holban AM, editors *Food Bioconversion: Handbook of Food Bioengineering*, Volume 2, Academic Press is an imprint of Elsevier, 2017, ch14 p. 467-489. DOI: 10.1016/B978-0-12-811413-1.00014-0
- [8] N. Gharaibeh, "Vegetable and Mineral Used Oils as Cutting Fluids: Effect on Surface Roughness of Aluminum Alloy". *Journal of Surface Engineered Materials and Advanced Technology*, Vol. 6, No. 4, 2016, 176-182. DOI: 10.4236/jsemt.2016.64016
- [9] S. K. Kolawole, J. K. Odusote, "Performance Evaluation of Vegetable Oil-Based Cutting Fluids in Mild Steel Machining", *Chemistry and Materials Research*, Vol.3 No.9, 2013, 35-46. ISSN 2224- 3224 (Print) ISSN 2225- 0956 (Online)
- [10] S. Gariani, I. Shyha, M. A. El-Sayed, D. Huo, "Investigation into the effect of cutting fluid concentration on the machinability of Ti-6Al-4V using vegetable oil-based cutting fluids", *Journal of Engineering*, Volume 6, Issue 2, 2017, 414-423. ISSN: 0747-9964
- [11] E. Kuram, B. Ozcelik, E. Demirbas. Environmentally Friendly Machining: Vegetable Based Cutting Fluids. In: Davim J. editor. *Green Manufacturing Processes and Systems. Materials Forming, Machining, and Tribology*. Springer, Berlin, Heidelberg, 2013, p. 23-47. DOI: 10.1007/978-3-642-33792-5_2
- [12] M. S. Saleem, M.. Z. Khan, M. Z.Zaka, "Vegetable oil as an alternate cutting fluid while performing turning operations on a lathe machine using single point cutting tool", *International Journal of Technical Research and Applications* Volume 1, Issue 5, 2013, 103-105. e-ISSN: 2320-8163
- [13] ASM Aerospace Specification Metals, Inc.[http://asm.matweb.com/search/SpecificMaterial.asp?bassnum=ma6061t6\(2018\)](http://asm.matweb.com/search/SpecificMaterial.asp?bassnum=ma6061t6(2018))
- [14] M. Kuttolamadom, S. Hamzehlouia, L. Mears, "Effect of Machining Feed on Surface Roughness in Cutting 6061 Aluminum", *SAE International Journal of Materials and Manufacturing*, Vol. 3, No. 1, 2010, 108-119. DOI: 10.4271/2010-01-0218.
- [15] E. Rezvani, H. Ghayour, M. Kasiri, "Effect of cutting speed parameters on the surface roughness of Al5083 due to recrystallization". *Mechanical Sciences*, Vol. 7, No. 1, 2016,85–91. DOI:10.5194/ms-7-85-2016.
- [16] J. P. Davim, "A note on the determination of optimal cutting conditions for surface finish obtained in turning using design of experiments", *Journal of Materials Processing Technology*, Vol. 116, No. 2, 2001, 305-308. ISSN: 0924-0136
- [17] S. H. Aghdeab, L. A. Mohammed, A. M. Ubaid, "Optimization of CNC Turning for Aluminum Alloy Using Simulated Annealing Method". *Jordan Journal of Mechanical and Industrial Engineering JJMIE*, Volume 9, Number 1, 2015, 39-44. ISSN 1995-6665
- [18] M. T. Hayajneh, M. S. Tahat, J.Bluhm, "A Study of the Effects of Machining Parameters on the Surface Roughness in the End-Milling Process". *Jordan Journal of Mechanical and Industrial Engineering JJMIE*, Volume 1, Number 1, 2007, 1 – 5. ISSN 1995-6665
- [19] O. S. Joshua, M. O. David, I. O.Sikiru, "Experimental Investigation of Cutting Parameters on Surface Roughness Prediction during End Milling of Aluminium 6061 under MQL (Minimum Quantity Lubrication)".*Journal of Mechanical Engineering and Automation*, Vol. 5, No. 1,2015, 1-13. DOI: 10.5923/j.jmea.20150501.01

Photovoltaic Cooling Using Phase Change Material

Mohammad Hamdan^{a,*}, Mohammad Shehadeh^a, Ahmad Al Aboushi^b,
Amer Hamdan^b, Eman Abdelhafez^b

^a Mechanical Engineering Department, The University of Jordan, Amman 11942, Jordan

^b Mechanical Engineering Department, Al-Zaytoonah University of Jordan, Amman 11733, Jordan

Received 15 Jan. 2018

Abstract

In this work an experimental work was conducted to improve the performance of photovoltaic panels (PV) by cooling them using phase change materials (PCM). A photovoltaic system made up of two identical PV panels were installed side by side, PCM was integrated on the back side of one of these photovoltaic panels, while the other one was kept as a standard one for comparison purposes. A micro converter with all necessary accessories to conduct the work were also used. The generated currents and voltages, temperatures of the ambient and the PV panels and the incident solar irradiance were recorded on hourly basis for twenty-eight days using a data acquisition system. The stored data was analyzed and it was found that the cooled PV panel using PCM had performed 2.6% better than the standard panel.

© 2018 Jordan Journal of Mechanical and Industrial Engineering. All rights reserved

Keywords: Photovoltaic Panels (PV), Phase Change Materials (PCM), Photovoltaic Cooling

1. Introduction

Worldwide energy has become the main concern for nations, especially with unpredictable fossil fuel prices, political driven energy market, global warming, environmental aspects, and the future availability of fossil fuel versus demand. This has driven researchers to study the possibility to compensate part of the energy which is generated by fossil fuel with alternative and sustainable resources. Among such sources, solar energy was found to be a very promising source of energy.

Solar energy is converted into electricity using Photovoltaic cells (PV) with maximum efficiency at around 15-20 %, depending on the type of solar cells. Almost 80% of the solar radiation reaching the (PV) will be reflected or transformed into heat energy. This leads to an increase in the cells temperature, and consequently a drop in the PV efficiency. So a reliable heat dissipation system is needed to cool the cells effectively in order to enhance the efficiency of the cells.

Tonui and Tripanagnostopoulos (2007a) [1] studied the use of a suspended thin flat metallic sheet at the middle or fins at the back wall of an air duct as heat transfer augmentations in an air-cooled photovoltaic/thermal (PV/T) solar collector to improve its overall performance. The steady-state thermal efficiencies of the modified systems are compared with those of typical PV/T air system. Daily temperature profiles of the outlet air, the PV rear surface and channel back wall are presented confirming the contribution of the modifications in increasing system electrical and thermal outputs and found that photovoltaic (PV) panels

suffer efficiency drop as their operating temperature increases especially under high insolation levels.

Tonui and Tripanagnostopoulos (2007 b) [2] studied the performance of two low cost heat extraction improvement modifications in the channel of a PV/T air system to achieve higher thermal output and PV cooling so as to keep the electrical efficiency at acceptable level. The validated model was then used to study the effect of the channel depth, channel length and mass flow rate on electrical and thermal efficiency. PV cooling and pressure drop for both improved and typical PV/T air systems and their results were compared. Both experimental and theoretical results showed that the suggested modifications improved the performance of the PV/T air system and the excess temperatures on installed photovoltaic (PV) modules lead to efficiency loss and PV cooling protected them from this undesirable efficiency drop.

Odeh and Behnia (2009) [3] carried out a long-term performance modeling of a proposed solar-water pumping system, which consists of a PV module cooled by water, a submersible water pump, and a water storage tank. Cooling of the PV panel is achieved by introducing water trickling configuration on the upper surface of the panel. The experimental results indicated that an increase of about 15% in system output is achieved at peak radiation conditions. Long-term performance of the system is estimated by integrating test results in a commercial transient simulation package using site radiation and ambient temperature data. The simulation results of the system's annual performance indicated that an increase of 5% in delivered energy from the PV module can be achieved during dry and warm seasons.

* Corresponding author e-mail: mhamdan@ju.edu.jo.

Huang (2011) [4] has modified a numerical simulation model for single PCM application to predict the thermal performance of the multi-PCMs in a triangular cell system. Having conducted a series of numerical simulations tests in static state and realistic conditions, he discussed the thermal regulation of the PV/PCM system with a different range of phase transient temperature PCMs.

Teo et al (2012) [5] have designed, fabricated and experimentally investigated a hybrid photovoltaic/thermal (PV/T) solar system to actively cool the PV cells, a parallel array of ducts with inlet/outlet manifold designed for uniform airflow distribution was attached to the back of the PV panel. Experiments were performed with and without active cooling. A linear trend between the efficiency and temperature was found. Without active cooling, the temperature of the module was high and solar cells can only achieve an efficiency of 8–9%. However, when the module was operated under active cooling condition, the temperature dropped significantly leading to an increase in efficiency of solar cells to between 12% and 14%.

Zhao and Tan (2014) [6] have investigated the theoretical performance characteristics of PV modules using an adapted analytical model. A prototype thermoelectric system integrated with PCM heat storage unit for space cooling is used for this study. It was found that using PCM heat storage unit leads to a saving of 35.3% in electrical energy.

Hasan et al (2014) [7] studied the effect of using PCM to cool PV panels in two different countries, Ireland and Pakistan by integrating PCM into PV panels to absorb excess heat. Electrical and thermal energy efficiency analysis of PV-PCM systems was conducted to evaluate their effectiveness and found that in Ireland the financial benefit of both PV-PCM systems is less than the cost incurred to mass produce such systems confirming that such systems are not cost effective in Ireland. However, the cost of the PV-PCM systems is almost half of the benefit in Pakistan which shows that such systems are cost effective in such climates, and thus encourages the possibility of future research to improve performance to make them more effective.

Tan and Zhao (2015)[8] have proposed a numerical model for space cooling purpose using a thermoelectric cooling system integrated with phase change material (PCM). The analysis conducted was under two modes (1) dissipating the generated heat directly to outdoor air through the air-water heat exchanger, and (2) releasing heat to the shell-and-tube PCM heat storage unit. The model was validated using experimental work, which showed the average system cooling COP is increased by 56% (from 0.5 to 0.78) due to PCM integration.

The performance of a PV/T module that employs a Micro-encapsulated Phase Change Material slurry as the working fluid was presented by Qui et.al (2015)[9]. It was found that the established model, based on the Hottel–Whillier assumption, was able to predict the energy performance of the MPCM slurry based PV/T system at a very good accuracy, with 0.3–0.4% difference compared to a validated model. Furthermore, and under the turbulent flow condition, an increase in the concentration of the slurry leads to an improvement in

the performance of the module, which is due to the drop in temperature. Also, it was found that the net efficiency of the PV/T module reached the peak level at the concentration ratio of 5%.

For Jordan which is located in the Sun Belt area, solar energy is considered one of the best renewable energy resources to be used in heating water or generating electricity; with the fact that the average daily solar irradiation in Jordan is between 5 to 7 kWh/m² and the total annual irradiation is between 1600 to 2300 kWh/m². This proves to provide strong potential for energy generation in a sustainable way (EPIA, 2013) [10].

The main objective of this was to investigate the effect of cooling PV panels using phase change materials. To achieve this, a system was built using two identical panels of 250 Watt peak each. Both systems are installed at a tilt angle of 26 and facing south, one of the PV panels was a base unit and used for comparison purposes, while the second one was cooled by a PCM. The two panels were installed side by side and instantaneous measurements. The system is equipped with all necessary instruments to collect the performance data for each panel separately.

2. Experimental setup

As shown in figure 1, the experimental main components used in this work are:

1. Two Poly-Crystalline PV panels.

Each panel has 250Wp as nominal power and consists of 60 poly crystalline cells with 3.2mm low iron glass as a cover and aluminum anodized frame for protection.

2. Two micro inverters

These inverters enable individual panel control when flexibility and modularity is required which also can reduce shading and mismatching effect. Micro inverters are also equipped with a Maximum Power Point Tracker (MPPT) algorithm that maximizes energy and flexibility with an efficiency of 96.5 %, hot dip galvanized steel structure for fixing PV panels

3. Monitoring system and data acquisition system including weather station and the following devices

- a) Radiation sensor (Photoelectric).
- b) Two Temperature Sensors (RTD).
- c) Ambient Temperature sensor.
- d) Two current clamps.

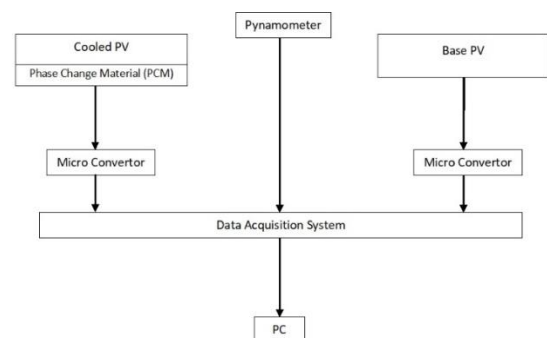


Figure 1. Experimental setup

PCM was chosen to have a melting point close to the V panels STC temperature condition; a product number 51-27 was used from PHASE CHANGE energy solutions. Table 1 shows the chosen PCM properties.

Table 1. PCM properties.

Parameter	Units	Value
Melting point	°C	27
Freeze point	°C	20
Latent heat storage capacity	J/g	200
Latent heat storage capacity	kWh/m ²	0.161
PCM Weight per m ²	kg	2.7

3. Experimental procedure

The two mounting systems were installed to face south at 26° tilt angel, the PV panels were installed on top of the mounting system and fixed using bolts and nuts. One PV module was covered from the back side with aluminum sheet, so it can accommodate the PCM while the other was used a base panel. The PCM was loaded manually to fill up the space between the aluminum sheet and the backside of the module, 8.33 Kg of PCM was enough to fill up the empty space between the sheet and the module which is equivalent to 3.03 m².

The Modules were connected to the micro inverters, which were connected to the data acquisition system. Also connected to the DAS, the pyranometer, which was used to measure the hourly incident solar radiation intensity and the temperatures sensors used to measure the ambient and the panel temperatures. The parameters that affect the performance of each panel were collected and analyzed to implement s the objectives of the experiment.

4. Results and Discussion

The ambient temperature, cooled module temperature, standard module temperature, irradiance and both PV panels performance expressed in terms of accumulative energy produced were recorded and stored through data acquisition system into a PC on a daily basis.

The accumulated daily energy production during the working period between 24th Oct 2014 and 18th Nov 2014 is presented in figure2. It may be noticed from this figure that there is a difference in the accumulative performance of the cooled panel and the base panel with a difference value of 2.6% based on the period during which work was conducted. The cooled panel generated 27.7 kWh, while the base one generated 26.9 kWh.

Figure 3 shows the daily energy generated by each panel and figure 4 shows the average daily temperature for each panels. As indicated in this figure the ambient maximum and minimum temperatures were recorded on 26th of October and 16th of November respectively. Consequently, only these days will be considered in this section.

Figure 4 shows the hourly generation from 6 am to 6 pm on 26th of Oct., which shows the highest ambient

temperature and the highest average temperature for the panels cooled by PCM. While figure 5 shows the accumulative energy by each panel during this day.

From the figures above it can be noticed that the energy gap between the PCM cooled panel and the standard panel is 1.78% only, which is lower than the average energy gap for the whole experiment, with the value 2.6%.

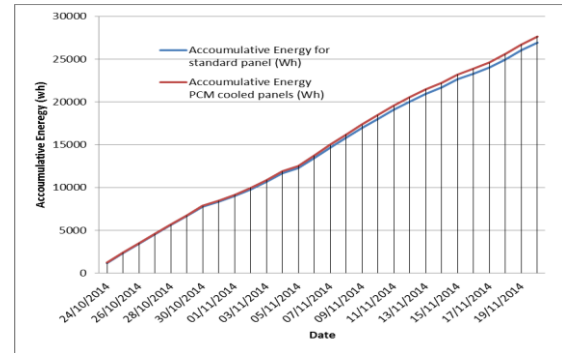


Figure 2. Accumulative energy generated for PCM cooled and standard PV panels.

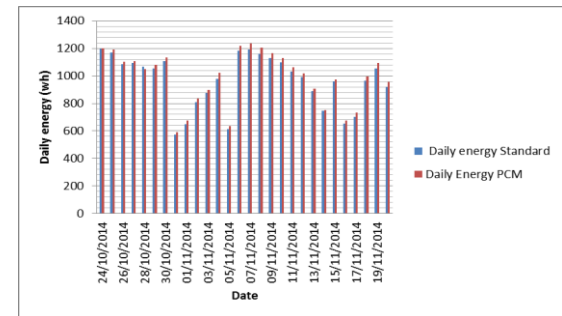


Figure 3. Daily energy generated for PCM cooled and standard PV panels.

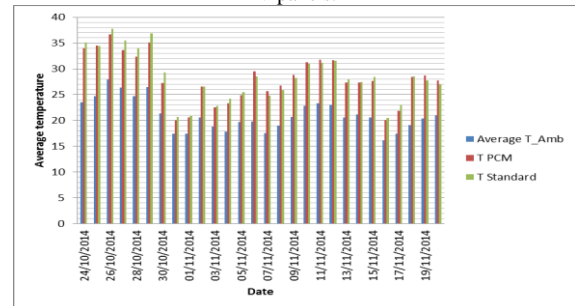


Figure 4. Daily average temperature for ambient, PCM cooled and standard panels

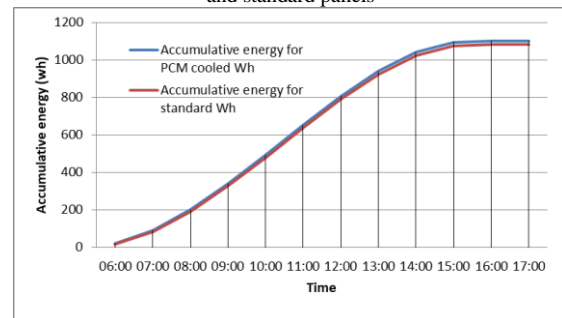


Figure 5. Accumulated energy generation on 26th Oct

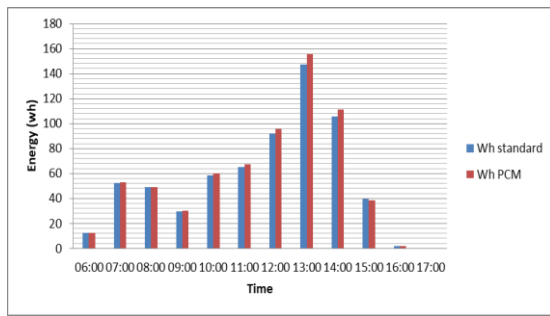


Figure 6. Hourly energy generation on 16th Nov

Figure 6, shows the hourly generation from 6 am to 6 pm on 16th of Nov., as indicated in this figure, the lowest average ambient temp and the lowest average temperature for the standard panel. Figure 7, shows the accumulative energy by each panel.

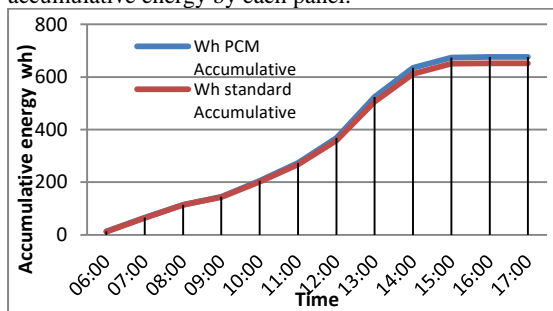


Figure 7. Accumulative energy generation on 16th of Nov

From these figures above it may be noticed that the energy gap between the PCM cooled panel and the standard panel is 3.6%, which is higher than the average energy gap for the whole experiment which was 2.6%.

From the above discussion, and based on the selected samples, on the extreme data collected and on the period of the experiment and location it may be concluded that as the temperature increases the energy gap between the cooled and the standard module will be less than the average energy gap for the total experiment. This means that lower performance than the average performance for the PCM cooled panels. While during the day with the lowest radiation and the day with the lowest average temperature the cooled PV by PCM showed a better performance than the average performance. This may be attributed to the capacity of storing energy in the PCM

On the other hand, on the lowest average temperature day (16th Nov., 2014), it was found that the maximum energy that can be absorbed within the PCM from the total energy delivered to the surface of the panel is 11.3% which will reflect positively on the performance of PCM cooled panel by absorbing a higher percentage of energy preventing it to increase the temperature of the PV panel.

Furthermore, it was observed that the PCM cooled panel showed lower performance compared with the standard panel when temperature and radiation dropped at the end of each day, which leads to the fact that the PCM is approaching the freezing temperature point and causing it to be a heat source and hence the PCM cooled panel temperature will be higher than the standard panel causing a drop in performance.

5. Conclusions

In this work, the effect of cooling PV panels using phase change materials was investigated by using a system. To achieve this, a system was designed and constructed, this consist of two identical panels of 250 Watt peak each and installed at a tilt angle of 26 and facing south, one of the PV panels is installed normally (without being cooled) and the other one is covered from the back side with PCM.

From this work, it may be concluded that the PCM cooled panel performed better than the standard panel, the stored data was analyzed and the main findings were that the cooled PV panel using PCM had performed 2.6% better than the standard panel.

Acknowledgment

The research would like to acknowledge that this research work was financially supported by the Deanship of research at Al-Zaytoonah University of Jordan

References

- [1] Tonui, J. & Tripanagnostopoulos, Y. 2007 a. Improved PV/T solar collectors with heat extraction by forced or natural air circulation. *Renewable Energy*, 32, 623-637.
- [2] Tonui, J. & Tripanagnostopoulos, Y. 2007 b. Air-cooled PV/T solar collectors with low cost performance improvements. *Solar Energy*, 81, 498-511.
- [3] Odeh, S. & Behnia, M. 2009. Improving photovoltaic module efficiency using water cooling. *Heat Transfer Engineering*, 30, 499-505.
- [4] Ming Jun Huang, 2011. The effect of using two PCMs on the thermal regulation performance of BIPV systems *Solar Energy Materials and Solar Cells*, Volume 95, Issue 3, March Pages 957-963.
- [5] Teo, H. Lee, P. & Hawlader, M. 2012. An active cooling system for photovoltaic modules. *Applied Energy*, 90, 309-315.
- [6] Dongliang Zhao, Gang Tan (2014) Experimental evaluation of a prototype thermoelectric system integrated with PCM (phase change material) for space cooling. *Energy*, Volume 68, Pages 658-666.
- [7] Hasan, A., McCormack, S. J., Huang, M. J. & Norton, B. 2014. Energy and Cost Saving Of A Photovoltaic-Phase Change Materials (Pv-Pcm) System Through Temperature Regulation And Performance Enhancement Of Photovoltaics. *Energies*, 7, 1318-1331.
- [8] Gang Tan, Dongliang Zhao (2015). Study of a thermoelectric space cooling system integrated with phase change material. *Applied Thermal Engineering* 86 187-198.
- [9] Zhongzhu Qiu, Xudong Zhao, Peng Li, Xingxing Zhang, Samira Ali, Junyi Tan (2015) Theoretical investigation of the energy performance of a novel MPCM (Microencapsulated Phase Change Material) slurry based PV/T module *Energy*, Volume 87, , Pages 686-698.
- [10] European Photovoltaic Industry Association (2013). *Global Market Outlook*, Germany.

MHD Tangent Hyperbolic Nanofluid with Zero Normal Flux of Nanoparticles at the Stretching Surface with Thermal Radiation

Ittedi Shravani^{a,*}, Dodda Ramya^b, Sucharitha Joga^a

^a Department of Mathematics, Government Degree College, Adilabad, 504001, Telangana State, India

^b Department of Mathematics, University College of Science, Osmania University, Hyderabad, 500007, Telangana State, India

Received 19 May 2018

Abstract

This article presents the effect of thermal radiation and slip effects on MHD boundary layer flow of tangent hyperbolic nanofluid over a stretching sheet and condition of zero normal flux of nano particles introduced at the surface. Similarity transformations are used to transform the governing partial differential equations in terms of continuity, momentum, energy, and concentration which are reconstructed into ordinary differential form and then solved numerically using Runge-Kutta fourth order method with shooting technique. The behavior of the involved physical parameters Weissen berg number (We), thermal radiation (R), Lewis number (Le), velocity slip (λ) and power law index (n) are displayed graphically for velocity, temperature, and concentration profiles. Additionally, local skin friction, local Nusselt number, and local Sherwood number are computed and analyzed. Comparison of the present results with previously published literature is specified and found in good agreement. The numerical results show that the skin friction increases and the Nusselt number as well, whereas the Sherwood numbers are decreasing with the increase in velocity slip parameter.

© 2018 Jordan Journal of Mechanical and Industrial Engineering. All rights reserved

Keywords: Tangent hyperbolic fluid, nanofluid, MHD, thermal radiation, partial slip effects;

1. Introduction

The steady flow over stretching sheet with heat transfer is a classical problem in fluid dynamics. In past few decades, boundary layer flows over stretching sheet got a lot of importance due to its occurrence in various engineering and mechanical processes, chemical and metallurgical processes like polymers pro-tuberating, glass blowing, paper and fiber glass production, metallic plate cooling, melt-spinning, hot rolling etc. Sakiadis [1] has discussed the study of the boundary layer flow over a continuous solid surface moving with constant speed. Crane [2] has extended the work for both linear and exponentially stretching sheet. Hayat *et al.* [3] examined the chemically reactive flow of third grade fluid by an exponentially convective stretching sheet. Vajravelu *et al.* [4] have studied the effects of thermo-physical property on unsteady flow and heat transfer in a Ostwald-de Waele liquid on a stretching sheet. Turkyilmazoglu [5] has derived the flow of a micropolar fluid due to a porous stretching sheet and heat transfer.

The study of MHD flow is very important as it has many industrial applications, such as magnetic materials processing, purification of crude oil, magneto hydrodynamic electrical power generation, glass manufacturing, geophysics, and paper production, and

many other practical applications such as magnetic field effects on wound healing, or cancer action causing hypothermia, surgical procedures and MRI (magnetic resonance imaging) to diagnose disease. Furthermore, the influence of the magneto hydrodynamic (MHD) flow due to a stretching sheet has enormous applications in modern metallurgy and chemical industry e.g. fusing of metals and cooling of nuclear reactors etc. Rashidi *et al.*[6] have analyzed the entropy analysis of convective MHD flow of third grade non-Newtonian fluid over a stretching sheet. MHD flow and heat transfer of couple stress fluid over an oscillatory stretching sheet with heat source/sink in porous medium has been studied by Nasir Ali *et al.*[7]. Hayat *et al.*[8] derived MHD axisymmetric flow of third grade fluid between stretching sheets with heat transfer. Rana and Bhargava [9] have analyzed similar research for a nonlinear stretching sheet using finite element and finite difference methods. Mabood *et al.*[10] introduced the MHD flow over exponential radiating stretching sheet using homotopy analysis method. Forced convection heat transfer in a semi annulus under the influence of a variable magnetic field derived by Sheikholeslami *et al.*[11]. Rashidi *et al.*[12] investigated the entropy generation in MHD and slip flow over a rotating porous disk with variable properties.

The term nanofluid used for suspensions which comprise the nano size particles (silver, gold, aluminum,

* Corresponding author e-mail: ittedi876@gmail.com.

copper, diamond etc.) and conventional base fluid. Firstly, Choi [13] introduced the term nanofluid. Today nanofluids are sought for wide range of applications in medical application, Biomedical industry, detergency, power generation in nuclear reactors and more specifically in any heat removal involved industrial applications. Micropolar nanofluid flow with MHD and viscous dissipation effects towards a stretching sheet with multimedia feature studied by Kai-Long Hsiao [14]. Ibrahim [15] analyzed the magnetohydrodynamic (MHD) boundary layer stagnation point flow and heat transfer of a nanofluid past a stretching sheet with melting. Mabood *et al.* [16] did a numerical study on MHD boundary layer flow and heat transfer of nanofluids over a nonlinear stretching sheet. Hayat *et al.* [17] have studied the flow of nanofluid by nonlinear stretching velocity.

The fluids are mainly classified into two categories: Newtonian and Non-Newtonian. Moreover, the analysis of heat transfer of non-Newtonian fluids plays a very important role in various industrial applications, such as in petroleum production and metallurgical process. Numerous materials excluding dyes, blood at low shear rate, ketchup, certain paints, lubricants, mud and personal care products are non-Newtonian in nature. Flow of non-Newtonian fluids has a pivotal role in manufacturing polymer devolatilisation, bubbles columns, fermentation, composite processing, boiling, plastic foam processing, and bubbles absorption etc. In the present research work, we will focus on the study of non-Newtonian fluid which is one of the important branches of non-Newtonian fluid i.e., hyperbolic tangent fluid which is useful for chemical engineering systems, and it has the capacity to describe shear thinning phenomena. Examples of tangent hyperbolic fluids are ketchup, whipped cream, blood, paint, and nail polish. Malik *et al.* [18] analyzed the MHD flow of tangent hyperbolic fluid over a stretching cylinder by using Keller box method. Prabhaker *et al.* [19] studied the impact of inclined Lorentz forces on tangent hyperbolic nanofluid flow with zero normal flux of nanoparticles at the stretching sheet. Hayat *et al.* [20] introduced magnetohydrodynamic (MHD) stretched flow of tangent hyperbolic nano liquid with variable thickness. Khan *et al.* [21] did a numerical investigation on boundary layer flow of MHD tangent hyperbolic nanofluid over a stretching sheet. Naseer *et al.* [22] derived the boundary layer flow of hyperbolic tangent fluid over a vertical exponentially stretching cylinder. Nadeem and Akram [23] studied the peristaltic transport of a hyperbolic tangent fluid model in an asymmetric channel.

Thermal radiation is important in some applications because of the way radiant emission depends on temperature and nanoparticle volume fraction. Thermal radiation is continuously emitted by all matter whose temperature is above absolute zero. Thermal radiation is also defined as the portion of the electromagnetic spectrum that extends from about 0.1 to 100 μm , since the radiation emitted by bodies due to their temperature falls almost entirely into this wave length range. Hayat *et al.* [24, 25] investigated on radiative flow of a tangent hyperbolic fluid with convective conditions. Mahanthesh *et al.* [26] analyzed nonlinear convective and radiated flow of tangent hyperbolic liquid due to stretched surface with convective condition. Rehman *et al.* [27] introduced mutual effects of

thermal radiations and thermal stratification on tangent hyperbolic fluid flow yields by both cylindrical and flat surfaces. Rashidi *et al.* [28] scrutinized the buoyancy effect on MHD flow of nanofluid over a stretching sheet in the presence of thermal radiation. Thermal radiation and MHD effects on boundary layer flow of micropolar nanofluid past a stretching sheet with non-uniform heat source/sink has been derived by Pal and Mandal [29]. Hayat *et al.* [30] have analyzed the new thermodynamics of entropy generation minimization with nonlinear thermal radiation and nanomaterials.

Slip effects on MHD boundary layer flow over an exponentially stretching sheet with suction/blowing and thermal radiation are studied by Swati Mukhopadhyay [31]. Thermal radiation and slip effects on MHD stagnation point flow of nanofluid over a stretching sheet are studied by Rizwan Ul Haq *et al.* [32]. MHD boundary layer flow and heat transfer of a nanofluid past a permeable stretching sheet with velocity, thermal and solutal slip boundary conditions have been discussed by Ibrahim and Shankar [33]. Hayat *et al.* [34] studied radial MHD and mixed convection effects in peristalsis of non-Newtonian nanomaterial with zero mass flux conditions. Rehman *et al.* [35] analyzed entropy generation analysis for non-Newtonian nanofluid with zero normal flux of nanoparticles at the stretching surface. Entropy generation in steady MHD flow due to a rotating porous disk in a nanofluid is studied by Rashidi *et al.* [36].

From above literature, the aim of the present study is to investigate the condition of zero normal flux for MHD tangent hyperbolic fluid flow towards a stretching sheet with thermal radiation. Mathematical model is structured for non-Newtonian fluid in the presence of slip mechanism of nanofluid. To discard the gravitational settling at the surface of the sheet, we have considered the passive control of nanoparticles at the surface which are defined in the boundary condition. The governing nonlinear partial differential systems are transformed into ordinary nonlinear differential equations. Here the Runge-Kutta fourth order method with shooting technique is applied to construct the series solution for the nonlinear governing problems. The effects of governing parameters on fluid velocity, temperature and particle concentration were discussed and shown in graphs and tables as well.

2. Tangent hyperbolic fluid model:

For an incompressible fluid the balance of mass and momentum are given by [23]

$$\text{div } V = 0, \quad (1)$$

$$\rho \frac{dV}{dt} = \text{div } S + \rho f \quad (2)$$

Where ρ is the density, V is the velocity vector, S is the Cauchy stress tensor, f represents the specific body force and $\frac{d}{dt}$ represents the material time derivative. The constitutive equation for hyperbolic tangent fluid is given by

$$S = -PI + \bar{\tau} \quad (3)$$

$$\bar{\tau} = -[\mu_{\infty} + (\mu_0 + \mu_{\infty}) \tanh(\Gamma \bar{\gamma})^n] \bar{\gamma}, \quad (4)$$

In which $-PI$ is the spherical part of the stress due to constraint of incompressibility, $\bar{\tau}$ is extra stress tensor, μ_{∞} is the infinite shear rate viscosity, μ_0 is the zero shear rate

viscosity, Γ is the time dependent material constant, n is the power law index, i.e., flow behavior index and $\bar{\gamma}$ defined as

$$\bar{\gamma} = \sqrt{\frac{1}{2} \sum_i \sum_j \bar{\gamma}_{ij} \bar{\gamma}_{ji}} = \sqrt{\frac{1}{2} \Pi}, \quad (5)$$

Where $\Pi = \frac{1}{2} \text{tr}(\text{grad}V + \text{grad}V^T)^2$. Here Π is the second invariant strain tensor. We consider Eq. (4), the case for which $\mu_\infty = 0$ because it is not possible to discuss the problem for the infinite shear rate viscosity and since we are considering tangent hyperbolic fluid that describing shear thinning effects so $\Gamma \bar{\gamma} < 1$. Then Eq.(4) takes the form

$$\bar{\tau} = -\mu_0 [(\Gamma \bar{\gamma})^n] \bar{\gamma} = -\mu_0 [(1 + \Gamma \bar{\gamma} - 1)^n] \bar{\gamma} \quad (6)$$

$$\bar{\tau} = -\mu_0 [1 + n(\Gamma \bar{\gamma} - 1)] \bar{\gamma}$$

3. Mathematical formulation

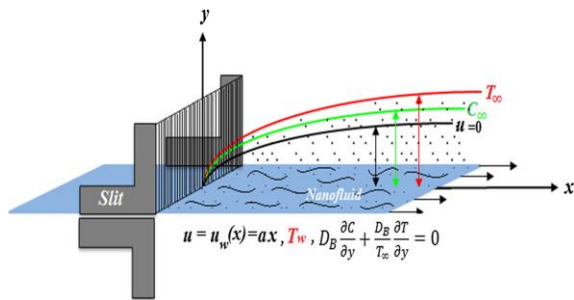


Figure 1. Geometry of the model.

Consider the steady, viscous, two-dimensional and incompressible boundary layer flow of tangent hyperbolic nano fluid over a stretching sheet with surface at $y = 0$ which is stretching linearly with velocity $u_w = ax$. The flow lies in the region $y > 0$ and magnetic field of strength B_0^2 is applied normal to the flow. It is assumed that at the stretching surface, the temperature and the nano particles fraction take constant values T_w and C_w whereas the ambient values of temperature T_∞ and the nanoparticles fraction C_∞ are attained as y tends to infinity. Taking all these assumptions into account, the governing equations under boundary layer assumptions are given below[23] :

$$\frac{\partial u}{\partial x} + \frac{\partial v}{\partial y} = 0, \quad (7)$$

$$u \frac{\partial u}{\partial x} + v \frac{\partial u}{\partial y} = v(1-n) \frac{\partial^2 u}{\partial y^2} + \sqrt{2} \nu n \Gamma \frac{\partial u}{\partial y} \frac{\partial^2 u}{\partial y^2} - \frac{\sigma B_0^2(x)}{\rho_f} u, \quad (8)$$

$$u \frac{\partial T}{\partial x} + v \frac{\partial T}{\partial y} = \alpha_m \frac{\partial^2 T}{\partial y^2} + \tau \left\{ D_B \frac{\partial C}{\partial y} \frac{\partial T}{\partial y} + \frac{D_T}{T_\infty} \left(\frac{\partial T}{\partial y} \right)^2 \right\} - \frac{1}{(\rho c)_f} \frac{\partial q_r}{\partial y}, \quad (9)$$

$$u \frac{\partial C}{\partial x} + v \frac{\partial C}{\partial y} = D_B \frac{\partial^2 C}{\partial y^2} + \left(\frac{D_T}{T_\infty} \right) \frac{\partial^2 T}{\partial y^2}. \quad (10)$$

here u and v are the velocity components along the x and y directions, respectively, ρ_f the density of the base fluid, $\alpha_m = k/(\rho c)_f$ the thermal diffusivity, ν the kinematic viscosity, Γ is the time constant, n is the power law index, T is the fluid temperature, c_p is the specific heat, D_B the Brownian diffusion coefficient, D_T the thermophoretic diffusion coefficient, $\tau = \frac{(\rho c)_p}{(\rho c)_f}$ the ratio between the effective heat capacity of the nanoparticle material and heat capacity of the fluid and ρ the density of the particles.

Using Rosseland approximation for radiation we can write

$$q_r = -\frac{4\sigma^* \partial T^4}{3k^* \partial y} \quad (11)$$

Where σ^* is the Stefan-Boltzman constant, k^* is the absorption coefficient. Assuming that the temperature difference within the flow is such that T^4 may be expanded in a Taylor series and expanding T^4 about T_∞ , the free stream temperature and neglecting higher orders we get

$$T^4 \approx 4T_\infty^3 T - 3T_\infty^4.$$

We introduce subjective boundary conditions are $u = u_w(x) + \gamma_1 \frac{\partial u}{\partial y}$, $v = 0$, $T = T_w$, $D_B \frac{\partial C}{\partial y} + \frac{D_B \partial T}{T_\infty \partial y} = 0$ as $y = 0$ (Zero normal flux)
 $u = 0$, $T = T_\infty$, $C = C_\infty$ as $y \rightarrow \infty$ (12)

The similarity transformations for this problem can be written as

$$\eta = y \sqrt{\frac{a}{\nu}}, u = ax f'(\eta), v = -\sqrt{av} f(\eta), \quad (13)$$

$$\theta(\eta) = \frac{T - T_\infty}{T_w - T_\infty}, \phi(\eta) = \frac{C - C_\infty}{C_\infty}.$$

After applying the above-defined transformations into governing equations, they take the following form

$$((1-n) + n We f'') f''' - f'^2 + f f'' - M^2 f' = 0, \quad (14)$$

$$(1 + \frac{4}{3} R) \theta'' + Pr(f \theta' + Nb \phi' \theta' + Nt \theta'^2) = 0, \quad (15)$$

$$\phi'' + Pr Le f' \phi' + \frac{Nt}{Nb} \theta'' = 0. \quad (16)$$

Transformed boundary conditions

$$f(0) = 0, f'(0) = 1 + \lambda f''(0), \theta(0) = 1, Nb \phi'(0) + Nt \theta'(0) = 0, \quad (17)$$

$$f'(\infty) = 0, \theta(\infty) = 0, \phi(\infty) = 0.$$

where prime denotes differentiation with respect to η . The dimensionless parameters $Nb, Nt, Pr, Le, M, We, R, \lambda$ are the Brownian motion parameter, thermophoresis parameter, Prandtl, Lewis, the magnetic parameter, Weissenberg number, thermal radiation parameter, velocity slip parameter, respectively. These parameters are defined as follows:

$$Nb = \frac{(\rho c)_p D_B C_\infty}{(\rho c)_f \nu}, Nt = \frac{(\rho c)_p D_T (T_w - T_\infty)}{(\rho c)_f \nu T_\infty}, Pr = \frac{\nu}{\alpha_m}, Le = \frac{\alpha_m}{D_B}, M = \frac{\sigma B_0^2}{\rho_f a}, \quad (18)$$

$$We = \frac{\sqrt{2} a^{3/2} \Gamma x}{\sqrt{\nu}}, R = \frac{k k^*}{4 \sigma^* T_\infty^3}, \lambda = \gamma_1 \sqrt{\frac{a}{\nu}}.$$

The physical quantities of interest are the skin friction C_f and the local Nusselt number Nu_x which are defined as

$$C_f = \frac{\tau_w}{\rho u_w^2}, Nu_x = \frac{x q_w}{k(T_w - T_\infty)} \quad (19)$$

Where the surface shear stress τ_w and the heat flux q_w are given as

$$\tau_w = (1-n) \left(\frac{\partial u}{\partial y} \right)_{y=y_0} + \frac{n \Gamma}{\sqrt{2}} \left(\frac{\partial u}{\partial y} \right)_{y=y_0}^2,$$

$$q_w = -k \left(\frac{\partial T}{\partial y} \right)_{y=0} + (q_r)_w \quad (20)$$

Substituting Eq. (13) into Eqs. (19)- (20), we obtain

$$Re_x^{1/2} C_f = (1-n) f''(0) + \frac{n We}{2} (f''(0))^2,$$

$$\frac{Nu_x}{Re_x^{1/2}} = -(1 + \frac{4}{3} R) \theta'(0) \quad (21)$$

where $Re_x = (ax^2/\nu)$ is the local Reynolds number.

4. Numerical Procedure

The system of coupled non-linear ordinary differential equations (14) - (16) along with the boundary conditions (17), which are solved numerically by Runge-Kutta fourth order method with shooting technique. The step size is taken as $\Delta\eta = 0.01$ and the convergence criteria were set to 10^{-5} . Computational time is 1.569 s. The asymptotic boundary conditions defined in Eq.(17) are replaced by $f(\eta_{max}) = 1$ using a value similarity variable $\eta_{max} = 15$. The choice of $\eta_{max} = 15$ ensures that all numerical solutions approached the asymptotic values correctly.

5. Results and discussion

The coupled nonlinear ordinary differential Eqs.(14)-(16), subjected to the boundary conditions (17) have been calculated using Runge-Kutta fourth order method with shooting technique. Here the numerical solutions of tangent hyperbolic fluid for stretching sheet are presented. The dimensionless parameters including, magnetic parameter (M), Prandtl number (Pr), Brownian motion parameter (Nb), thermophoresis parameter (Nt), thermal radiation R , velocity slip parameters λ are the main interests of the study. The numerical values of local skin friction are exhibited in Table1. The present results show a good agreement with the published data. From Table 2, the Nusselt number is a decreasing function of increasing R , and Sherwood number is found to be an increasing function of R .

Table 1. Comparison of local skin friction coefficient in the absence of nanoparticles, Weissenberg number $We = 0$.

M	Akbar et al.[37]	Malik et al.[18]	Hussain et al.[38]	Khan et al.[21]	Present results
0	-1	-1	-1	-1	-1.00017
1	-1.41421	-1.41419	-1.4137	-1.4139	-1.41421
5	-2.449449	-2.44945	-2.4495	-2.4499	-2.44949
10	-3.31663	-3.31657	-3.3166	-3.3170	-3.31662
100	-10.0498	-10.04981	-10.0500	-10.0503	-10.04988
500	-22.38303	-22.38294	-22.3835	-22.3839	-22.38303
1000	-31.63859	-31.63851	-31.6391	-31.6399	-31.63858

Table 2. Calculation of $-f''(0), -\theta'(0)$ and $-\phi'(0)$ when $Pr = 1.0, Le = 1.0, M = 0.5, Nb = 0.2, Nt = 0.3, We = n = 0.1$.

R	λ	$Re_x^{1/2} C_f$	$-\theta'(0)$	$-\phi'(0)$
0.0		-1.10901	0.47841	-0.71762
0.5	0.1	-1.10901	0.33929	-0.50894
1.0		-1.10901	0.27901	-0.41852
	0.2	-0.97330	0.32343	-0.48514
0.5	0.3	-0.86987	0.31053	-0.46580
	0.5	-0.72127	0.29055	-0.43583

Figure.2 illustrates the effect of power law index on velocity, temperature and concentration profiles. It is noticeable that an increase in the values of power-law index n correspond to reduction in velocity and boundary layer thickness, and it is also observed that the fluid nature changes from shear thinning to shear thickening. Hence velocity profile shows the decreasing behavior while

temperature and concentration profile are increasing with increasing values of power law index. The influence of the Weissenberg number We on the velocity, temperature and concentration profiles are presented in figure 3. An increase in the values of Weissenberg number We correspond to the decrease in velocity of the flow and thinning of hydrodynamic boundary layer since We is the ratio of the shear rate time to the relaxation time of the fluid. Hence with the increase of the Weissenberg number We the relaxation time increases, which produces more resistance to the motion of the fluid and thus the velocity profile decreases. But the reverse behavior is obtained for temperature and concentration profiles. Figure 4, illustrates the effect of magnetic parameter on velocity, temperature and concentration profiles. It shows that velocity profile decreases with an increase in magnetic parameter. The existence of magnetic field produces a force called Lorentz force and it resists the fluid motion and therefore some useful energy is converted into heat. Therefore the flow velocity is decreased but temperature and concentration are enhanced with increasing values of M . Effect of Brownian motion parameter Nb on nanoparticle concentration is observed in Figure 5, from the figure we can seen that nanoparticle concentration is found to decrease and the concentration boundary layer thickness decreases with an increase in the Brownian motion parameter Nb , due to an increase in Brownian motions causes irregular movement of nanoparticles, hence it ultimately deprecates the nanoparticle concentration.

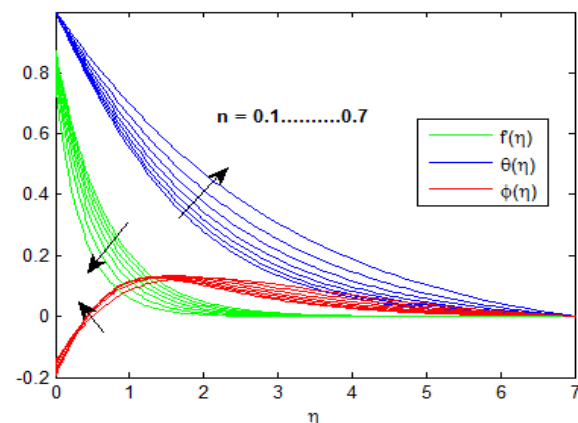


Figure 2. Effect of n on velocity, temperature and concentration profiles.

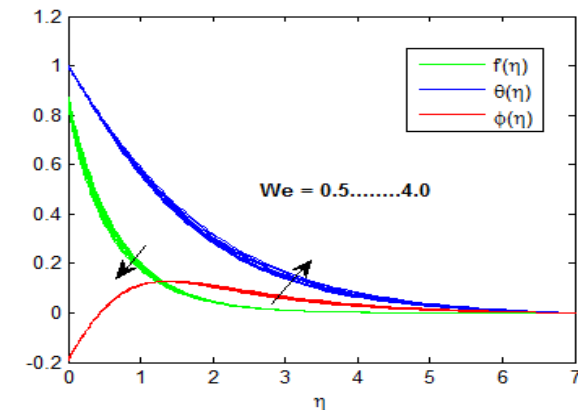


Figure 3. Effect of We on velocity, temperature and concentration profiles.

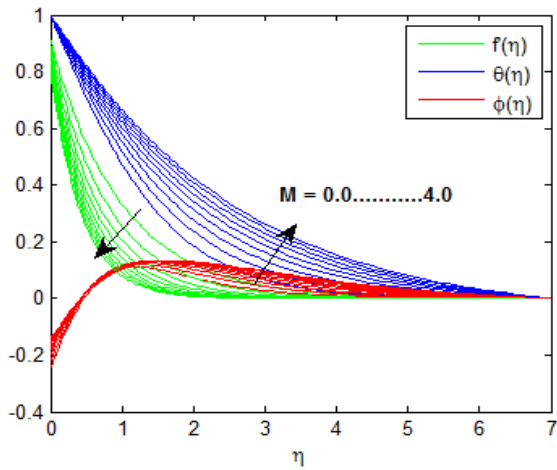


Figure 4. Effect of M on velocity, temperature and concentration profiles.

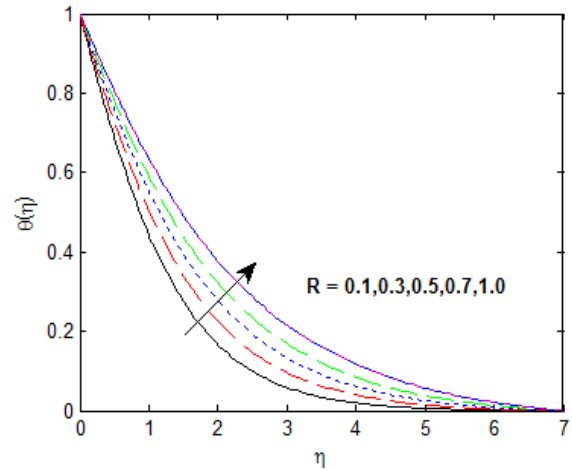


Figure 8. Effect of R on temperature profile.

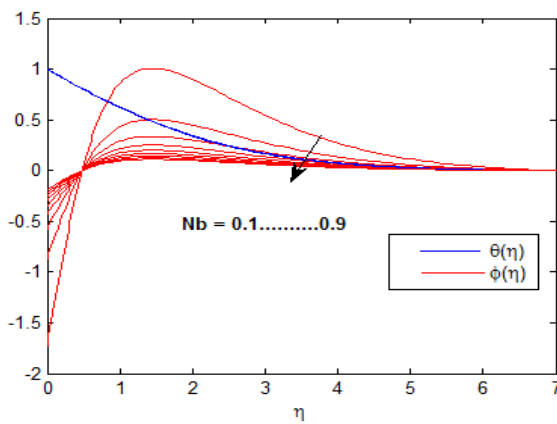


Figure 5. Effect of Nb on temperature and concentration profiles.

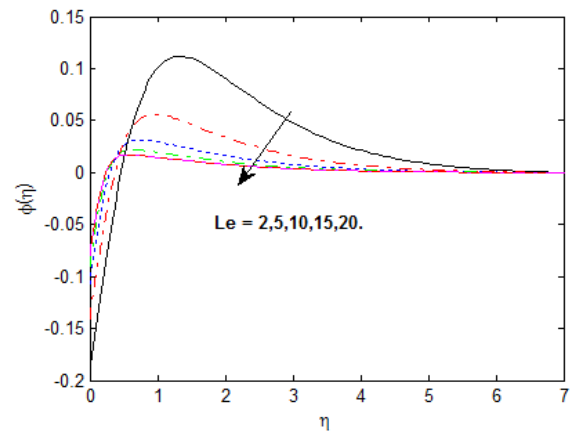


Figure 9. Effect of Le on concentration profile.

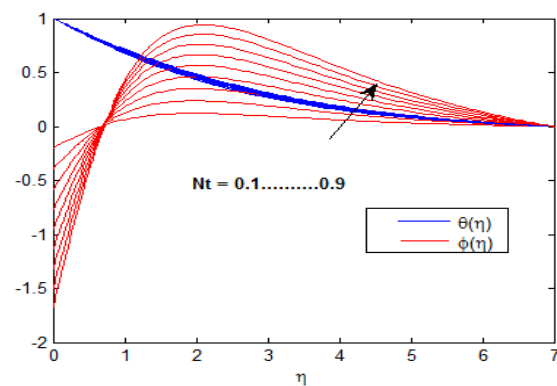


Figure 6. Effect of Nt on temperature and concentration profiles.

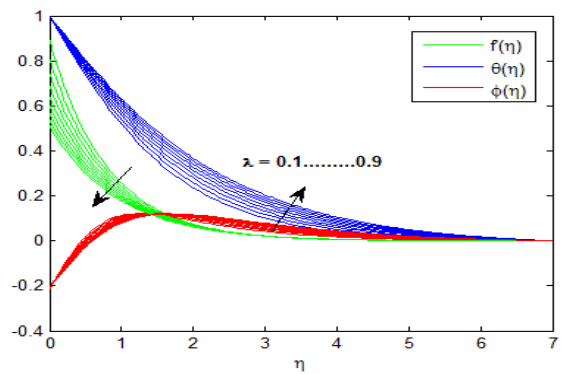


Figure 10. Effect of λ on velocity, temperature and concentration profiles.

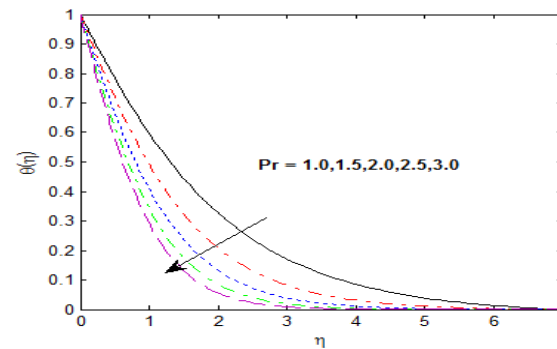


Figure 7. Effect of Pr on temperature profile.

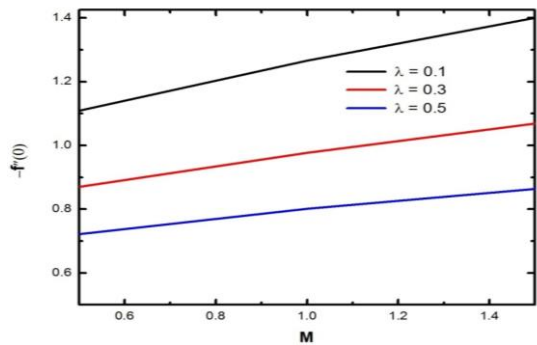


Figure 11. Variation of skin friction with various values of M and λ

Figure 6 depicts the impact of thermophoresis parameter Nt on temperature and nanoparticle concentration profiles. From the figure, large values of thermophoresis parameter Nt temperature profile as well as nanoparticle concentration profile increases. It is observed that for large values of thermophoresis parameter Nt , nanoparticles migrated from the hot surface to cold ambient fluid, as a result the thermal boundary layer thickness enhances. Figure 7 shows the influence of Prandtl number Pr on temperature profile. Here we observed that the temperature profile decreases by increasing Pr . In fact when Pr increases then thermal diffusivity decreases. This indicates diminution in energy transfer ability and decrease of thermal boundary layer thickness. Influence of thermal radiation R on temperature profile is shown in Figure 8. Here we observed that when the thermal radiation R increases then the temperature profile enhanced. For large values of radiation parameter, generates a significant amount of heating to the nanofluid which increases the nanofluid temperature profile and thicker thermal boundary layer thickness. Influence of Lewis number Le on concentration profile is shown in Figure 9. As Lewis number increases the concentration graph decreases and the concentration boundary layer thickness decreases. This is because for larger Lewis number Le , the Brownian diffusion is weaker, which leads to weak mass transfer as a result, the thinner concentration boundary layer at the surface.

Figure 10 illustrates the effect of velocity slip parameter on velocity, temperature and concentration profiles. An increase in the velocity slip parameter λ corresponds to a decrease in the relative velocity of the fluid and the stretching sheet. Increasing λ decreases the velocity because under the slip condition, the pulling of the stretching sheet can be only partly transmitted to the fluid. The boundary layer thickness also decreases as the slip parameter λ increases. In this figure, we also observed that as the value of velocity slip parameter increases the temperature profile as well as concentration profile increases. Results produced for skin friction are analyzed for magnetic parameter and velocity slip parameter λ in Figure 11. It can be found that decreasing the skin friction for increasing velocity slip parameter (λ).

6. Conclusions

In general, the effect of thermal radiation, velocity slip, Weissenberg number, power-law index parameter and magnetic field on boundary layer flow and heat transfer of tangent hyperbolic fluid with zero normal flux of nanoparticles past a stretching sheet have been discussed. The boundary layer equations governing the flow problem are reduced into a couple of high order non-linear ordinary differential equations using the similarity transformation. The obtained differential equations are solved numerically using Runge-Kutta fourth order method with shooting technique from Matlab software. The effects of various governing parameters such as velocity slip parameters λ , magnetic parameter M , radiation parameter R , Prandtl number Pr , Brownian motion parameter Nb , thermophoresis parameter Nt and Lewis number parameter Le on momentum, energy and concentration

equation are analyzed using figures and tables. The observations of the present study are as follows:

1. By increasing the values of velocity slip parameter λ , Weissenberg number We , power-law index n and magnetic parameter M on velocity, temperature and concentration profiles, there happens a reduction in velocity profile and increase in the temperature and concentration profiles.
2. Increase in Prandtl number Pr leads to decrease in the temperature profile.
3. Nanoparticle concentration decreases with an increase in Brownian motion parameter Nb .
4. As the thermophoresis parameter Nt enhances, both temperature and concentration profile increase.
5. Concentration profile is reduced when the Lewis number Le increased.
6. Temperature profile is increased with the increasing values of thermal radiation parameter R .

Acknowledgements

The first author is very thankful to University Grants Commission, India, for providing the opportunity to do this research work under UGC-Faculty Development Programme (FDP), India.

References

- [1] Sakiadis, B.C., Boundary-layer behavior on continuous solid surface: I. Boundary-layer equations for two-dimensional and axisymmetric flow. *American Institute of Chemical Engineers Journal*, Vol.7, pp 26-28.
- [2] L.J. Crane, Flow past a stretching plate, *ZAMP* 21 (1970) 2.
- [3] T.Hayat, M.Waqas, S.A.Shehzad, A.Alsaedi, Chemically reactive flow of third grade fluid by an exponentially convected stretching sheet, *Journal of Molecular Liquids*, Volume 223, November 2016, Pages 853-860.
- [4] Vajravelu K, Prasad KV, Chiu-On Ng. Unsteady flow and heat transfer in a thin film of Ostwald-de Waele liquid over a stretching surface, *Commun Nonlinear Sci Numer Simul* 2012;17: 4163-73.
- [5] M.Turkyilmazoglu, the flow of a micropolar fluid due to a porous stretching sheet and heat transfer, *International Journal of Non-Linear Mechanics*, Volume 83, July 2016, Pages 59-64.
- [6] M.M.Rashidi, S.Bagheri, E.Momoniati, N.Freidoonimehr, Entropy analysis of convective MHD flow of third grade non-Newtonian fluid over a stretching sheet, *Ain Shams Engineering Journal*, Volume 8, Issue 1, March 2017, Pages 77-85.
- [7] NasirAli, SamiUllah Khan, Muhammad Sajid, ZaheerAbbas, MHD flow and heat transfer of couple stress fluid over an oscillatory stretching sheet with heat source/sink in porous medium, *Alexandria Engineering Journal*, Volume 55, Issue 2, June 2016, Pages 915-924.
- [8] T.Hayat, A.Shafiq, A.Alsaedi, M.Awais, MHD axisymmetric flow of third grade fluid between stretching sheets with heat transfer, *Computers & Fluids*, Volume 86, 5 November 2013, Pages 103-108.
- [9] Rana, P., Bhargava, R., Flow and heat transfer of a nanofluid over a nonlinearly stretching sheet: a numerical study, *Commun. Nonlinear Sci.Numer.Simul*, Vol.17, pp 212-226, 2012.
- [10] Fazle Mabood, W.A.Khan, A.I.Md.Ismail, MHD flow over exponential radiating stretching sheet using homotopy analysis method, *Journal of King Saud University*

- Engineering Sciences*, Volume 29, Issue 1, January 2017, Pages 68-74.
- [11] Mohsen Sheikholeslami, Kuppapalle Vajravelu, Mohammad Mehdi Rashidi, Forced convection heat transfer in a semi annulus under the influence of a variable magnetic field, *International Journal of Heat and Mass Transfer*, Volume 92, January 2016, Pages 339-348.
- [12] M.M.Rashidi, N.Kavyani, S.Abelman, Investigation of entropy generation in MHD and slip flow over a rotating porous disk with variable properties, *International Journal of Heat and Mass Transfer*, Volume 70, March 2014, Pages 892-917.
- [13] Choi, S. U. S., Enhancing Thermal Conductivity of Fluids with Nanoparticles, *Proceedings, ASME International Mechanical Engineering Congress and Exposition*, San Francisco, Cal., USA, ASME, FED 231/MD 66, (1995), pp. 99-105.
- [14] Kai-Long Hsiao, Micropolar nanofluid flow with MHD and viscous dissipation effects towards a stretching sheet with multimedia feature, *International Journal of Heat and Mass Transfer*, Volume 112, September 2017, Pages 983-990.
- [15] Ibrahim, Magnetohydrodynamic (MHD) boundary layer stagnation point flow and heat transfer of a nanofluid past a stretching sheet with melting, *Propulsion and Power Research*, Volume 6, Issue 3, September 2017, Pages 214-222.
- [16] F.Mabood, W.A.Khan, A.I.M.Ismail, MHD boundary layer flow and heat transfer of nanofluids over a nonlinear stretching sheet: A numerical study, *Journal of Magnetism and Magnetic Materials*, Volume 374, 15 January 2015, Pages 569-576.
- [17] Tasawar Hayat, Madiha Rashid, Ahmed Alsaedi, Bashir Ahmad, Flow of nanofluid by nonlinear stretching velocity, *Results in Physics*, Available online 9 January 2018, In Press, <https://doi.org/10.1016/j.rinp.2017.12.014>.
- [18] M.Y.Malik, T.Salahuddin, Arif Hussain, S.Bilal, MHD flow of tangent hyperbolic fluid over a stretching cylinder: Using Keller box method, *Journal of Magnetism and Magnetic Materials*, Volume 395, 1 December 2015, Pages 271-276.
- [19] Besthapu Prabhakar, Shankar Bandari, Rizwan Ul Haq, Impact of inclined Lorentz forces on tangent hyperbolic nanofluid flow with zero normal flux of nanoparticles at the stretching sheet, *Neural Computing and Applications*, May 2018, Volume 29, Issue 10, pp 805-814.
- [20] T.Hayat, M.Waqas, A.Alsaedi, G.Bashir, F.Alzahrani, Magnetohydrodynamic (MHD) stretched flow of tangent hyperbolic nanofluid with variable thickness, *Journal of Molecular Liquids*, Volume 229, March 2017, Pages 178-184.
- [21] Mair Khan, Arif Hussain, M.Y.Malik, T.Salahuddin, Farzana Khan, Boundary layer flow of MHD tangent hyperbolic nanofluid over a stretching sheet: A numerical investigation, *Results in Physics*, Volume 7, 2017, Pages 2837-2844.
- [22] Muhammad Naseer, Muhammad Yousaf Malik, Sohail Nadeem, Abdul Rehman, The boundary layer flow of hyperbolic tangent fluid over a vertical exponentially stretching cylinder, *Alexandria Engineering Journal*, Volume 53, Issue 3, September 2014, Pages 747-750.
- [23] Sohail Nadeem and Safia Akram, Peristaltic Transport of a Hyperbolic Tangent Fluid Model in an Asymmetric Channel, *Z. Naturforsch.* 64a, 2009, 559 – 567.
- [24] Tasawar Hayat, Sajid Qayyum, Ahmed Alsaedi, Sabir Ali Shehzad, Nonlinear thermal radiation aspects in stagnation point flow of tangent hyperbolic nanofluid with double diffusive convection, *Journal of Molecular Liquids*, Volume 223, November 2016, Pages 969-978.
- [25] Tasawar Hayat, Sajid Qayyum, Bashir Ahmad, Muhammad Waqas, Radiative flow of a tangent hyperbolic fluid with convective conditions and chemical reaction, *The European Physical Journal Plus*, December 2016, 131:422.
- [26] B.Mahanthesh, P.B. Sampath Kumar, B.J.Gireesha, S.Manjunatha, R.S.R.Gorla, Nonlinear convective and radiated flow of tangent hyperbolic liquid due to stretched surface with convective condition, *Results in Physics*, Volume 7, 2017, Pages 2404-2410.
- [27] Khalil Ur Rehman, Aneeqa Ashfaq Malik, M.Y.Malik, Noor Ul Saba, Mutual effects of thermal radiations and thermal stratification on tangent hyperbolic fluid flow yields by both cylindrical and flat surfaces, *Case Studies in Thermal Engineering*, Volume 10, September 2017, Pages 244-254.
- [28] M.M.Rashidi, N.Vishnu Ganesh, A.K.Abdul Hakeem, B.Ganga, Buoyancy effect on MHD flow of nanofluid over a stretching sheet in the presence of thermal radiation, *Journal of Molecular Liquids*, Volume 198, October 2014, Pages 234-238.
- [29] Dulal Pal, Gopinath Mandal, MHD effects on boundary layer flow of micropolar nanofluid past a stretching sheet with non-uniform heat source/sink, *International Journal of Mechanical Sciences*, Volume 126, June 2017, Pages 308-318.
- [30] T.Hayat, M.Ijaz Khan, Sumaira Qayyum, A.Alsaedi, M.Imran Khan, New thermodynamics of entropy generation minimization with nonlinear thermal radiation and nanomaterials, *Physics Letters A*, Volume 382, Issue 11, 23 March 2018, Pages 749-760.
- [31] Swati Mukhopadhyay, Slip effects on MHD boundary layer flow over an exponentially stretching sheet with suction/blowing and thermal radiation, *Ain Shams Engineering Journal*, Volume 4, Issue 3, September 2013, Pages 485-491.
- [32] Rizwan Ul Haq, Sohail Nadeem, Zafar Hayat Khan, Noreen Sher Akbar, Thermal radiation and slip effects on MHD stagnation point flow of nanofluid over a stretching sheet, *Physica E: Low-dimensional Systems and Nanostructures*, Volume 65, January 2015, Pages 17-23.
- [33] Wubshet Ibrahim, Bandari Shankar, MHD boundary layer flow and heat transfer of a nanofluid past a permeable stretching sheet with velocity, thermal and solutal slip boundary conditions, *Computers & Fluids*, Volume 75, 20 April 2013, Pages 1-10.
- [34] T.Hayat, S.Farooq, A.Alsaedi, B.Ahmad, Numerical analysis for radial MHD and mixed convection effects in peristalsis of non-Newtonian nanomaterial with zero mass flux conditions, *Results in Physics*, Volume 7, 2017, Pages 451-458.
- [35] Sajjad-ur Rehman, Rizwan-ul Haq, Zafar Hayat Khan, Changhoon Lee, Entropy generation analysis for non-Newtonian nanofluid with zero normal flux of nanoparticles at the stretching surface, *Journal of the Taiwan Institute of Chemical Engineers*, Volume 63, June 2016, Pages 226-235.
- [36] M.M.Rashidi, S.Abelman, N.Freidooni Mehr, Entropy generation in steady MHD flow due to a rotating porous disk in a nanofluid, *International Journal of Heat and Mass Transfer*, Volume 62, July 2013, Pages 515-525.
- [37] Akbar NS, Ebai A, Khan ZH. Numerical analysis of magnetic field effects on Eyring-Powell fluid flow towards a stretching sheet, *J Magn Magn Mater*, 2015;382:355-8.
- [38] Hussain Arif, Malik MY, Awais M, Salahuddin T, Bilal S. Computational and physical aspects of MHD Prandtl-Eyring fluid flow analysis over a stretching sheet, *Neural Comput Appl*, 2017. <http://dx.doi.org/10.1007/s00521-017-3017-5>.

Proposed Inventory Strategy of NSR Material in Cikarang-Indonesia Oil and Gas

Services Company

Atma Yudha Prawira^{a,*}, Euis Nina Saparina Yuliani^a, Hardianto Iridiastadi^b

^a Master of Industrial Engineering Department, Universitas Mercu Buana, 11650 Jakarta, Indonesia

^b Doctoral Programme of Industrial Engineering, Bandung Institute of Technology, 40132 Indonesia

Received 7 Feb. 2018

Abstract

The main purpose of this article is to present the inventory control model to determine the most reasonable amount of stock. The amount of stock exceeding or less than the requirement gives adverse impact to the company. With the current inventory system Oil and Gas Services, companies often experience the amount of NSR (Neutron Source Radioactive) supplies that exceed their needs. This is due to the number of orders provided to the supplier set based on various things such as anticipated safety stock, improper accuracy in the estimated needs, and projected lead time of arrival of goods. If the amount of inventory is too large, the amount of funds that must be spent by the company will also increase, in addition to increased storage costs, and an increased risk of damage to goods. However, if too little causing cessation of production processes, delays in profits can happen, or even loss of customers. The most reasonable inventory level improvement is done through stock optimization methods such as EOQ (Economic Order Quantity) model, Newsvendor Model, Lot-Sized Reorder Point System, and Service Level in Q and R System. With these inventory modes, the most reasonable inventory level can be found.

© 2018 Jordan Journal of Mechanical and Industrial Engineering. All rights reserved

Keywords: NSR Material, Overstock, Inventory Cost, Inventory Strategy, Stock Optimization;

1. Introduction

The main purpose of inventory control is that the company can always have an inventory for the right amount of goods, the right type, the right time, and in the specified specification or quality [2,25]. So, the result is that the cost incurred to hold inventory is the most reasonable. If the amount of inventory is too large, the amount of funds to be spent by the company, the cost of storage (such as personnel costs, operational costs, building costs, etc.) as well as the risk of damage to goods can all increase. However, too little inventory leads to a risk of stock running out as often inventory items cannot be brought in unexpectedly which may result in cessation of production processes, delays in profits, and even loss of customers. This is certainly not expected by the company because the loss of customers is the worst situation for any company.

The same problem is also experienced by an oil and gas service company in Cikarang which is a leading company in the field of oil and gas services industry. Oil and gas services companies play an important role in exploration and exploitation activities. Petroleum exploration or search is a long study involving several fields of study of earth and exact science. For basic study, research is done by geologists, those who master earth science. They are the ones who are responsible for the search for the hydrocarbons. While exploitation means actively and

efficiently utilizing oil and gas wells maximally so it can be made as the most reasonable [1].

To do the drilling and logging, sophisticated technological equipment is required. Each company has its own technology that will continue to compete, and thus it reflects on its reliability as to provide drilling and logging services. This tech logging equipment uses NSR material which is then incorporated into a drilling tool that is useful for reading the structure of rocks in the soil. Therefore, the NSR material plays an important role in the well logging process to obtain data from the soil tested which is then used to plan the next drier process.

In 2014, based on the Brent Crude Oil price, there was a decrease of world oil price per barrel, it also caused the decrease of oil and gas exploration activity in the world, and in Indonesia in particular. Based on data obtained from monthly demand reports of NSR materials to a drilling site by a Cikarang Oil and Gas Services Company, in 2014 the company experienced a decrease in demand for NSR materials to 21-units on average each month. This number continues to decline by 2015, the average demand for NSR material decreases to 14 units per month. And in December 2016 the demand for the number of NSR materials to the drilling sites was only 5-unit only, as shown in Figure 1.

The company's inventory management system currently uses a traditional approach by assuming that the uncertainty of consumer demand leads to production and purchase uncertainties so that the firm must have a large

* Corresponding author e-mail: atma.yudha.prawira@gmail.com.

supply. Management seeks to overcome these uncertainties through the best possible dosage planning. In this approach the assumption that production problems can be overcome by managing inventories. There are several reasons that encourage companies to use traditional approaches as they need inventories to balance storage and ordering costs, satisfy customer demand, take advantage of rebates, keep watch in case of price increases, and maintain the smoothness of the production process. Under current conditions, the company has an excess stock for existing NSR materials in storage bunkers.

With the current inventory system, the company accumulates 30 units of NSR material, assuming as a safety stock and assuming that the demand for materials or products is not known for certain, the likelihood of a supply shortage arises. According to Hansen and Maryanne [5,19], safety stock is an extra supply that is kept as collateral in the face of a demand that keeps fluctuating. Excess inventory on the company will result in increased cost of inventory management. Conversely, if there is a shortage of inventory, it will increase the risk of delay in operations that resulted in the company lost. Radioactive Neutron Source Material (NSR) is a material that serves to read the formation of the borehole using high-energy epithermal neutrons which then decreases its energy due to elastic scattering to the thermal level moments before being absorbed by the formation nucleus. With neutron logging technology itself can capture gamma rays, thermal neutron scattering, and high energy epithermal neutrons can be detected [4]. Note that neutron porosity is usually sensitive to the quantity of hydrogen atoms in certain formations, which are generally associated with rock porosity.

Nahmias [3,20] states that there are several factors affecting inventory levels, namely: estimates of raw material usage, raw material prices, inventory costs, spending policies, materials usage, waiting times, material purchase models, safety stocks and repurchases. Furthermore, there are two types of inventory controls that are used to be used on the basis of demand. For example, inventory control for known requests and inventory controls for changing demand. Nahmias [3,6,7] also states that there are some inventory strategies that can be used among them EOQ (Economic Order Quantity) is one of the inventory management models, EOQ (Economic Order Quantity) model is used to determine the quantity of inventory orders that can minimize storage costs and inventory ordering costs. Then Newsvendor Model, is a mathematical model in operations management used to determine the most reasonable order quantity of goods. This is usually characterized by fixed price and uncertain product demand. Another is Lot-Sized Reorder Point System, which is a system that uses inventory levels as a

trigger for ordering supplies. The company must set the minimum number of items held in the warehouse, so that when the inventory reaches the minimum, the item must be ordered again. And other strategies such as Q and R Service Level System is a system by determining the amount of optimum inventory in one order cycle to avoid stock-out cost.

From some of the above-mentioned inventory concepts seem to be able to solve inventory problems faced by the company. But not yet known which model is the most reasonable. The most reasonable model in question is an inventory model that can provide the highest level of availability and the lowest cost of inventory. This study will combine the four concepts of inventory to obtain the most reasonable inventory model.

2. Material and Method

Inventory or inventory within a company is the stock of goods used to meet customer demand and to facilitate the production process. Inventory can be divided into several types, such as raw materials, work in process, finished goods, and maintenance goods (repair, repair and operating supplies). Inventory is calculated as one type of corporate wealth so it requires a large capital (capital) to procure / purchase. On the one hand inventory is a burden to the company's finances, but on the other hand inventory availability is a must for the operation / production process to run smoothly and consumer / customer demand can be fulfilled [23-25].

Ben-Daya and Hariga [9,21] states that in general the types of inventory contained in manufacturing companies are divided into three groups, namely: Inventory of raw materials, Work in process inventory, and finished goods. Kogan and Lou [10] define inventory management as inventory management including planning, coordinating, and controlling activities related to the flow of incoming supplies, though, and out of an organization. Based on the above definition it can be concluded that inventory management is concerned with decisions about how much quantity of goods to be ordered (how much to order) and when reservations will be made (when to order). The pressure of inventory management is that there is a reduction in inventory while maintaining customer service and production levels. There are two objectives for the inventory management system; to provide the level of customer service, and to minimize the cost of providing the service. Based on some opinions above, it can be concluded that the purpose of inventory management is to provide good service to customers (customers) with a minimum total cost. Some definitions of existing inventory management terms are as follows: ordering cost, setup cost, capital cost, and stock out cost.



Figure 1. Graph of Delivery of NSR materials to Drilling Site 2014-2016
(Source: Internal Data Collection)

2.1. Economic Order Quantity (EOQ)

Economic Order Quantity (EOQ) is an inventory system by providing a quantity of inventory material in a single purchase period with the least inventory cost. EOQ methods can be used for both purchased and self-produced goods. EOQ is widely used today because it is easy to use, however, one should pay attention to the assumptions used when applying it. The basic assumptions for using EOQ methods are as follows: (1) Demand can be determined with certainty and constancy so that the cost of stock out and associated with its capacity does not exist. (2) Items ordered independently with other items. (3) Booking is received promptly and surely. (4) The price of the item is constant [11-12].

The usual formula used to calculate the EOQ is as follows [3,10]:

$$EOQ = \sqrt{\frac{2DS}{H}} \quad (1)$$

$$T = \frac{EOQ}{D} \quad (2)$$

$$\text{Holding Cost} = H \frac{EOQ}{2} \quad (3)$$

The Economic Order Quantity (EOQ) method is used to determine how much ordering is economical for each order with the predetermined order frequency as well as when the order is re-done. EOQ can answer the questions about the conditions that often occur in the company, which determines the amount of inventory in accordance with the needs of the company that is not too high nor too low as to reduce losses that occur in the company due to improper company processing inventory [17].

2.2. Newsvendor Model

The Model Newsvendor or Model Newsboy is a stochastic model that considers the uncertainty factor in the number of requests per production period. The Newsboy model is a model developed by Federgruen [8] where the mean is a profit whereas deviations from averages (variance) are made at risk. Generally, the Newsboy Model has a production period that is not too long, because the goods produced have a time limit that is not too long (short live). Although that the expiration of goods can be observed, the age of goods can also be seen from the sale of goods. If the goods concerned can be sold at normal prices, then the goods are still within the time limit (age of goods has not been exhausted) [8]. The basic purpose of the Newsboy model is to determine the most reasonable amount of production that provides the maximum profit and predicts the magnitude of risk or deviation from the profit to be obtained [18].

In a stochastic production model, any product that exceeds demand will result in the cost of overstock cost of C_o and any goods in production that are less than the need will cause the cost of the lack of goods (understock cost) C_u . When s the sale price of goods per item, c purchasing goods per item and v residual value of unsold inventory. In the Newsboy model it is assumed that $v < c < s$. The calculation of excess goods (C_o) can be calculated using the following formula:

$$C_o = c - v \quad (4)$$

Calculation of shortage of goods (C_u) can be calculated using the following formula:

$$C_u = s - c \quad (5)$$

So we get the equation to calculate the critical ratio. Since the C_o and C_u values are positive, the critical ratio is in the range of 0 to 1. This equation applies to continuous demand distribution and always solves the problem.

$$F(Q^*) = \frac{C_u}{(C_o + C_u)} \quad (6)$$

The equation $F(Q^*)$ is defined as the probability that the demand will not exceed the supply Q^* . Critical ratios are defined as the probability of satisfaction over all requests over the period if unit Q^* is provided at the beginning of the period. It should be noted and understood that this is not the same as the proportion to demand fulfilment. When the cost of shortages and excess inventory is the same, the critical ratio value is half. If on the issue where Q^* is the median (middle value) of the demand distribution. When a symmetric demand density (such as normal density), the mean and middle values are equal.

$$Q = \sigma z + \mu \quad (7)$$

$$\text{Dengan } \sigma = \sqrt{\frac{\sum_{i=1}^n x_i^2 - (\sum_{i=1}^n x_i)^2}{n}} \quad (8)$$

2.3. Lot-Sized Reorder Point System

Reorder point is the point where the order must be held again in such a way that the arrival or acceptance of goods ordered is right when needed. This re-ordering needs to be done by the company at each period to prevent the occurrence of shortage of goods, so that company activity is not disturbed. Reorder Point is also defined as the time reorder of goods that will be required. Reorder point of each item of goods need to be known for the availability of goods is guaranteed, so ordering goods done at the right time when the stock of goods is not excessive and not empty. The calculation of reorder point is determined by the length of lead time, the average use of goods and safety stock [13-14].

Reorder point system model occurs when the amount of inventory contained in the stock decreases steadily, so we must determine how much the minimum level of inventory should be considered to re-order so that there is no shortage of inventory. The expected amount is calculated during the grace period, may also be added to the safety stock which usually refers to the probability or likelihood of stock shortages during the grace period. Here is an overview of reorder point and lead time [16]. Reorder point is also defined as a system that uses the inventory level to trigger a reordering of the inventory. In this case, the company must establish the minimum quantity of goods that must be available in the warehouse, so that when the inventory reaches the minimum, the goods must be reordered. This system is usually calculated as a forecast of goods demand during the lead time plus safety stock. In the EOQ (Economic Order Quantity) model, it is assumed that there is no time lag between ordering and procurement of materials. Therefore, the ordering point for inventory replenishment occurs at a prescribed minimum

level. When the inventory level drops to zero and due to an instant delivery by the supplier, the inventory level will return. Sometimes the rate of re-ordering is greater than the maximum inventory, this is due to the lead time that is too long or due to the uncertain levels of demand and lead time [3,15].

Furthermore, by defining $G(Q, R)$ as an estimate of the average annual cost for storage, setup, and lack of inventory. The combination of these costs into equations.

$$G(Q, R) = h(Q/2 + R - \lambda\tau) + K\lambda/Q + p\lambda n(R)/Q \quad (9)$$

The goal is to determine Q and R to minimize $G(Q, R)$. The most reasonable results can be found by equations.

$$Q_1 = \sqrt{\frac{2\lambda[K + pn(R)]}{h}} \quad (10)$$

$$1 - F(R) = Q_0 h / p\lambda \quad (11)$$

$$R = \sigma z + \mu \quad (12)$$

$$s = R - \mu \quad (13)$$

2.4. Service Level in (Q, R) Systems

This system helps management to determine the amount of costs due to out of inventory. On various issues, stock out costs include intangible components such as loss of product value and potential delays in other systems on the system. A common replacement for the term stock out cost is service level. Although there are many different meanings of the word service, it is generally interpreted as the probability of achieving customer satisfaction. Level services can be applied to both periodic review systems (Q, R). There are two service level types, Type 1 Service and Type 2 Service.

In the case of type 1 service, specifically to calculate the probability level against the absence of stock out cost at lead time. The α symbol is used to indicate the probability level. As the specification of the probability is determined from the value of R , the calculation of the R and Q values can be separated. The calculation of the most reasonable value (Q, R) aimed at the type 1 service is very easy.

- Calculate the value of R with the equation $F(R) = \alpha$.
- Value of $Q = EOQ$ (Economic Order Quantity).

On the Type 2 service, measure the proportion of the demand specified from the inventory. The β symbol is used to indicate the proportion of this type. The value of $n(R)/Q$ is the average fraction of the demand for the stock out cost in the cycle. Therefore, the value of β can be searched by the equation $n(R)/Q = 1 - \beta$. This equation is very complex compared to type 1, because it includes both Q and R values. This proves that EOQ is not lean in this case, only usually gives a pretty good result. If EOQ is used as a lot size, then its value can be calculated by the equation $n(R) = EOQ(1 - \beta)$ [3,22].

3. Result

As explained in the methodology, this study will present a comparison of 5 different inventory strategies for NSR materials, by comparing the most reasonable amount of inventory, material ordering time and the most reasonable inventory cost of the five strategies. The five

strategies are the Traditional Inventory Strategy that the company is currently implementing, EOQ (Economic Order Quantity), Newsvendor Model, Lot-Sized Reorder Point System, and Q and R Service Level System. Table 1 is a summary of the average number of inventories, planning and actual use of NSR materials.

Table 1. Summary of the average number of inventories, planning and actual use of NSR materials

No	Description	Amount
1	Average NSR Material Storage	39,50
2	Average NSR Material Use Planning	2,67
3	Average NSR Material Usage	2,33

Source: Company Data Processed

3.1. Economic Order Quantity (EOQ)

With EOQ strategy, to calculate the most reasonable order quantity of materials, equation (1) can be used, in this paper based on data from internal company, the number of materials needs NSR 2017 is as many as 32 units. The cost of ordering each order is USD 10,000 and material deposit per unit is USD 1,000.

$$EOQ = \sqrt{\frac{2DS}{H}} \quad (1)$$

$$EOQ = \sqrt{\frac{2 \times \text{annual needs} \times \text{ordering cost per order}}{\text{storage cost per unit}}}$$

$$EOQ = \sqrt{\frac{2 \times 32 \times 10,000}{1,000}}$$

$$EOQ = \sqrt{640} = 25.3 \approx 25 \text{ unit}$$

Furthermore, the most reasonable time to place an order can be calculated by the equation (2).

$$T = \frac{EOQ}{D} \quad (2)$$

$$T = \frac{25}{32}$$

$$T = 0.78 \text{ year} = 9.375 \text{ months} \approx 9 \text{ months}$$

Then can be calculated holding cost per order period with equation (3):

$$\text{Holding Cost} = H \frac{EOQ}{2} \quad (3)$$

$$\text{Holding Cost} = 1,000 \frac{25}{2}$$

$$\text{Holding Cost} = \text{USD } 12,500$$

$$\text{Holding Cost} = \text{USD } 1,388 \text{ per month}$$

3.2. Newsvendor Model

With the Newsvendor Model, to calculate the most reasonable order quantity of materials, equations (4-8) can be used. In this case, based on data obtained from the internal company for the number of annual needs 2017 is

32 units. With a production cost of USD 20,000 and a product selling price of USD 40,000 and the remaining selling price of USD 10,000.

First calculate the cost of excess inventory (Co) and the cost of inventory shortage (Cu) by using equations (4-5).

$$Co = c - v \tag{4}$$

Co = Cost of Production – Remaining Selling Price

$$Co = USD 20,000 - USD 10,000 = USD 10,000$$

$$Cu = s - c \tag{5}$$

Cu = Product Selling Price – Cost of Production

$$Cu = USD 4,0000 - USD 2,000 = USD 2,000$$

Next calculate the critical ratio with equation (6).

$$F(Q^*) = \frac{Cu}{(Co+Cu)}$$

$$(6)F(Q^*) = \frac{USD 20,000}{USD (20,000+10,000)}$$

$$F(Q^*) = \frac{USD 20,000}{USD 30,000}$$

$$F(Q^*) = 0.667$$

By using table z, we get z value for 0.667 is 0.42. So that the most reasonable number of orders for one period of material ordering can be calculated by equation (7). By calculating the standard deviation (σ) first using equation (8).

$$\sigma = \sqrt{\frac{\sum_{i=1}^n x_i^2 - (\sum_{i=1}^n x_i)^2}{n}} \tag{8}$$

$$\sigma = \sqrt{\frac{(12)(100) - 1024}{(12)(11)}}$$

$$\sigma = \sqrt{1.33} = 1.15$$

$$Q = \sigma z + \mu \tag{7}$$

$$Q = (\text{Standard Deviation} \times z \text{ Value}) + (\text{Mean})$$

$$Q = (1.15) (0.42) + (2.67) = 3.153 \text{ Unit} \approx 3 \text{ Unit per Month}$$

Table 2. Number and Time of Order and Material Storage Costs by Using EOQ Inventory Strategy

No	Product Code	Material	Month	Number of Needs (unit)	Number of Order	Average of Storage Cost (USD)
1	RA 01US	NSR	Jan-17	1		1,388
2	RA 01US	NSR	Feb-17	3		1,388
3	RA 01US	NSR	Mar-17	3		1,388
4	RA 01US	NSR	Apr-17	3		1,388
5	RA 01US	NSR	May-17	2		1,388
6	RA 01US	NSR	Jun-17	2	25 Unit	1,388
7	RA 01US	NSR	Jul-17	3	for 9 Month	1,388
8	RA 01US	NSR	Aug-17	4		1,388
9	RA 01US	NSR	Sep-17	2		1,388
10	RA 01US	NSR	Oct-17	1		1,388
11	RA 01US	NSR	Nov-17	3		1,388
12	RA 01US	NSR	Dec-17	5		1,388
Total				32		16,666

Source: Company Inventory Data 2017 Processed

Table 3. Quantity, Order Time and Material Storage Cost by Using News vendor Model

Material	Month	Number of Needs (unit) (x)	(x ²)	Mean (μ)	Number of Monthly Storage (unit)	Average of Storage Cost (USD)
NSR	Jan-17	1	1		3,00	4,166
NSR	Feb-17	3	9		3,00	4,166
NSR	Mar-17	3	9		3,00	4,166
NSR	Apr-17	3	9		3,00	4,166
NSR	May-17	2	4		3,00	4,166
NSR	Jun-17	2	4		3,00	4,166
NSR	Jul-17	3	9		3,00	4,166
NSR	Aug-17	4	16	2,67	3,00	4,166
NSR	Sep-17	2	4		3,00	4,166
NSR	Oct-17	1	1		3,00	4,166
NSR	Nov-17	3	9		3,00	4,166
NSR	Dec-17	5	25		3,00	4,166
Total		32	100		36	49,999

Source: Company Inventory Data 2017 Processed

3.3. Lot-Sized Reorder Point System

To determine the Lot Size Reorder Point System, first we need to know the value of EOQ by using equation (1). With EOQ strategy, to calculate the most reasonable order quantity of materials can use Equation (1), in this paper based on data from internal company, the number of materials needs NSR 2017 is as many as 32 units. The cost of ordering each order is USD 10,000 and material deposit per unit is USD 1,000.

$$EOQ = \sqrt{\frac{2DS}{H}} \quad (1)$$

$$EOQ = \sqrt{\frac{2 \times \text{annual needs} \times \text{ordering cost per order}}{\text{storage cost per unit}}}$$

$$EOQ = \sqrt{\frac{2 \times 32 \times 10,000}{1,000}}$$

$$EOQ = \sqrt{640} = 25.3 \approx 25 \text{ unit}$$

Next use equation (11) to calculate the loss function, with the cost of the order shortage of USD 6,500.

$$1 - F(R) = Q_0 h / p \lambda \quad (11)$$

$$1 - F(R) = \left(\frac{25 \times 10,000.000}{100,000.000 \times 32} \right)$$

$$1 - F(R) = \left(\frac{25}{320} \right)$$

$$1 - F(R) = 0,078$$

Using table z. Substitute 0.078 so that z is 1.42 and the value of L(z) is 0.036. After both values are obtained, the value of R can be calculated.

$$R = \sigma z + \mu \quad (12)$$

$$R = (1,15)(1,41) + 2,67$$

$$R = 4,29$$

$$n(R) = \sigma L(z) = (1,15)(0,036) = 0,0414$$

Using equation (10), to calculate the lot size of Q1 in a single order.

$$Q_1 = \sqrt{\frac{2\lambda [K + pn(R)]}{h}} \quad (10)$$

$$Q_1 = \sqrt{\frac{(2)(32) [10,000 + (10,000)(0,0414)]}{1,000}}$$

$$Q_1 = \sqrt{666.496}$$

$$Q_1 = 25.816 \text{ unit} \approx 26 \text{ unit}$$

Then, calculate safety stock:

$$s = R - \mu \quad (13)$$

$$s = 4.29 - 2.67$$

$$s = 1.62 \approx 2 \text{ unit}$$

3.4. Service Level in (Q, R) Systems

To apply Service Level in (Q, R) Systems, first we must know the value of EOQ by using equation (1). In this study based on data from internal company, the total requirement of NSR material in 2017 is 32 units. The cost of ordering each order is USD 3,500 and the material deposit per unit is USD 680.

$$Q_1 = \sqrt{\frac{2\lambda [K + pn(R)]}{h}} \quad (10)$$

$$Q_1 = \sqrt{\frac{(2)(32) [10,000 + (10,000)(0,0414)]}{1,000}}$$

$$Q_1 = \sqrt{666.496}$$

$$Q_1 = 25.816 \text{ unit} \approx 26 \text{ unit}$$

Furthermore, the most reasonable time for ordering can be calculated by equation (2).

$$T = \frac{EOQ}{D} \quad (2)$$

$$T = \frac{25}{32} = 0,78 \text{ year} = 9,375 \text{ months} \approx 9 \text{ months}$$

Next look for the values of z and R, using equation (11).

$$1 - F(R) = Q_0 h / p \lambda \quad (11)$$

$$F(R) = 1 - \frac{Q_0 h}{p \lambda}$$

$$F(R) = 1 - \frac{(25)(1,000)}{(10,000)(32)}$$

$$F(R) = 1 - \frac{25}{320}$$

$$F(R) = 1 - 0.078$$

$$F(R) = 0.922$$

$$R = \sigma z + \mu \quad (12)$$

$$R = (1.15)(1.41) + 2.67$$

$$R = 4.29$$

Furthermore, calculate the safety stock and the most reasonable time for ordering can be calculated by equation (2).

$$s = R - \mu \quad (13)$$

$$s = 4.29 - 2.67$$

$$s = 1.62 \approx 2 \text{ unit}$$

Next calculate the storage cost in the following equation:

$$\text{Holding Cost} = H \frac{Q_0}{2} + s \quad (3)$$

$$\text{Holding Cost} = 1,000 \left(\frac{25}{2} + 2 \right)$$

$$\text{Holding Cost} = \text{USD } 14,500$$

$$\text{Holding Cost} = \text{USD } 1,611 \text{ per month}$$

Furthermore, the most reasonable time for ordering can be calculated by equation (2).

$$T = \frac{Q_1 + s}{H} \quad (2)$$

$$T = \frac{26}{32}$$

$$T = 0.8125 \text{ years} = 9.75 \text{ months} \approx 10 \text{ months}$$

Using the Q₂R level service, assuming the probability that all requests are met in one cycle is 90%, then:

$$Q_2 = Q_1 + s = 28 \text{ unit}$$

α = 0.9 using the attachment table 1 obtained the value of z = 1.28, so

$$R = \sigma z + \mu \quad (12)$$

$$R = (1.15)(1.28) + 2.67$$

$$R = 4.142 \approx 4$$

If the probability assumption is increased to 96%, then:

$$Q_2 = Q_1 + s = 28 \text{ unit}$$

α = 0.96 using the attachment table 1 obtained the value of z = 1.76, so

$$R = \sigma z + \mu \quad (12)$$

$$R = (1.15)(1.76) + 2.67$$

$$R = 4.67 \approx 5$$

After analysing the calculation of the amount of expenses charged to the company for the storage of NSR

materials, the analysis is done by comparing the five inventory strategies, including the Traditional System used by the company today, Economic Order Quantity (EOQ), Newsvendor Model, Lot Size Reorder Point System and Service Level in (Q, R) Systems. The five inventory strategies have proposed the most reasonable inventory amount and the most reasonable ordering time as well. Furthermore, the results of analysis and calculation are summarized in Table 5.

4. Discussion

The purpose of this study is to analyse the inventory strategy that is currently being implemented by oil and gas service companies in Cikarang which are considered to be the most reasonable or even become a source of waste in the company. Then a literature study of various inventory strategies has the potential to be a proposed as a new and more reasonable inventory strategy, the most reasonable inventory strategy is an inventory strategy with high availability but low inventory cost.

After analysing and studying some inventory strategies, this research creates a new proposal inventory strategy. This research will also calculate the most reasonable inventory level to reduce waste for NSR material at oil and gas services company in Cikarang. In addition to considering the advantages and disadvantages of each new inventory strategy proposal, the inventory cost factor is

also a determinant factor in choosing the most reasonable inventory strategy at the lowest possible cost.

4.1. Traditional Inventory

Currently the inventory model that companies apply is a traditional inventory model with a high inventory level. As an initial reference and comparison with other inventory proposals. This research will calculate the amount of inventory costs at the beginning that the company spent on applying this inventory model.



Figure 2. Graph of Inventory Costs with Traditional Inventory Model
(Source: Company Data Processed)

Table 4. Quantity, Order Time and Material Storage Cost by Using Lot-Sized Reorder Point System

No	Product Code	Material	Month	Number of Needs (unit)	Number of Order	Average of Storage Cost (USD)
1	RA 01US	NSR	Jan-17	1		1,500
2	RA 01US	NSR	Feb-17	3		1,500
3	RA 01US	NSR	Mar-17	3		1,500
4	RA 01US	NSR	Apr-17	3		1,500
5	RA 01US	NSR	May-17	2		1,500
6	RA 01US	NSR	Jun-17	2	28 Unit per 10 Months	1,500
7	RA 01US	NSR	Jul-17	3		1,500
8	RA 01US	NSR	Aug-17	4		1,500
9	RA 01US	NSR	Sep-17	2		1,500
10	RA 01US	NSR	Oct-17	1		1,500
11	RA 01US	NSR	Nov-17	3		1,500
12	RA 01US	NSR	Dec-17	5		1,500
Total				32		18,000

Source: Company Inventory Data 2017 Processed

Table 5. Summary of Analysis of Each Inventory Strategy

No	Inventory Strategy	Average Number of NSR Material Order (Unit)	Average Monthly NSR Material Storage Cost (USD)	Total NSR Material Annual Storage Cost (USD)
1	Traditional	71 per 12 Month	65,500	786,000
2	EOQ	25 per 9 Month	1,388	16,666
3	Model Newsvendor	3 per 1 Month	4,166	49,999
4	Lot Size Reorder Point System	28 per 10 Month	1,500	18,000
5	Service Level in (Q, R) System	28 per 11 Month	1,363	15,000

Source: Company Inventory Data 2017 Processed

4.2. Newsvendor Model

After studying inventory strategy using Newsboy or Newsboy Model it can be concluded that the most reasonable amount of NSR material inventory in 2017 is 36 units for 12 months usage. With each inventory amount each month is 3 units. The company is expected to make regular orders every month to ensure all requests in 2017 can be met. By applying the Newsvendor Model as a new inventory strategy, the company is expected to reduce the amount of high inventory as applied to its inventory system before it. In the previous section, paper already compares the inventory cost difference between the traditional inventory strategy that the company applies today to the proposed inventory strategy using the Newsvendor Model.

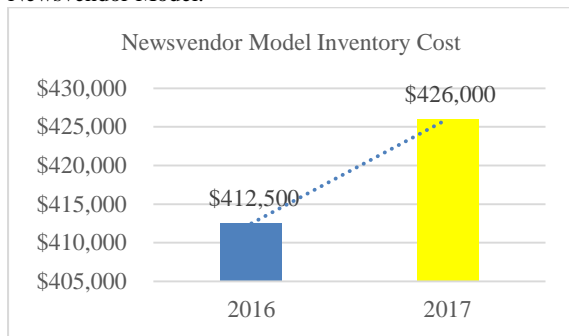


Figure 4. Graph of Inventory Costs with Newsvendor Model (Source: Company Data Processed)

By using an inventory system with the Newsvendor Model, the company is expected to reduce the amount of funds spent on NSR material inventory capital. Previously with the traditional system the company will issue funds amounting to USD 412,500 in 2017 but otherwise, if the company implements the Newsvendor Model the company will instead spend more funds for a larger inventory capital of USD 426,000. This is because the company is required to make regular reservations every month. Of course, the shipping costs will increase drastically. Instead, the company will raise USD 13,500 or 3.27% from its previous budget if it wants to implement the Newsvendor Model. Increased capital cost of material inventory can be seen clearly in Figure 4.

4.3. Lot Size Reorder Point System

After studying inventory strategy by using Lot Size Reorder Point System, it can be concluded that the most reasonable amount of NSR material inventory in 2017 is as much as 26 main units and added 2 units as safety stock so total 28 units for 10 months usage. By applying the Lot Size Reorder Point System as a new inventory strategy, the company is expected to reduce the amount of high inventory as applied to its inventory system before it. The comparison of inventory cost between the traditional inventory strategy that the company is currently implementing with the proposed inventory strategy by using the Lot Size Reorder Point System.

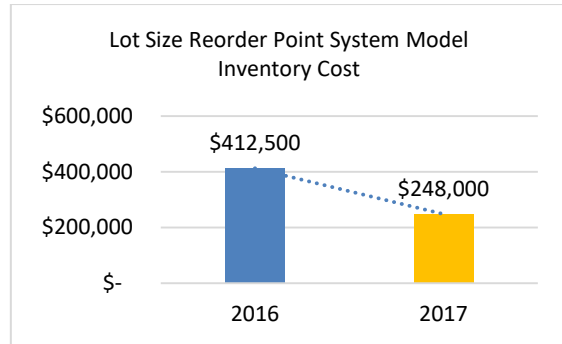


Figure 5. Graph of Inventory Costs with Lot Size Reorder Point System Model (Source: Company Data Processed)

By applying the Lot Size Reorder Point System as a new inventory strategy, the company can reduce the amount of funds spent on NSR's material inventory capital. Previously with the traditional system the company will spend USD 412,500 in 2017 for NSR material inventory capital, but by applying Lot Size Reorder Point System, the company only has to spend the fund for inventory capital of USD 248,000 for 10 months. The Company can directly save up to USD 164,500 or 39.88% of the previous budget. The decrease in capital cost of material inventory can be seen clearly in Figure 5.

4.4. Service Level in (Q, R) Systems

After studying inventory strategy using Service Level in (Q, R) Systems, it can be concluded that the most reasonable amount of NSR material inventory in 2017 is 28 main units and 2 units added as safety stock so total 28 units. The calculation of the inventory amount is used in the same way as the Lot Size Reorder Point System, but the difference lies in when the company will reorder material inventory. By implementing Service Level in (Q, R) Systems, the most reasonable time to place an order is when the material inventory in the warehouse is 4 units. By implementing Service Level in (Q, R) Systems as a new inventory strategy, the company is expected to reduce the high inventory amount as applied to its inventory system before. As previously described, the proportion of inventory cost between the traditional inventory strategy that the company applies today to the proposed inventory strategy by using Service Level in (Q, R) Systems.

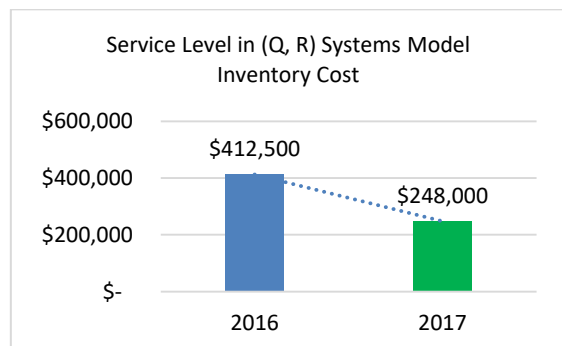


Figure 6. Graph of Inventory Costs with Service Level in (Q, R) Systems Model (Source: Company Data Processed)

By implementing Service Level in (Q, R) Systems as a new inventory strategy, the company can reduce the amount of funds spent on NSR material inventory capital. Previously with the traditional system, the company will spend USD 412,500 in 2017 for NSR material inventory capital, but by applying Lot Size Reorder Point System, the company only has to spend the fund for inventory capital of USD 248,000 for 11 months. Companies can directly save funds amounting to USD 164,500 or 39.88% of the previous budget. Decrease in capital cost of material inventory can be seen clearly in Figure 6.

4.5. Selection of Proposed Inventory Strategies

Based on the findings given, and the advantages and disadvantages proposed by each inventory model and completed with the calculation by using several inventory models such as Traditional Model, Economic Order Quantity (EOQ), Newsvendor Model, Lot Size Reorder Point System and Service Level in (Q, R) Systems, it is clearly shown that the results of the analysis and calculation will be the cornerstone of the selection of the most reasonable inventory strategy where we have high levels of availability and low inventory costs.

Table 6 describes the total inventory cost of each inventory model used in this study. Overall the proposed inventory model tends to be better than the inventory strategy that companies apply today. However, the most appropriate inventory strategy proposal based on the research results is the Service Level in (Q, R) Systems model. Because this inventory mode perfects the previous inventory models of Economic Order Quantity (EOQ) and Lot Size Reorder Point System.

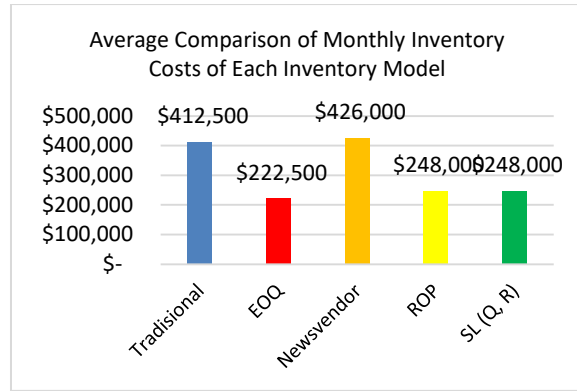


Figure 7. Average Monthly Inventory Cost (Source: Company Data Processed)

Conclusion

From the results of research and discussion conducted, it can be concluded as follows. Based on the results of this study, the company is advised to apply the inventory model proposal with Service Level in (Q, R) Systems. Because this inventory model is the most reasonable model to solve the inventory problem at oil and gas service company in Cikarang. This inventory model can determine the most reasonable amount of inventory for company needs in the year 2017 that is as much as 26 units and added 2 units as safety stock so that it can save inventory cost equal to 30.50% every month. The reorder point is also determined based on the remaining inventory amount, which is 4 units. Also, by applying this method based on analysis and calculation from literature, the company can meet all customer demands with a probability of success rate more than 70%.

Table 6. Total Inventory Cost of Each Inventory Model

No	Inventory Model	Capital Cost (USD)	Ordering Cost (USD)	Storage Cost (USD)	Lifetime Storage (Month)	Total Annual Storage Cost (USD)	Average Monthly Cost (USD)
1	Traditional	340.000	20.000	52.500	12	412.500	34.375
2	EOQ	212.500	10.000	12.500	9	235.000	26.111
3	Newsvendor	306.000	120.000	50.000	12	476.000	39.667
4	ROP	238.000	10.000	15.000	10	263.000	26.300
5	SL (Q, R)	238.000	10.000	15.000	11	263.000	23.909

(Source: Company Data Processed)

Acknowledgements

This research was supported by our colleagues which is Mercu Buana University who provided insight and expertise that greatly assisted the research, although they may not agree with all of the interpretations/conclusions of this paper. Also, thanks for assistance with particular technique, methodology and for comments that greatly improved the manuscript. We would also like to show our gratitude for sharing their pearls of wisdom with us during course of this research, and we are also immensely grateful for their comments on an earlier version of the manuscript, although any errors are our own and should not tarnish the reputations of these esteemed colleagues.

References

- [1] Pike, Bill. (2002). Well – Logging. Oil & Gas Investor, 22, 9; ProQuest pg. 64.
- [2] Rahani, A. R., & Al-Ashraf, M. (2012). Production flow analysis through value stream mapping: a lean manufacturing process case study. Procedia Engineering, 41, 1727-1734. Chicago.
- [3] Nahmias, S., & Olsen, T. L. (2015). Production and operations analysis. Waveland Press.
- [4] Anonymous. (2006). Downhole Data Captured. Oil & Gas Investor, 22, 9; ProQuest pg. 16.
- [5] Hansen, Don R. and Maryanne M. Mowen. 2001. Cost Management: Accounting and Control. Second Edition. USA: South-Western College Publishing.
- [6] Khan, M., Jaber, M. Y., & Bonney, M. (2011). An economic order quantity (EOQ) for items with imperfect quality and inspection errors. International Journal of Production Economics, 133(1), 113-118.
- [7] Jaggi, C. K., Goel, S. K., & Mittal, M. (2011). Economic order quantity model for deteriorating items with imperfect quality and permissible delay on payment. International Journal of Industrial Engineering Computations, 2(2), 237-248.
- [8] Federgruen, Chen (2002). Mean-Variance Analysis, New York.
- [9] Ben-Daya, M., & Hariga, M. (2004). Integrated single vendor single buyer model with stochastic demand and variable lead time. International Journal of Production Economics, 92(1), 75-80.
- [10] Kogan, K., & Lou, S. (2003). Multi-stage newsboy problem: A dynamic model. European Journal of Operational Research, 149(2), 448-458.
- [11] Ferguson, M., Jayaraman, V., & Souza, G. C. (2007). Note: An application of the EOQ model with nonlinear holding cost to inventory management of perishables. European Journal of Operational Research, 180(1), 485-490.
- [12] Wahab, M. I. M., Mamun, S. M. H., & Ongkunaruk, P. (2011). EOQ models for a coordinated two-level international supply chain considering imperfect items and environmental impact. International Journal of Production Economics, 134(1), 151-158.
- [13] Li, J., Cheng, T. E., & Wang, S. (2007). Analysis of postponement strategy for perishable items by EOQ-based models. International Journal of Production Economics, 107(1), 31-38.
- [14] Huang, Wei., Swaminathan, Jayashankar M. (2009). "Introduction of a Second Channel: Implications for Pricing and Profits". ELSEVIER, European Journal of Operational Research No. 194, 258–279.
- [15] Stevenson, W. J., & Hojati, M. (2007). Operations management (Vol. 8). Boston: McGraw-Hill/Irwin.
- [16] Rondeau, P. J., & Litteral, L. A. (2003). Evolution of manufacturing planning and control systems: from reorder point to enterprise resource planning. Production and Inventory Management Journal, 42(2), 1.
- [17] Shukla, H., Shukla, V., & Yadava, S. (2013). EOQ model for deteriorating items with exponential demand rate and shortages. Uncertain Supply Chain Management, 1(2), 67-76.
- [18] Kocabiyikoglu, A., & Popescu, I. (2011). An elasticity approach to the newsvendor with price-sensitive demand. Operations research, 59(2), 301-312.
- [19] Sarac, A., Absi, N., & Dauzère-Pères, S. (2010). A literature review on the impact of RFID technologies on supply chain management. International Journal of Production Economics, 128(1), 77-95.
- [20] Manna, S. K., & Chaudhuri, K. S. (2006). An EOQ model with ramp type demand rate, time dependent deterioration rate, unit production cost and shortages. European Journal of Operational Research, 171(2), 557-566.
- [21] Huang, Y. F., & Hsu, K. H. (2008). An EOQ model under retailer partial trade credit policy in supply chain. International Journal of Production Economics, 112(2), 655-664.
- [22] Soni, H. (2011). (Q, R) inventory model with service level constraint and variable lead time in fuzzy-stochastic environment. International Journal of Industrial Engineering Computations, 2(4), 901-912.
- [23] Rao, V. D. P., Subbaiah, K. V., & Raju, V. R. (2009). Fuzzy genetic approach to economic lot-size scheduling problem. JJMIE, 3(1), 9-16.
- [24] Shakoor, M., Jadayil, W. A., Jabera, N., & Jaber, S. (2017). Efficiency Assessment in Emergency Department Using Lean Thinking Approach. Jordan Journal of Mechanical & Industrial Engineering, 11(2).
- [25] Prasad Patnaik, V. V. S., & Patnaik, D. P. (2015). A Numerical Study on Deterministic Inventory Model for Deteriorating Items with Selling Price Dependent Demand and Variable Cycle Length. Jordan Journal of Mechanical & Industrial Engineering, 9(3).

Solar Panel Cooling and Water Heating with an Economical Model Using Thermosyphon

Laith Jaafer Habeeb^a, Dheya Ghanim Mutasher^a, Faez Abid Muslim Abd Ali^{b,*}

^a University of Technology, Mechanical Engineering Department

^b University of Kufa, Engineering College

Received 12 Jan. 2018

Abstract

In the present work, experimental and theoretical study has been carried out to investigate the effect of using heat thermosyphon on the performance of cooling photovoltaic thermal solar panel. Three test rigs are constructed. The first system (module I) constructed from photovoltaic panel with 0.07 mm thickness cooper plate base, four thermosyphon heat pipes and water box heat exchanger with a capacity of 16.2 litter. The second system (module II), which was made for a cheaper economic model than module I, comprises similar photovoltaic panel with 0.07 mm thickness aluminum plate base, six copper heat pipes with the same dimensions for (module I) and water cylindrical heat exchanger with a capacity of 9.537 litter. The novel panels compared with the traditional panel. The experiments are carried out in July 2017, Baghdad. A MATLAB program is used to compute the models and establishing characteristic curves. The experimental thermal results proved that the novel methods are successful in cooling the solar panel, the module I is colder than the module II and the two modules are cooler than the traditional panel in a rate of (15-35) % for module I and (10-14) % for module II. The experimental electrical results showed that the efficiency of module I is improved by (11-14) % and module II improved by (4-8) % compared with traditional one. The comparison between the experimental and theoretical results revealed a good agreement with a small deviation of about (3-6) %.

© 2018 Jordan Journal of Mechanical and Industrial Engineering. All rights reserved

Keywords: cooling photovoltaic panel, water heating, thermosyphon;

Nomenclature

A	Module area	θ	angle, degree
c	specific heat capacity, J/kg K	ρ	density, kg/m ³ , reflectance
D	diameter, m	σ	Stefan Boltzman constant, W/m ² K ⁴
E	output electricity, W/m ²	τ	Transmittance
G	solar radiation intensity, W/m ²	$(\tau\alpha)$	Transmittance absorptance product, -
h	heat transfer coefficient, W/m ² K	Subscripts	
k	thermal conductivity, W/m K	a	air, ambient
L	length, m	b	base panel
M	mass, kg	i	inner, differential node "i"
R	thermal resistance, K/W	j	differential node "j"
T	temperature, °C	l	Liquid
t	time, s	o	Outer
u	flow velocity, m/s	p	heat pipe
Ex	exergy, W/m ²	s	thermal insulating material
Pr	Prandtl number	v	Vapor
Nu	Nusselt number	w	water, wall of the heat pipe
Ra	Raleigh number	con	condenser section of heat pipe

Re	Reynolds number	eva	evaporator section of heat pipe
Greek letters			
α	Absorptivity	pv	PV cell
γ	PV cell covering factor	sky	Sky
δ	thickness, m	TPT	black tedlar-polyester-tellar
ε	emissivity, second-low efficiency,-		
η	Efficiency		

1. Introduction

Photovoltaic is the most useful way of employing solar energy by directly converting it into electricity. Energy conversion devices, which are used to convert sunlight to electricity using the photoelectric effect are called solar cells [1]. There are two distinguished types of energy that can be produced: electrical energy and thermal energy, it leads to increase the photovoltaic temperature. The overall efficiency of photovoltaic cells drops radically with an increase in temperature and the rate of decrease ranges from 0.25% to 0.5% per degree Celsius, depending on the cell material used [2]. Akbarzadeh and Wadowski [3] introduced a passive method based on thermosiphons

* Corresponding author e-mail: faezabdali22@gmail.com.

which can effectively cool the Photovoltaic cells under concentrated light. Incorporating a thermosiphon cooling system for the photovoltaic cells has been manufactured and successfully tested. Tonui et al. [4] studied the photovoltaic/thermal (PV/T) panel with heat extraction by forced or natural air circulation, prepare a non-expensive and simple method of photovoltaic panel cooling and the solar preheated air could be used in manufactured, industrial and agricultural section. The paper presents the use of a suspended thin flat metallic sheet at the middle or fins at the back wall of an air duct as heat transfer augmentations in an air-cooled photovoltaic/thermal (PV/T) solar collector to improve its overall performance. William et al. [5] wrote a research about used heat pipes to cool the concentrating photovoltaic systems, this work demonstrated the feasibility of a heat pipe cooling solution for concentrating photovoltaic cells. Heat pipes can be used to passively remove the heat, accepting a high heat flux at the concentrating photovoltaic cell, and rejecting the heat to fins by natural convection. Tang et al. [6] introduced a new method by using the micro heat pipe arrangement to cooling photovoltaic panel. The experimentally implemented study used air or water to cool the solar panel, the solar panel temperature can decrease and increase the photoelectric conversion efficiency. The temperature decreases by 4.7 °C and output power increases by 8.4%, for air-cooling compared with ordinary solar panel, and the temperature decreases by 8 °C and output power increases by 13.9 % for water-cooling. Mutombo [7] presented study about the behavior of thermosiphon hybrid photovoltaic thermal panel when exposed to differences of environmental parameters and to prove the advantage of cooling photovoltaic modules using a rectangular channel shape with water. The simulation results showed that the overall efficiency of the PV/T module was 38.7% against 14.6% for a standard PV module while the water temperature in the storage tank reached 37.1 °C. During summer in South Africa, this is a great reassurance to the marketing of the hybrid photovoltaic thermal technology.

This research introduces a novel technique to increase the conduction heat transfer by using a copper and aluminum plates to increase the thermal conduction surface area from the panel to the heat pipe. Thus, the present work is concerned with carrying out experimental study and mathematical verification to study the performance of photovoltaic panel by using heat pipe as a new technique to increase the conduction heat transfer by using a copper plate for module I and aluminum plate for module II to increase the thermal conduction surface area from the panel to the heat pipe. Also, the study is coupled with electrical and thermal model for calculating various parameters related to the performance of photovoltaic cooling by heat pipe system and through solving equations of the problem numerically for all parts and determining PV model parameters.

2. Heat Pipe Photovoltaic Modules HP-PV/T

There are three photovoltaic panels used in the experimental work (two modified solar module panels and a traditional panel to compare with), there were made of monocrystalline solar module 80(72) M1240×541. The specifications of photovoltaic panels are; peak power (Pmax) which is 80 (Watt), voltage at maximum power (Vmp) of 33.3 (V), current at maximum power (Imp) 2.4 (A), open circuit voltage (Voc) of 41.5 (V) and short circuit current (Isc) of 2.6 (A), these are provided by the manufacturer for the reference conditions of 1000 W/m² of irradiance level, 25 °C of cell temperature, total number of cells are 68. Figure (1) showed the experimental setup for modules (I and II), which has been designed and manufactured in this work.



Figure 1. Experimental setup system.

2.1. Module I

The test system consists of four copper thermosiphon heat pipe, 1200 mm evaporator length with filling ratio 55% distilled water as a working fluid, 14 mm inner diameter and 16 mm outer diameter, fixed on the back surface of the PV module. A copper plate of 0.07 mm thickness covered heat pipes and panel from the back, the new technique was done by envelope around the heat pipe to increase the contact surface, Fig. (2). 50 mm glass wool insulated the system from the back of the panel. 150 mm condenser length with 28 mm inner diameter and 30 mm outer diameter, immersed at (540×150×300) mm³ water box. The space between the two adjacent heat pipes were measured to be approximately 140 mm. Schematic diagram of the experimental rig with thermocouples location is shown in Fig. (3).



Figure 2. copper plate with heat pipe in the back of panel.

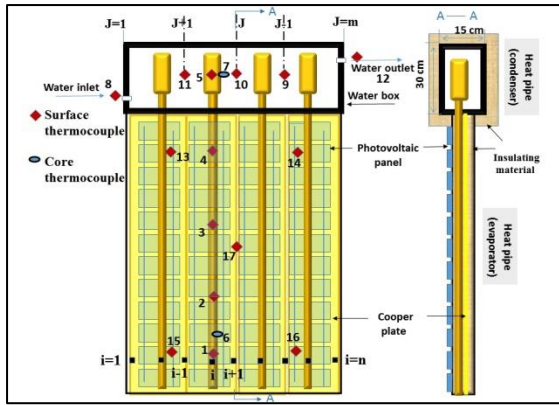


Figure 3. Schematic diagram of module (II) and thermocouples location.

2.2. Module II

The test system (I) is expensive (172 \$) because of the use of expensive parts that made from pure copper 90-95%. Therefore, a second low cost and economic (39 \$) test system (II) was used and placed next to system (I) to study the performance of systems and compare between them. This cheap and economic Photovoltaic module II was used for the first time which consists of six thermosyphon heat pipes with the same dimension in module I, aluminum plate instead of copper plate, heat exchanger is made of plastic cylindrical pipe of 3 mm thickness with 146 mm inner diameter and 540 mm length, water tank, storage tank and stand. Schematic diagram of the experimental rig with thermocouples location is shown in Fig. (4).

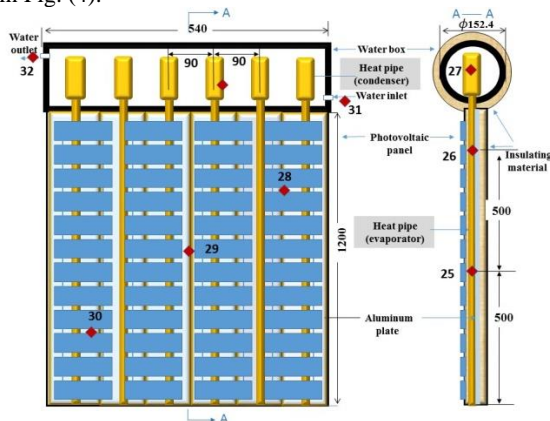


Figure 4. Schematic diagram of module (II) and thermocouples location.

The most previous studies tested the performance of the photovoltaic without a load, wherefore in this work, the performance of the photovoltaic with load is studied and, it showed the load effects on the photovoltaic behavior. Because PV panel produces electricity and warm water at the same time, the load will be a water electrical heater (DC 40 Watt) that receives the power from the PV panel. So, it can produce hot water instead of warm water to use it in the houses and industrial applications.

3. Thermal analyses

In the present study, a passive technique model was developed for an HP-PV/T system. The mathematical model consists of five main equation sets as follows [8]:

1. Heat-balance equation of the PV module.
2. Uni-dimensional heat conduction of the base panel (aluminum plate).
3. Heat-balance equation of the heat pipe.
4. Heat-balance equation for water in the heat exchanger.
5. Heat-balance equation for water in the storage tank.

The following assumptions were made in the model to simplify the calculation:

1. Heat conduction in the longitudinal direction of the aluminum plate was neglected.
2. The temperatures of the adhesive layer (EVA and TPT) and PV cells in the same direction were considered equal.
3. The heat capacity of the adhesive layer (EVA and TPT) was neglected.
4. Heat loss from the heat pipe condenser to the ambient was neglected.

Figure (7) depicts the section of the HP-PV/T solar collector.

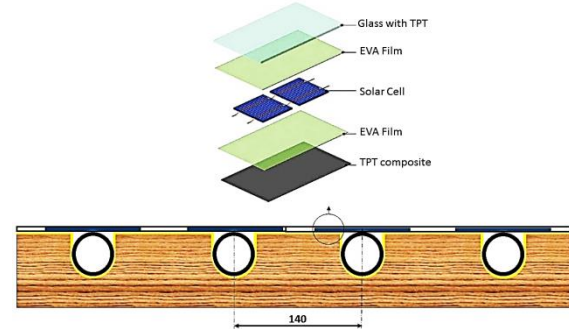


Figure 5. Section of the HP-PV/T solar collector.

Based on assumptions described above, for the photovoltaic layer, which includes the PV cells, EVA and TPT, the heat-balance equation is given by [8]:

$$\gamma \delta_{pv} \rho_{pv} C_{pv} \frac{\partial T_{pv}}{\partial t} = h_a (T_a - T_{pv}) + h_{sky,pv} (T_{sky} - T_{pv}) + (T_b - T_{pv}) / R_{b,pv} + G(\tau\alpha)_{pv} - E_{pv} \tag{1}$$

Where, h_a and $h_{sky,pv}$ are convective and radiant heat transfer coefficients, respectively, between the PV and surroundings.

T_{sky} is the sky temperature with:

$$T_{sky} \equiv T_a \tag{2}$$

$$h_a = 2.8 + 3.0u_a \tag{3}$$

$$h_{sky,pv} = \epsilon_{pv} \sigma (T_{sky}^2 + T_{pv}^2) (T_{sky} + T_{pv}) \tag{4}$$

$$\gamma \text{ is PV cell coverage ratio [9,10], and } \gamma = \frac{A_{pv}}{A_c} \tag{5}$$

Where, σ is the Stefan-Boltzmann constant ($5.6697 \times 10^{-8} \text{ W/m}^2 \text{ K}^4$) and $R_{b,pv}$ is the thermal resistance between the PV layer and base panel (copper plate) expressed as [9, 11]:

$$R_{b,pv} = \delta_{ad} / K_{ad} \tag{6}$$

E_{pv} is given by the instantaneous PV efficiency (η_{pv}) expressed as:

$$E_{pv} = G(\tau\alpha)_{pv}\tau_{ad}\eta_{ref}(1 - B_{ref}(T_{pv} - T_{ref})) \quad (7)$$

Where, η_{ref} is the reference cell efficiency at the reference operating temperature, $T_{ref} = 25$ °C.

B_{ref} is the temperature coefficient, $B_{ref} = 0.0045$ °C⁻¹.

τ_{ad} is the transmittance of the adhesive layer.

$(\tau\alpha)_{pv}$ is the effective absorptance and is given as:

$$(\tau\alpha)_{pv} = \frac{\tau\alpha}{1 - (1 - \alpha)\rho_d} \quad (8)$$

α is the effective absorptance of PV/T plate given as:

$$\alpha = \gamma\alpha_{pv} + (1 - \gamma)\alpha_{TP} \quad (9)$$

ρ_d is the reflectance of inner cover for diffuse radiation and is given as [9, 11 and 12]:

$$\rho_d = 1 - \alpha_{ad} - \tau_{ad} \quad (10)$$

The base panel divided the differential grid, as shown in Fig. (6). The two types of grid are labeled, where one grid is connected to a heat pipe node and the other is not (middle node). The heat-conduction equations in these two types of grid are different and are given by Eqs. (7) and (8), respectively [9, 11 and 12].

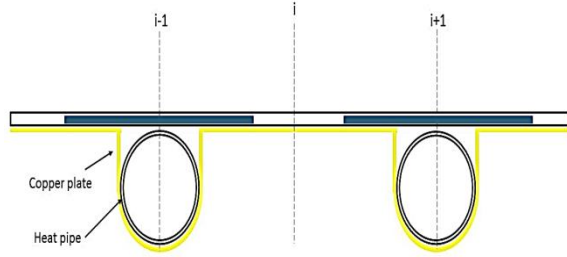


Figure 6. Differential grid partition of the base panel.

The expressed of heat-pipe node is:

$$\rho_b c_b \frac{\partial T_b}{\partial t} = k_b \frac{\partial^2 T_b}{\partial x^2} + \frac{1}{\delta_b} \left[(T_a - T_b)/R_{b,a} + (T_{pv} - T_b)/R_{b,pv} + (T_{p,eva} - T_b)/(R_{p,b}) \right] \quad (9)$$

$$\rho_b c_b \frac{\partial T_b}{\partial t} = k_b \frac{\partial^2 T_b}{\partial x^2} + \frac{1}{\delta_b} \left[\frac{(T_a - T_b)/R_{b,a}}{+ (T_{pv} - T_b)/R_{b,pv}} \right] \quad (10)$$

Were $R_{b,a}$ is the thermal resistance between the base panel and the ambient air, given by:

$$R_{b,a} = \delta_s/k_s + 1/h_a \quad (11)$$

Where, δ_{pb} and A_{pb} are the thickness between the base panel and evaporator section of heat pipe and contact area, respectively.

For the heat pipe, the heat-balance equations were provided for the evaporator and condenser sections, respectively. Heat transfer from the evaporator section to the condenser section was calculated using total thermal resistance $R_{eva,con}$.

Having known that the pressure decrease that is caused by vapor flow along the axial length of the heat pipe is

very small, the vapor space is assumed to operate at a constant saturation pressure. Therefore, the temperature gradient of the working fluid along the axial length of the heat pipe can be neglected.

The value for $R_{eva,con}$ can be derived based on the following parts:

- $R_{eva,p}$, thermal resistances across the thickness of the container wall and thickness.
- $R_{eva,wick}$, thermal resistance across the wick thickness.
- $R_{eva,i}$, thermal resistance that occurs at the vapour-liquid interfaces in the evaporator.
- $R_{con,i}$, thermal resistance associated with the condensing process.
- $R_{con,p}$, thermal resistance associated with the conduction process through the pipe wall.
- That's will be:

$$\sum R_{eva,con} = R_{eva,p} + R_{eva,wick} + R_{eva,i} + R_{con,i} + R_{con,p} \quad (12)$$

$$R_{eva,p} = \frac{\ln(d_o/d_i)}{2\pi k_p L_{eva}} \quad (13)$$

$$R_{eva,wick} = \frac{\ln(d_{o,wick}/d_{i,wick})}{2\pi k_{wick} L_{eva}} \quad (14)$$

$$R_{eva,i} = \frac{2}{h_{eva,i} \pi d_i L_{eva}} \quad (15)$$

$$h_{eva,i} = \frac{k_l}{t_{wick}}$$

k_l and t_{wick} , the thermal conductivity of the fluid and the wick thickness, respectively.

$$R_{con,p} = \frac{\ln(d_o/d_i)}{2\pi k_p L_{con}} \quad (16)$$

$$R_{con,i} = \frac{1}{h_{con,i} \pi d_i L_{con}} \quad (17)$$

Where $h_{con,i}$ is the condensing film coefficient that may be obtained from the Nusselt analysis for film wise condensation as [7 and 8]:

$$h_{con,i} = 1.13 \left[\frac{\phi \sin\theta \cdot \rho_l (\rho_l - \rho_v) k_l^3 h_{fg}}{\mu_l \Delta T_{cr} L_{con}} \right]^{1/4} \quad (18)$$

Because of using the wickless heat pipe, the $R_{eva,wick}$ and $R_{eva,i}$ were neglected.

Therefore, $\Sigma R_{eva,con}$ becomes:

$$\Sigma R_{eva,con} = R_{eva,p} + R_{con,i} + R_{con,p} \quad (19)$$

The heat-balance equation for the evaporator section, is expressed as:

$$M_{p,eva} c_p \frac{\partial T_{p,eva}}{\partial t} = (T_{p,con} - T_{p,eva})/R_{eva,con} + (T_b - T_{p,eva})/R_{p,b} \quad (20)$$

and for the condenser section as:

$$M_{p,con} c_p \frac{\partial T_{p,con}}{\partial t} = (T_{p,eva} - T_{p,con})/R_{eva,con} + A_w h_{w,con} (T_w - T_{p,con}) \quad (21)$$

$h_{w,con}$, is the convection heat transfer coefficient between the heat pipe condenser and water.

$$h_{w,con} = Nu \frac{k_w}{D_{con,o}} \quad (22)$$

$$Nu = CRe^m Pr^n \quad (23)$$

Values of C , m and n depend on the Reynold's number [7 and 13].

In the water box, the differential grid partition for water is shown in Fig. (7). In addition, the upwind scheme is used in the water differential equation, and for grid (j), the equation can be expressed as:

$$m_w c_w \frac{\partial T_{w,j}}{\partial t} + \dot{m}_w c_w (T_{w,j} - T_{w,j-1}) = (T_a - T_{w,j}) / R_{a,w} + A_w h_{w,con} (T_{p,con} - T_{w,j}) \quad (24)$$

Where, m_w is the mass of the water in a single control volume.

\dot{m}_w is the mass flow rate of the water, $\dot{m}_w = \rho_w u_w A$.

$R_{a,w}$ is the equivalent thermal resistance between water and ambient air.

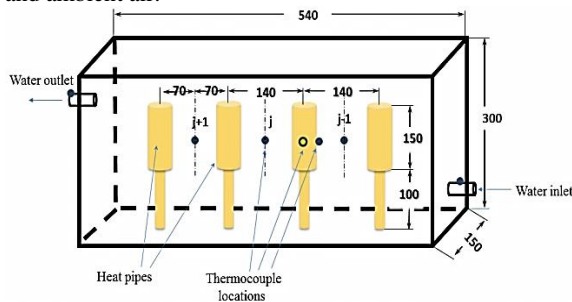


Figure 7. Differential grid partition of water in the water box.

The heat balance equation for the water in the storage tank is given by [8 and 11]:

$$M_{w,tank} c_w \frac{\partial T_{w,t}}{\partial t} = (T_a - T_{w,t}) / R_{a,wt} + n \cdot \dot{m}_w c_w (T_{w,out} - T_{w,in}) \quad (25)$$

Where, $M_{w,tank}$ is the mass of the water in the storage tank.

$R_{a,wt}$ is the equivalent thermal resistance between the water and the ambient air.

$T_{w,in}$ and $T_{w,out}$ are the inlet and outlet water temperatures, respectively, of solar collector.

n is the number of solar panel.

The instantaneous useful heat gain of the system is given by:

$$Q_w = M_w c_w (T_{w,out} - T_{w,in}) \quad (26)$$

The instantaneous useful heat gain of the system is expressed as

$$Q_w = M_{w,tank} c_w (T_{w,t}^1 - T_{w,t}^0) \quad (27)$$

The total efficiency of the HP-PV/T system can be described by an equation based on the first-law of thermodynamics (energy efficiency) and is introduced as follows [14]:

$$\eta_{pvt} = \frac{\text{Total thermal energy} + \text{total electrical energy}}{\text{Total radiation over the PV/T}}$$

$$\eta_{pvt} = \frac{\int_{t_1}^{t_2} (Q_w + A_c E_{pv}) dt}{\int_{t_1}^{t_2} A_c G dt} = \eta_w + \gamma \eta_{pv} \quad (27)$$

A MATLAB 2016 was used to solve thermal equations and establishing characteristic curves.

4. Experimental Results

The experimental results taken on 18 and 21 July-2017 were about the average temperature, temperature on the modules parts and the electrical characteristics which were obtained by the multi-channel thermometer, solar power meter and solar module analyzer device.

4.1. Average Temperature

Several factors influenced the solar panel efficiency. These factors are: direction and intensity of solar radiation, angle of inclination, in addition to the ambient temperature. Direction and angle are fixed to the south and at 45°, therefore, the influencing factors will be the solar radiation and temperature on which the photovoltaic depends on the electricity generation.

On 18/7, the test was done on both models with constant water flow rate ($\dot{m}=10$ l/h), and the average temperature on the two modules panel at 12:00 is 68.68 °C for module I, 76.7 °C for module II and for the traditional panel is 85.36 °C with ambient temperatures is 48.7 °C. This indicates that the two modules operate at hot weather effectively and their average temperatures are less than that for the traditional panel in the rate of (35.7, 30.58) % for module I and (12.76, 12.3) % for module II, respectively, Fig. (8).

On 21/7, the flow rate is increased to 15 l/h, and the average temperature on the two modules panel at 12:00 is 64.06 °C for module I, 75.53 °C for module II and for the traditional panel is 86 °C in the rate of 34.2 % for module I and 13.86 % for module II with ambient temperatures 47.2 °C. The average temperature for the modules increases with the increase in the ambient temperature and radiation, Fig. (8). The increasing of the flow rate to 15 l/h did not have a significant effect, but the effect of ambient temperature is noticeable, indicating that the amount of heat withdrawn from the condenser needs a lower flow rate.

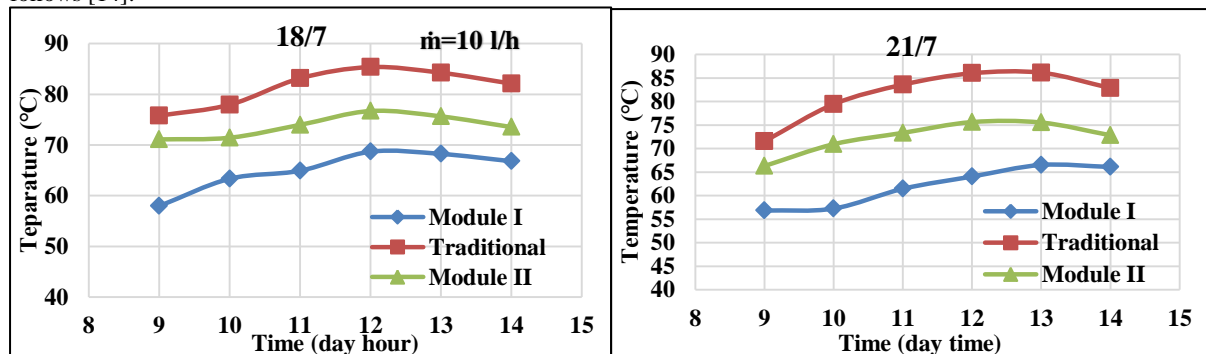


Figure 8. Average temperature.

4.2. Characteristics of Panel

The most important part in this study is the characteristics of the panel, which is the result of the study about the short and max current, the open and max voltage, the max power and the efficiency of the solar panel obtained by the solar module analyzer device. On 18/7, at 12:00 the open voltage is 33.84 V, short current is 2.1453 Ampere, max power is 50.5623 Watt, max voltage is 26.384 Volt, max current is 1.9164 Ampere and the efficiency is 16.8372 % for the module I. The open voltage is 33.493 V, short current is 2.148 Ampere, max power is 50.57426 Watt, max voltage is 26.96 Volt, max current is 1.8759 Ampere and the efficiency is 16.84 % for the module II, while for traditional panel: the open voltage is 32.366 Volt, short current is 2.0571 Ampere, max power is 45.4297 Watt, max voltage is 24.908 Volt, max current is 1.8239 Ampere and the efficiency is 15.128 %. with average temperature is 64.06 °C for module I, 76.7 °C for module II and 85.36 °C for traditional panel. The overall characteristics for module I and module II are close and

better than that for the traditional panel with photovoltaic temperature decrease, as shown in 18/7 the 21/7 as well, Fig. (9).

5. Theoretical Results

To solve the four-parameter model, a MATLAB computer program is used to evaluate the characteristics of photovoltaic panel. The temperature of panels and solar radiation intensity are adopted from the experimental data. Figure (10) shows that the theoretical results are very closer between the modules like experimental results. Table (1) shows the difference between the experimental and theoretical photovoltaic characteristics results. Theoretical efficiency of module I and module II are less than experimental in a rate of 12.7% and 15.6% respectively for 18/7 and 4% and 10% respectively for 21/7. Solar panel is influenced by several external factors, such as dust, wind, humidity, and interior factors such as multicellularity which led to a difference between the experimental and theoretical results.

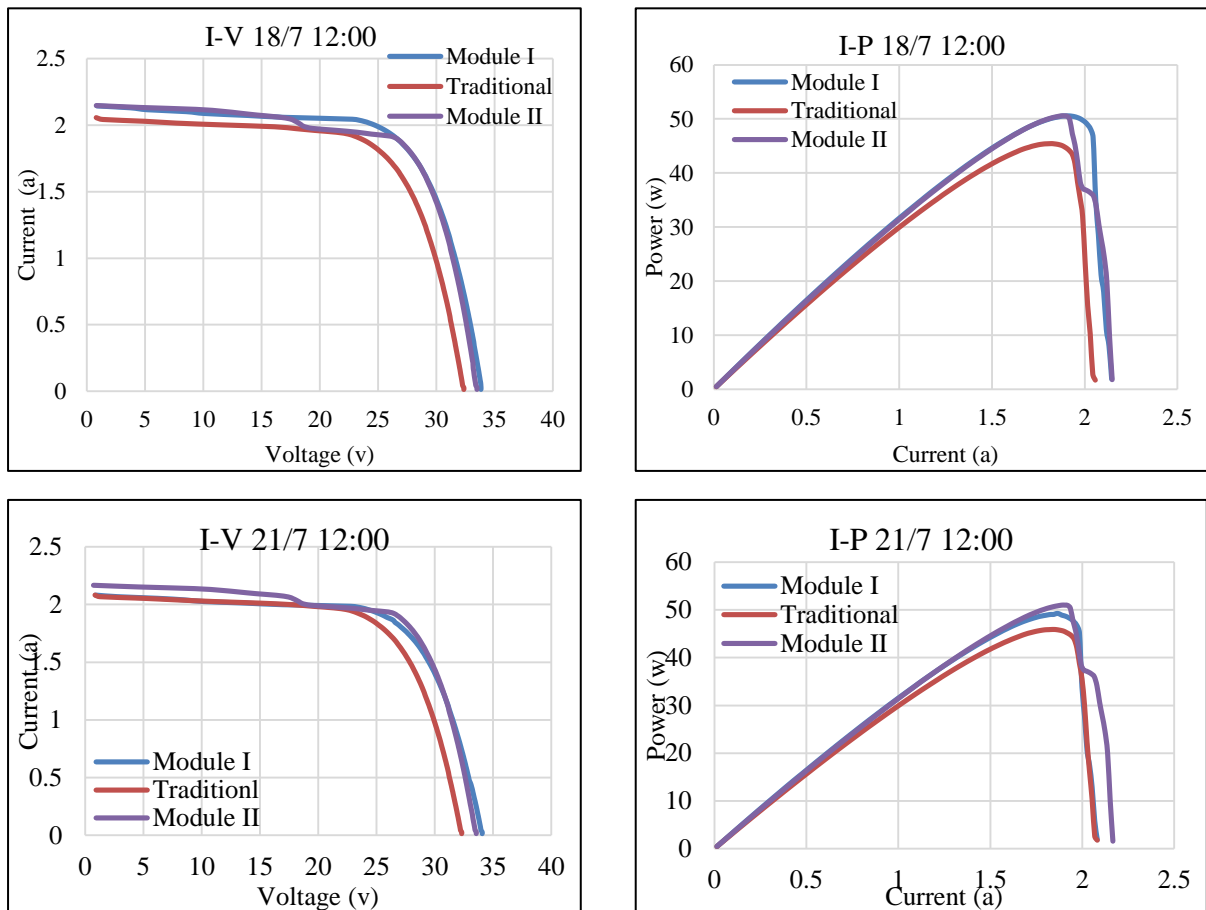


Figure 9. Photovoltaic characteristics.

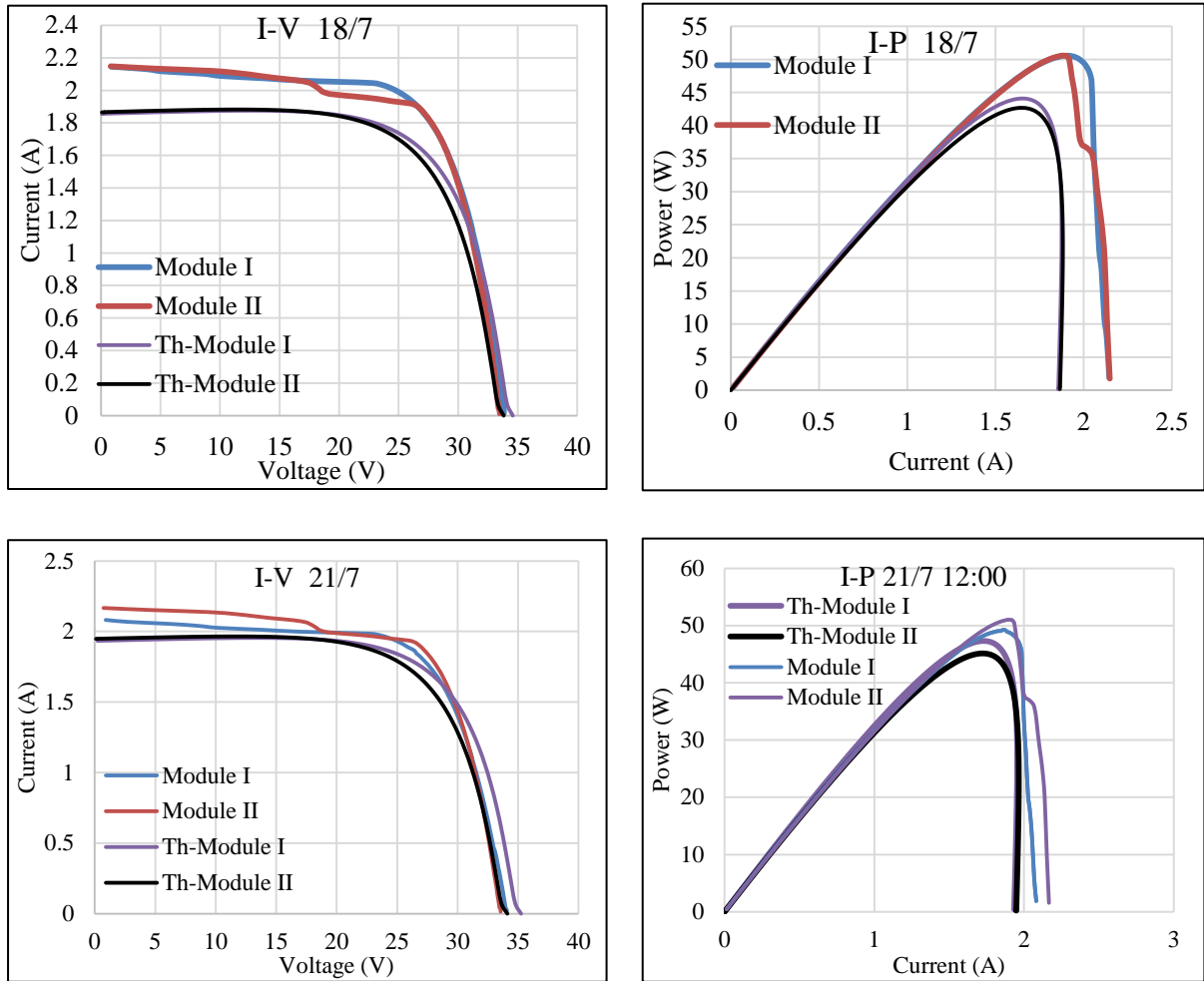


Figure 10. (I-V) and (I-P) for 18-21/7/2017 at 12:00 with radiation (724.7 W/m^2).

Table I. Experimental and theoretical characteristics of PV for 18, 21/7/2017 at 12:00.

Property 18/7/2017	Module I	Theoretical I	Module II	Theoretical II	Traditional
Temperature °C	64.06	64.06	76.7	76.7	85.36
Vopen V	33.84	34.5867	33.493	33.82	32.366
Ishort A	2.1453	1.927	2.148	1.865	2.0571
Pmax W	50.5623	44.08986	50.57426	42.68206	45.4297
Vmaxp V	25.26.384	26.58674	26.96	25.82052	24.908
Imaxp A	1.9164	1.658341	1.8759	1.653.29	1.8239
EFF%	16.8372	14.685	16.84	14.212	15.128
Property 21/7/2017	Module I	Theoretical I	Module II	Theoretical II	Traditional
Temperature °C	64.06	64.06	75.63	75.63	86
Vopen V	34.062	35.24228	33.553	34.10882	32.303
Ishort A	2.0818	1.932858	2.1667	1.947297	2.0818
Pmax W	49.2523	47.29924	51.0137	45.12669	45.9124
Vmaxp V	26.484	27.24228	26.96	26.10882	24.874
Imaxp A	1.8597	1.736243	1.8922	1.728408	1.8458
EFF%	16.4	15.75	16.983	15.3	15.294

6. Conclusions

The present research done to improve the performance of photovoltaic panel by cooling it by using thermosyphon heat pipe, the experiments carried out at different intervals proved the success of this method in reducing the temperature of the solar panel compared to the traditional panel, which improved the characteristics of the panel and the resulting in higher capacity and efficiency. Average temperature for module I is between 55-65 °C, module II 72-76 °C and for traditional panel is 70-more than 80 °C in July. Module I temperature is less than the module II and the two modules are less than the traditional panel in a rate of (15-30) % for module I and (10-14) % for module II.

References

- [1] Sharma A., Tyagi V. V., Chen C.R., Buddhi D., (2009), "Review on thermal energy storage with phase change materials and applications ", *Renew sustain Energy Rev*, Vol.13, pp. 45-318.
- [2] F. Grubišić-Čabo, S. Nizetić, T. Giuseppe Marco, (2016), "Photovoltaic Panels: A Review of the Cooling Techniques", *Transactions of Famena XI - Special issue 1*, University of Catania, Italy.
- [3] Akbarzadeh, T. Wadowski. (1996), "Heat pipe-based cooling system for photovoltaic cells under concentrated solar radiation", *Applied Thermal Engineering*, Vol. 16, No. 1, pp. 81-87.
- [4] J. K. Tonui and Y. Tripanagnostopoulos, (2007), "Improved PV/T solar collectors with heat extraction by forced or natural air circulation" *Renewable Energy* 32, pp. 623–637.
- [5] William G. Anderson, Sanjida Tamanna, David B. Sarraf, and Peter M. Dussinger, (2008) "Heat Pipe Cooling of Concentrating Photovoltaic (CPV) Systems", *Advanced Cooling Technologies, Inc., Lancaster, PA*, 17601.
- [6] Tang X., Quan Z. and Zhao Y., (2010), "Experimental investigation of solar panel cooling by a novel micro heat pipe array", *Energy and Power Engineering*, Vol.2, pp. 171-174.
- [7] N. Marc-Alain Mutombo, (2016), "Studied the Performance analysis of thermosyphon hybrid photovoltaic thermal collector", *Journal of Energy in Southern Africa*. Vol.27, No.1.
- [8] Pei Gang, Fu Huide, Zhang Tao and Ji Jie, (2011), "A numerical and experimental study on a heat pipe PV/T system", *Solar Energy* 85, pp. 911–921.
- [9] John A. Duffie and William A. Beckman, (2013), "Solar engineering of thermal processes", *Book*, Fourth Edition.
- [10] Ahmed Hikmet Jassim, (2016), "Improving Solar Collector Performance by Heat Pipe", *Ph.D. Theses*, University of Technology.
- [11] Pei Gang, Fu Huide, Zhang Tao and Ji Jie, (2012), "Performance study and parametric analysis of a novel heat pipe PV/T system", *Energy* 37, pp. 384-395.
- [12] Tiwari Arvind and Sodha MS (2005), "Performance evaluation of solar PV/T system: an experimental validation". *Solar Energy* 80, pp.751–759.
- [13] Incropera, F. P., DeWitt, D. P., Bergman, T. L., Lavine, A. S., (2007). "Fundamentals of Heat and Mass Transfer", 6th Edition, *John Wiley & Sons*, New York, p-428.
- [14] Laith J. Habeeb, Dheya G. Mutasher, Faez A. Abd Ali., (2017). "Cooling Photovoltaic Thermal Solar Panel by Using Heat Pipe at Baghdad Climate", *International Journal of Mechanical & Mechatronics Engineering IJMME-IJENS* Vol:17 No:06.

Prediction of Flow Parameters of Glass Beads-Water Slurry flow through Horizontal Pipeline using Computational Fluid Dynamics

Shofique Ahmed*, Rajesh Arora, Om Parkash

Department of Mechanical Engineering, Amity University Haryana, Gurgaon-122413, India

Received 6 Jun. 2018

Abstract

This paper presents a numerical analysis of two-phase glass beads-water slurry flow based on computational fluid dynamics through a 54.9 mm diameter and 4 m long horizontal pipe considering 125µm glass beads particle size over a flow velocity ranging from 1m/s to 5m/s at various volumetric concentration of the glass beads particle viz. 10%, 20%, 30%, 40% and 50%. For modeling the multiphase flow Eulerian two-phase approach was selected while for modeling the turbulence phase of the flow different turbulence models were introduced and Re-Normalization group K- epsilon model was selected after verifying the robustness of each turbulence model. Structured mesh with non-uniform spacing with a refinement near the wall boundary was selected for discretizing the entire fluid domain while control volume finite difference approach was selected for solving the Navier- Stokes governing equations in Analysis System 14.0 software package. Different flow variables like flow velocity distribution, pressure drop, concentration distribution of the particles, turbulence of the flow and their effects are studied and analyzed. In this study, a generalized mathematical relationship among pressure drop, volumetric concentration and turbulence of the flow has been proposed. The proposed mathematical relationship is then validated against the experimental data available in the previous literature and it was observed that the proposed model can forecast the pressure drop analytically with minimal error. It can be concluded from this study that the solid particles exhibit an asymmetrical distribution pattern along the vertical plane of the pipe cross section. However, as the flow velocity increases the solid particles are observed to be more blended with the liquid and leads to more symmetrical distribution. On the other hand, as the volumetric concentration increases the solid particles experience a more asymmetric distribution pattern and at low flow velocity and high volumetric concentration solid particles are settled at the bottom of the pipe. Volumetric concentration and flow velocity show a direct impact on the pressure drop where the pressure drop rises with the increase in volumetric concentration and flow velocity. Moreover, the comparison of the simulated results proves the practical utility of proposed model and high designing capability of Eulerian-Eulerian model with RNG k-ε turbulence model.

© 2018 Jordan Journal of Mechanical and Industrial Engineering. All rights reserved

Keywords: 3D CFD modeling, Eulerian two-phase model, RNG K-epsilon model, Concentration distribution, Flow velocity distribution, Pressure drop, Slurry pipeline;

Nomenclatures				
Notation	Description	Unit		
α_s	Volumetric concentration of solid	-	Y'	Normalized radial position
α_f	Volumetric concentration of fluid	-	Y	Distance from bottom to top of the pipe along vertical plane
ΔP	Pressure difference	Pa	D	Diameter of the pipe
K_{sf}	Drag coefficient of inter-force	N	L	Length of the pipe
V	Flow velocity of mixture	m/s	Re	Reynolds number
v_s	Flow velocity of solid particles	m/s	ρ	Mass Density
v_f	Flow velocity of fluid	m/s	ρ_f	Mass density for liquid phase
$\bar{\tau}_f$	Stress tensor for fluid phase	N/m ²	ρ_s	Mass density for solid phase
C_{vm}	Coefficient of virtual mass force	N		
C_{vf}	Volumetric concentration of solid particles	-		
C_L	Coefficient of lift	-		
$\mu_{t,f}$	Turbulent viscosity	Pa.s		
k_f	Turbulent kinetic energy	m ² /s ²		
ϵ_f	Turbulent energy dissipation rate	m ² /s ³		
$C(y')$	Predicted concentration distribution of			

1. Introduction

Transportation of solid materials through pipelines has been a common practice over the years in many industries including power generation industries, construction industries, food processing industries, oil and gas, pharmaceutical mining industries chemical industries etc. This mode of transportation of solid materials is preferred to the conventional mode of transportation because it

* Corresponding author e-mail: uddinshofique1991@gmail.com.

reduces environmental hazards, air pollution, less road traffics and more economical. Here solid materials are blended with fluid to form slurry and the slurry is then pumped through the pipeline. There are many terminologies available to classify the slurry flow, but the most frequent categorization is homogenous, heterogeneous, moving bed, stationary bed, and saltation slurry flow regime. Heterogeneous slurry flow regime is the most occurring flow regime among this entire flow regime where the solid particles are heterogeneously distributed in the fluid. The slurry flow through pipeline cannot be considered as pseudo-fluids because the solid particles tend to settle at the pipe bottom; hence it experiences a totally different flow patterns compared to the flow of pure fluid hence it is essential to have a detailed idea about the flow patterns and the behavior of various slurry flow parameters for a better understanding of the slurry flow problems. Many empirical approaches have been developed over the years for a better prediction of the characteristics of various slurry flow parameters. Computational fluid dynamics (CFD) is a sophisticated platform which allows us to explain a wide variety of multiphase flow problems with greater ease and at low cost. Wide range of flow conditions can be solved rapidly which is more or less impracticable with experimental work. It provides a wide range of exclusive clue about the variation of the flow variables inside the flow domain. There are relatively few works on the analysis of slurry flow using CFD technique which gives an exclusive opportunity to the researcher to understand the whole slurry flow process applying CFD technique. Pressure drop, particle flow velocity distribution and the solid particle distributions are the most manipulating flow parameters in a slurry flow process and researchers are aiming for developing a generalized approach to predict the behavior of these flow parameters more precisely since the third decades of the 20th century. Seshadri et. al [1] developed a mathematical correlation which could predict the solid particles distribution in a slurry flow through open channel flow, rectangular ducts and circular pipes. Roco and Shook [2] developed a straightforward algorithm using differential equations for predicting the distribution of solid particles and distribution of particle velocity in a slurry flow containing volumetric concentration less than 40% through pipelines of various pipe diameters. Following their work, Roco and Shook [3] developed a computational model for two-phase analysis of heterogeneous coal-water slurry flow to predict the behaviour of concentration distribution and flow velocity distribution. A two-layer approach was established by Gillies et. al [4] For the analysis of a slurry flow containing coarse particles of coal, gravel and sand and various flow parameters like pressure gradient and concentration distribution of solid particles were precisely predicted using their proposed model; their model was in a good consistency with the data collected from their experimental setup. Gillies and Shook [5] performed a numerical investigation to forecast the pattern of particle concentration distribution in a two-phase solid-fluid slurry flow. Conclusions that were drawn based on their analysis were that the solid particles interaction is limited to the region near the wall boundary and the interaction becomes more spectacular when the particle size becomes larger.

Doron and Berena [6] proposed a three-layer approach for predicting the distribution of particles and pressure gradient in a solid-liquid mixture slurry flow. From their new study they found out that the concentration distribution of the solid particles affects pressure drop. Mukhtar et. al [7] performed an experimental analysis on heterogeneous zinc-iron slurry through long 90° pipe bend. They forecasted the variation of pressure drop in pipe bends at various flow velocity and solid volumetric concentration. Bellus et. al [8] analyzed the pressure gradient of ice slurries containing 5% propylene in water in plate heat exchanger. From their analysis, they concluded that the pressure gradient increases by 15% when volumetric concentration of ice increases from 0% to 20%. Matousek [9] conducted an experimental analysis of sand-water slurry flow through different 35° descending, horizontal and vertical pipes for determining the pressure drop and flow patterns. From their study they found out that pressure drop is lower for smaller sand particles than that of larger sand particles. Also, in vertical pipe the pressure drop is lower than that of horizontal pipe. Scott and Steven [10] studied the slurry flow containing coarse and fine sediments of clay with a varying particle size of the order of 600-2000µm through a horizontal pipeline of 103 mm diameter. The purpose of their work was to examine the effect of concentration of clay on pressure drop and hydraulic gradient. A theoretical model based on genetic algorithm (GA) and support vector regression (SVR) was proposed by Lahiri and Ghanta [11] to forecast the pressure gradient in a solid-liquid slurry flow. Their proposed SVR correlation significantly improved the pressure gradient prediction over an extensive variety of pipe diameters, physical properties and flow conditions. Lahiri and Ghanta [12] proposed a generalized model based on CFD for the prediction of various flow parameters of a slurry flow. Euler-Euler two-phase approach was introduced for modeling the solid-fluid flow and standard K-epsilon approach was used for modeling the turbulence phase of the flow. Using their proposed model, they predicted concentration profile and pressure drop, simulated pressure drop was compared with their experimental data and was in a good consistency. Their investigation showed that pressure gradient is less at low velocity and increases rapidly at high velocity. Chandel et. al [13] conducted an experimental investigation of a slurry flow containing highly concentrated mixture of fly ash and bottom ash and water through a horizontal pipeline. Pressure gradient of the slurry flow was measured from their experiment. Finally, they developed a rheological approach to forecast the pressure gradient and predicted pressure gradient was related with results obtained from experiments and was in a good consistency. Kaushal et al [14] conducted a numerical investigation of slurry flow containing mono-dispersed glass beads particles through horizontal pipeline. Multiphase flow was modelled using Eulerian two-phase model and mixture model while the turbulence phase of the flow was modelled using RNG K-epsilon model. Various flow parameters including pressure drop, velocity distribution and concentration distributions were analyzed in their study. Moreover, they found out that the mixture model is not an appropriate model for predicting the pressure drop correctly while Eulerian model predicts the pressure drop with a higher accuracy.

Nabil et. al [15] anticipated a generalized CFD technique to simulate solid-liquid flow. By using their model, the predicted the behaviour of different flow parameters like velocity distribution and its consequence on pressure gradient considering the influence of the size of particles into concern. From their analysis they concluded that the pressure gradient rises with the rise in concentration as well as pressure gradient rises when the velocity is higher. Kumar et. al [16] conducted a numerical investigation of a slurry flow containing 440 μm diameter sand particles and water through a horizontal pipeline. Eulerian two-phase model and standard K- epsilon model was selected for modeling the flow. From their analysis they predicted the behaviour of pressure gradient, velocity distribution and distribution of solid particles as well as pressure drop was correlated with the data obtained from experiments. Kumar [17] conducted a CFD based numerical simulation of slurry flow consisting of silica sand and water through pipe bends and straight pipes for the prediction of pressure drop. He adopted Eulerian model and K-epsilon model for the analysis. Conclusion from his study was that the pressure gradient rises with flow velocity at pipe bend. Eulerian approach and RNG K-epsilon approach were applied for CFD simulation of sand-water slurry flow through horizontal pipeline by Gopaliya and Kaushal [18]. The pressure drops characteristics along with other flow parameters were predicted in their study.

This current study represents a CFD numerical analysis of Glass beads-water slurry flow through a horizontal pipeline of 54.9 mm diameter and 4m length. Size of the glass beads particles is taken as 125 μm with specific gravity of 2.47. The simulations are conducted over a flow velocity of 1m/s, 2m/s, 3m/s, 4m/s and 5m/s at solid particle volumetric concentration of 10%, 20%, 30%, 40% and 50%. Eulerian two-phase approach was selected for modeling the multiphase flow while different turbulence models were introduced, and their robustness was verified. It was found that RNG K-epsilon turbulence approach is the most suitable for modeling the turbulence phase of the flow. A mathematical correlation was developed and validated for the analytical prediction of pressure drop over flow velocity at different volumetric concentration. Finally, the simulated outcome of pressure gradient was correlated with the experimental pressure drop available in the work of Kaushal and Tomita [19].

2. Mathematical model

Selection of proper mathematical model plays a significant character in modeling the flow problems in a numerical analysis. Slurry flow contains solid and fluid phase thus it is a multiphase flow problem. CFD software package allows the selection of various multiphase models like discrete phase, mixture and Eulerian multiphase model for the modeling of the complex multiphase flow. Slurry flows not being a dilute phase flow problem; usage of discrete phase model is restricted for modeling its flow. Kaushal et. al [14] suggested that the mixture model cannot determine the pressure gradient of a slurry flow accurately, hence based on their study Eulerian two-phase model is adopted in this present study. In this study, the solid particles were assumed to be mono-dispersed. In other words, the solid particles were assumed to behave

like liquid particles because of its dispersed nature. Moreover, the granular version of Eulerian model is preferred to the non-granular version because unlike non-granular version, it considers the collision and friction among the solid particles which is essential for slurry flow. For modeling the turbulence phase of the flow several turbulence models were introduced in this present study and their robustness was determined, it was found that the RNG K-epsilon approach is the best suited model for modeling the turbulence phase of this slurry flow problem.

2.1. Eulerian model

The Eulerian model cannot differentiate solid-fluid and fluid-fluid multiphase flows. In Eulerian model, it is assumed that the slurry flow comprises separate fluid and solid phases, and they structure a continuum, so that the volume concentration of solid (α_s) and fluid (α_f) is equal to 1. i.e. $\alpha_s + \alpha_f = 1$. This model satisfies both law of conservation of momentum and mass for solid and liquid individually. The forces that act on a single fluid particle are:

- Static pressure gradient, ΔP .
- Inertial force caused by interaction of particles or solid pressure gradient ΔP_s .
- Difference in velocity between the solid and fluid phase causes the drag force, $K_{sf}(\vec{v}_s - \vec{v}_f)$ where, K_{sf} is the drag coefficient of inter-force, where \vec{v}_f the velocity of fluid is phase and \vec{v}_s is the velocity of solid phase.
- Forces due to viscosity, $\nabla \cdot \bar{\tau}_f$, $\bar{\tau}_f$ is being the stress tensor for fluid phase.
- $\rho \vec{g}$, is the body force.
- Virtual mass force, $C_{vm} \alpha_s \rho_f (\vec{v}_f \nabla \vec{v}_f - \vec{v}_s \nabla \vec{v}_s)$ where, C_{vm} is the coefficient of virtual mass force and is taken as 0.5 in this current work.
- Lift force, $C_L \alpha_s \rho_f (\vec{v}_f - \vec{v}_s) \times (\nabla \times \vec{v}_f)$, where, C_L is the coefficient of lift, taken as 0.5 in this current work.

2.2. Governing equations

The Continuity and Momentum equations are formulated as [14]

Continuity Equation

$$\nabla \cdot (\alpha_t \rho_t \vec{v}_t) = 0, \text{ t being either solid or fluid} \quad (1)$$

Momentum Equation for fluid phase

$$\nabla \cdot (\alpha_f \rho_f \vec{v}_f \vec{v}_f) = -\alpha_f \nabla P + \nabla \cdot \bar{\tau}_f + \alpha_f \rho_f \vec{g} + K_{sf}(\vec{v}_s - \vec{v}_f) + C_{vm} \alpha_f \rho_f (\vec{v}_s \cdot \nabla \vec{v}_s - \vec{v}_f \cdot \nabla \vec{v}_f) + C_L \alpha_s \rho_f (\vec{v}_f - \vec{v}_s) \times (\nabla \times \vec{v}_f) \quad (2)$$

Momentum Equation for solid phase

$$\begin{aligned} \nabla \cdot (\alpha_s \rho_s \vec{v}_s \vec{v}_s) = & -\alpha_s \nabla P - \nabla P_s + \nabla \cdot \bar{\tau}_s + \alpha_s \rho_f \vec{g} \\ & + K_{sf}(\vec{v}_f - \vec{v}_s) \\ & + C_{vm} \alpha_s \rho_f (\vec{v}_f \cdot \nabla \vec{v}_f - \vec{v}_s \cdot \nabla \vec{v}_s) \\ & + C_L \alpha_s \rho_f (\vec{v}_s - \vec{v}_f) \times (\nabla \times \vec{v}_f) \quad (3) \end{aligned}$$

2.3. Turbulence model

The turbulent model is solved using RNG K- ϵ model along with other additional conditions causing interfacial turbulent momentum transfer. The fluid phase Reynolds stress tensor is given by:

$$\overline{v_i v_j} = -\frac{2}{3}(\rho_f k_f + \mu_{t,f} \nabla v_f) \bar{I} + \mu_{t,f} (\nabla v_f + \nabla v_f^{tr}) \quad (4)$$

Here $\mu_{t,f}$ is the viscosity corresponding to turbulence. An analytical differential interrelationship for turbulent viscosity is provided with RNG K- ϵ model for modeling the flow at lower Reynolds number. At large Reynolds number (which is the case in current study) this analytical correlation converts to:

$$\mu_{t,f} = \rho_f C_\mu \frac{k_f^2}{\epsilon_f} \text{ With } C_\mu = 0.09 \quad (5)$$

The prediction of turbulent kinetic energy k_f and turbulent energy dissipation rate ϵ_f by Standard K- ϵ and RNG K- ϵ approach is almost very much alike. Standard and RNG k - ϵ approach differ in such a fashion that RNG k - ϵ approach contains a supplementary expression in the ϵ equation:

$$R_\epsilon = \frac{C_\mu \rho \eta^3 (1 - \eta/\eta_0) \epsilon^2}{(1 + \beta \eta^3) k} \quad (6)$$

Where, $\eta = Sk/\epsilon$, $\eta_0 = 4.38$, $\beta = 0.012$, the constant parameters are taken as $C_{\mu m} = 0.0845$, $C_{1\epsilon} = 1.42$, $C_{2\epsilon} = 1.68$, $C_{3\epsilon} = 1.3$, $\sigma_k = 0.75$, $\sigma_\epsilon = 1.2$

2.4. Wall functions

Wall functions are collections of empirical and semi-empirical formulae that yield a better solution near the wall boundary of a flow domain. In this study due to the presence of higher gradient terms the near wall boundary of the flow domain demands a special treatment during the simulation. This can be obtained by selecting standard wall functions accessible with the RNG K- ϵ model.

3. Numerical Solution

3.1. Geometry and mesh

A circular pipe of 4 m length and 54.9 mm diameter is modeled in ANSYS workbench design modular which defines the computational flow domain for this slurry flow problem. Structured hexa core elements with non-uniform spacing have been selected for discretizing the flow domain using multizone method. Seven inflation layers with smooth transition size of 0.05 mm and growth ratio of 1.2 has been introduced for refining the mesh size near the boundary wall. The generated mesh contains approximately 200901 elements.

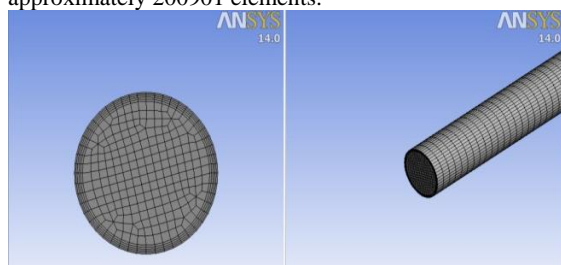


Figure 1. 2D and 3D view of generated mesh

3.2. Boundary conditions

Three faces enclosing the flow domain has been introduced namely outlet boundary, wall boundary and inlet boundary. Values are specified at those boundary conditions to initiate the flow through the flow field. Details of the boundary condition are shown in Table 1.

Table 1: Types of boundary conditions applied to the flow domain.

Boundary location	Boundary type	Turbulence (specification method)
Inlet	Fluid phase: velocity inlet in Z direction Solid phase: velocity inlet in Z direction and volumetric concentration $\alpha_s = C_{vf}$	Turbulent intensity=3.5% Hydraulic diameter=0.0549
Wall	No slip boundary condition for fluid phase Full slip boundary condition for solid phase	-
Outlet	Fluid phase: pressure outlet Solid phase: pressure outlet	Turbulent intensity=3.5% Hydraulic diameter=0.0549

3.3. Solution strategy and convergence criteria

In this current work, the Navier-Stokes governing equations are solved in FLUENT 14.0 software package. Finite difference control volume approach was selected for discretizing momentum and mass equations. Momentum equation, turbulent kinetic energy and turbulent dissipation rate are discretized with second order upwind scheme and volumetric concentration is discretized with first order upwind scheme. For pressure and velocity coupling phase coupled SIMPLE algorithm is selected. Convergence of problem depends on the scaled residual. For this flow problem the residuals contain continuity, X-velocity, Y-velocity, Z-velocity for both the phases; k and ϵ for fluid phase and volumetric concentration for solid phase which need to be converged at some specific region. Application of these schemes confirmed better stability, accuracy and convergence of the flow problem. Moreover, decreasing the value of under relaxation factors ensured better convergence of the problem. URF (under relaxation factor) for volumetric concentration has been reduced to 0.3 from 0.5 and for momentum it has been reduced from 0.7 to 0.5.

3.4. Grid independency test

In every numerical analysis it is highly recommended to select an optimal mesh for the analysis of flow patterns and flow parameters with higher accuracy. In this study a grid independency test is introduced where five mesh with different number of elements viz. 95000, 150000, 201000, 310000 and 387000 are introduced. Using this mesh, the problem has been simulated applying same boundary conditions (velocity=5 m/s and $C_{vf}=0.5$) for all mesh and velocity profile is drawn for each mesh. Plots of the outcome are shown in figure 2.

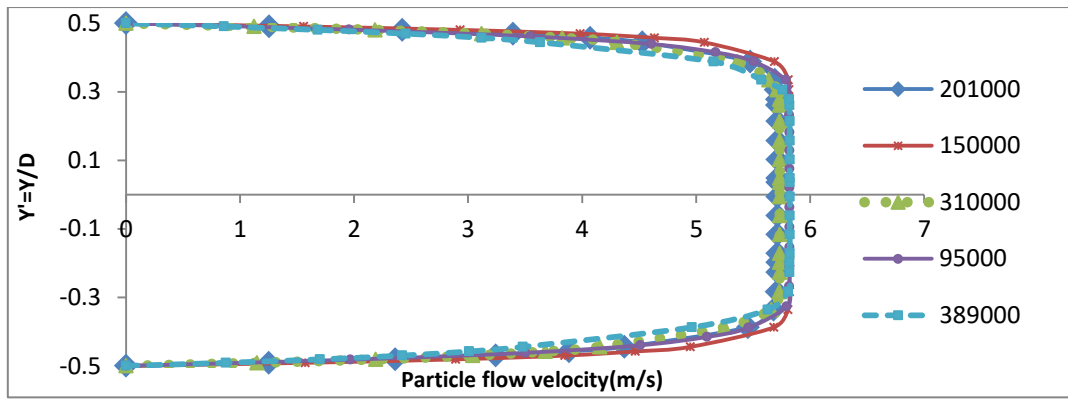


Figure 2. Velocity distributions for different mesh at $V = 5\text{ m/s}$ and $C_{vf} = 0.5$

It is confirmed from figure 2 that the velocity profile of the mesh containing 201000 elements and the mesh containing 310000 elements are super imposing with each other. So, the mesh containing 201000 elements has been considered as optimal mesh and it is used for the final calculation in this present study.

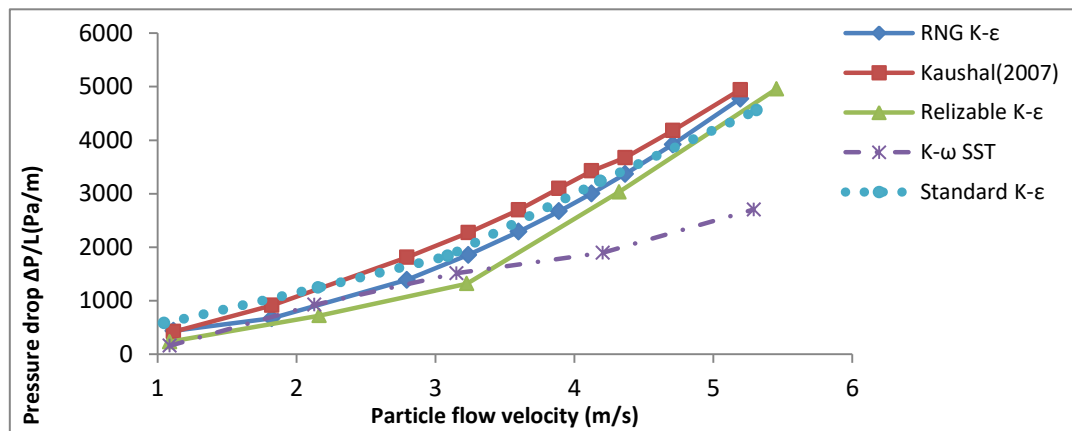


Figure 3. Comparison of experimental and simulated pressure drop at $C_{vf} = 0.3$ using different turbulent model.

3.5. Validation of turbulence model

The turbulence model of this slurry flow is validated with data obtained from the experiments obtainable in the work of Kausal and Tomita [26]. For validating the model, several test simulation runs are carried out using RNG K-epsilon model, Standard K-epsilon model; Realizable K-epsilon model and K-omega SST model along with Eulerian two-phase approach to investigate the precision of these turbulence models in forecasting the experimental pressure drop data. From figure 3, it can be noticed that the RNG K-epsilon turbulence model is the most robust model in forecasting the pressure drop compared to other turbulence model thus confirming the validity of the simulation model.

The simulation matrix used in performing the simulation in this study is shown in table 2 where RNG K-epsilon model along with Eulerian two-phase model are adopted for all the simulation.

4. Results and discussions

4.1. Concentration profile of solid phase

This section shows the simulated values of solid volumetric concentration along a vertical centerline of the pipe cross section at the outlet. $C(y')$ is the predicted solid

particles concentration distribution along the pipe cross section at the outlet, C_{vf} is the volumetric concentration of solid particles, which can be computed as the mean value over the length of the chord in Y direction, mathematically presented as below:

$$C_{vf} = \frac{1}{2y} \int_{-y}^{+y} \alpha_s(y, Y') dy \quad (7)$$

Where $Y' = Y/D$, Y is the height of the vertical centerline from bottom to top of the pipe cross section in Y-direction.

Table 2. Description of simulation parameters used in this study.

Simulation parameters	Values
Pipe diameter (D)	0.0549 m
Pipe length (L)	4 m (> 50D)
Size of glass beads particle (D_p)	125 μm
Particle Solid volumetric concentration	0.1 to 0.5 (10% to 50%)
Specific gravity of particle	2.47
Specific gravity of water	1.00
Velocity of mixture	1m/s to 5m/s
Turbulence equation	RNG K-epsilon
Multiphase model	Eulerian two-phase model

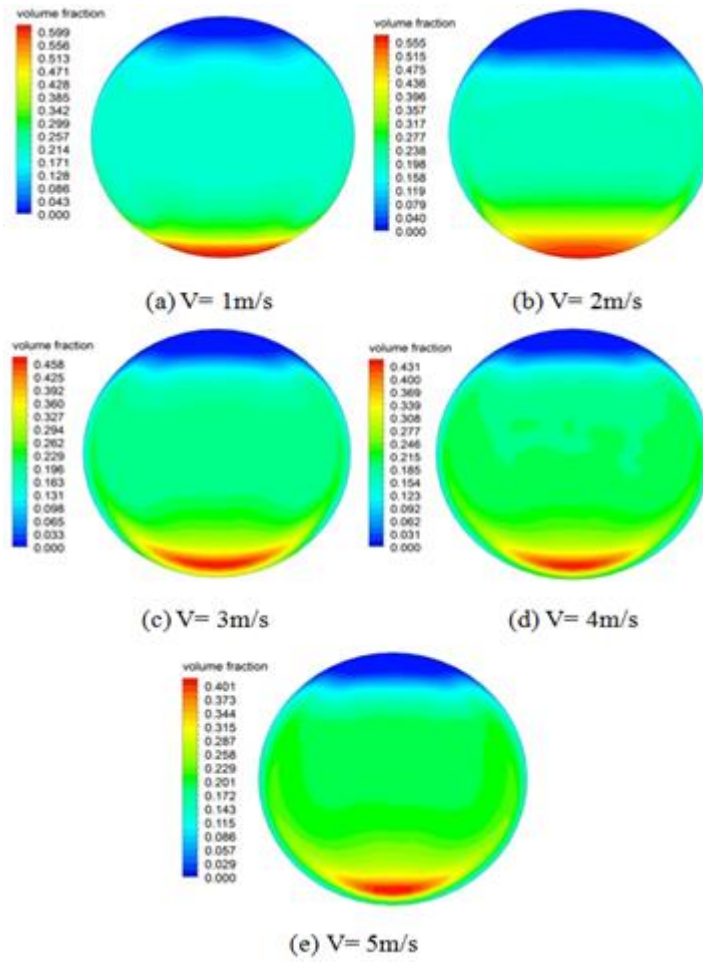


Figure 4. Solid concentration distribution α_s predicted at $C_{vf}=0.2$

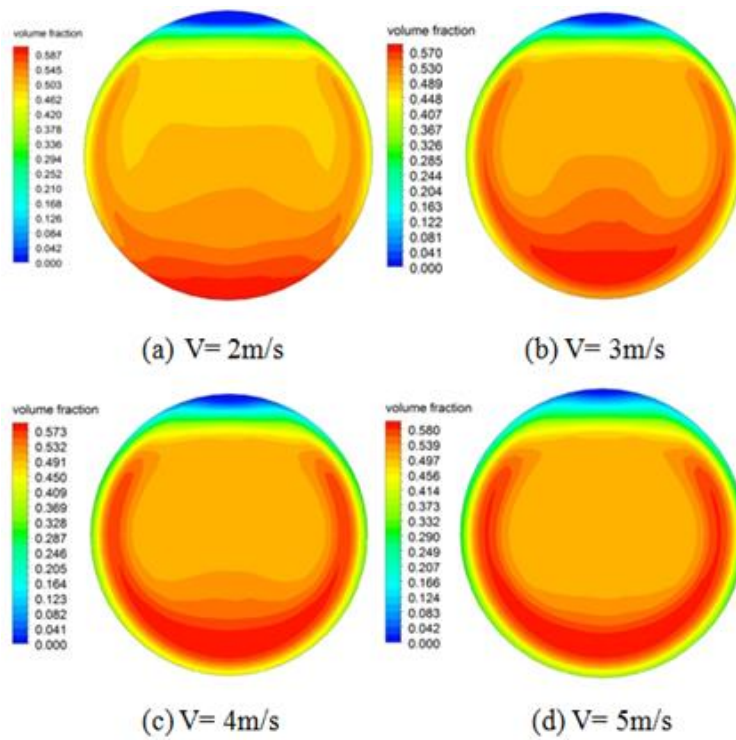


Figure 5. Solid concentration distribution α_s predicted at $C_{vf}=0.5$

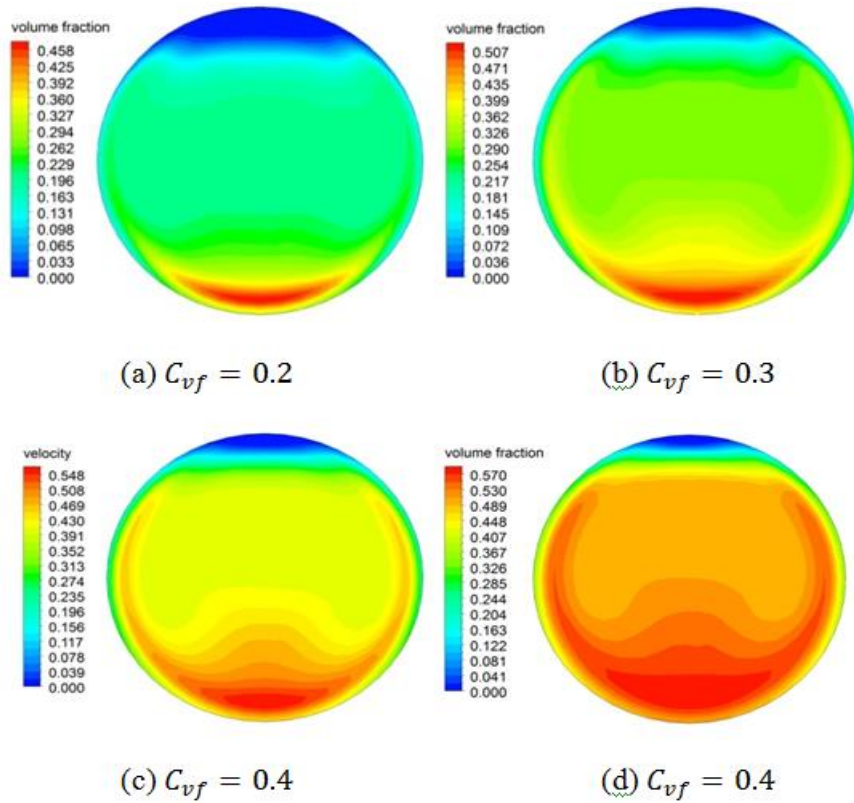


Figure 6. Solid concentration distribution α_s predicted at $V=3\text{m/s}$ for different volumetric concentration.

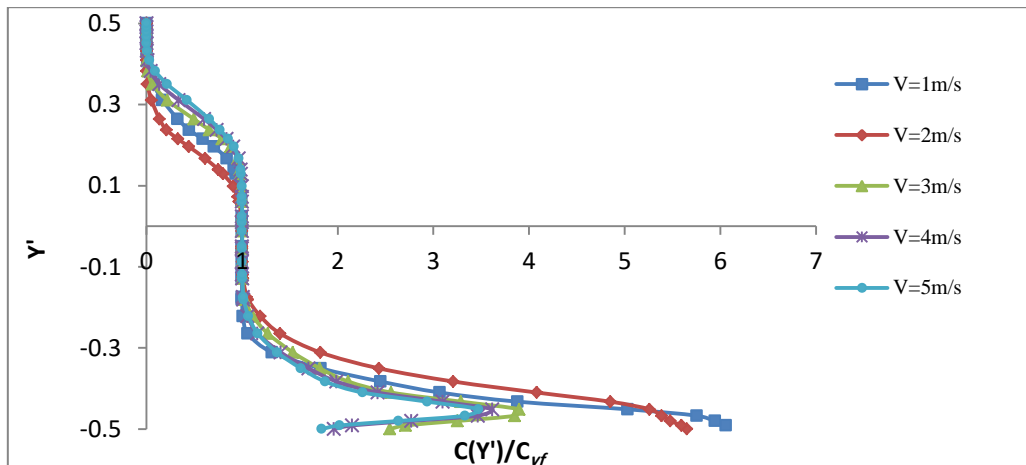


Figure 7. Plots of predicted solid concentration $\alpha_s(-y, y)$ at $C_{vf} = 0.1$

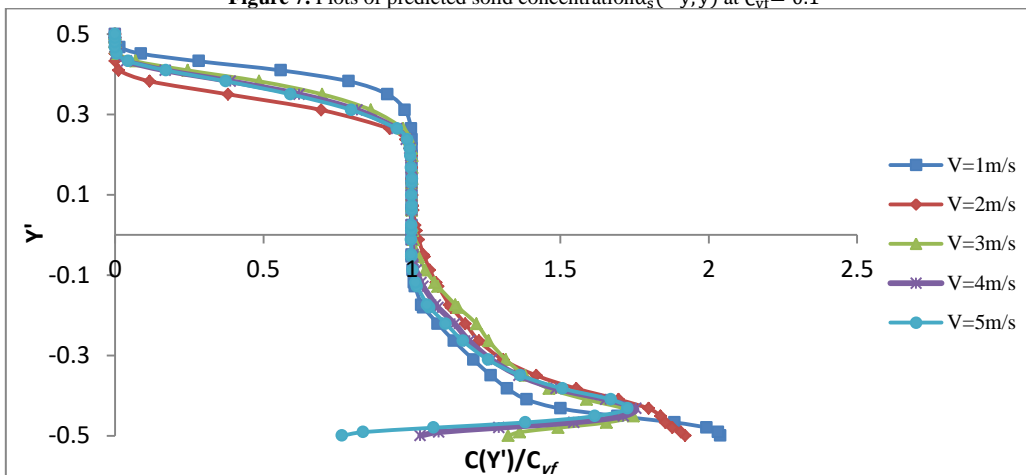


Figure 8. Plots of predicted solid concentration $\alpha_s(-y, y)$ at $C_{vf} = 0.2$

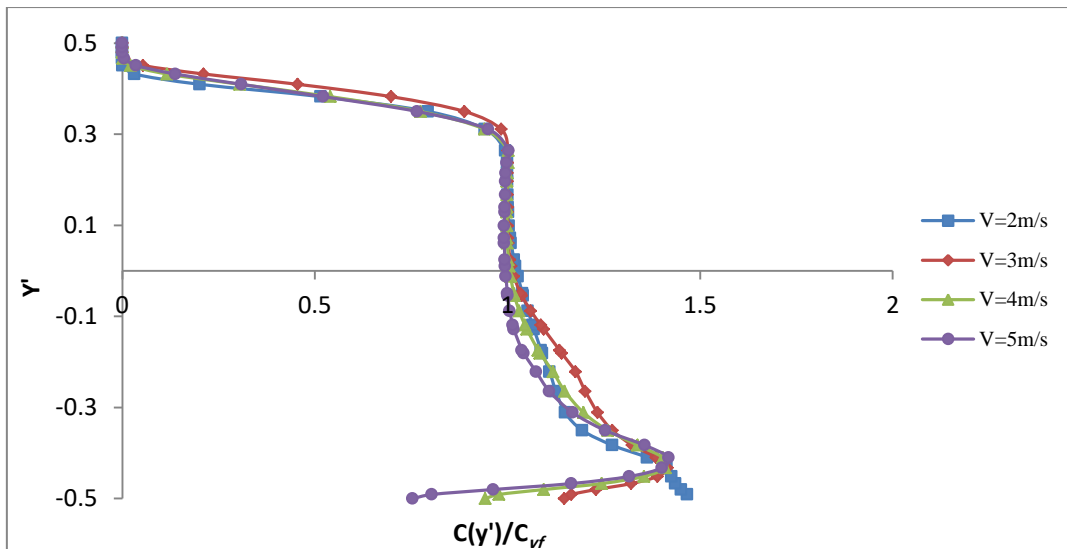


Figure 9. Plots of predicted solid concentration $\alpha_s(-y, y)$ at $C_{vf} = 0.3$

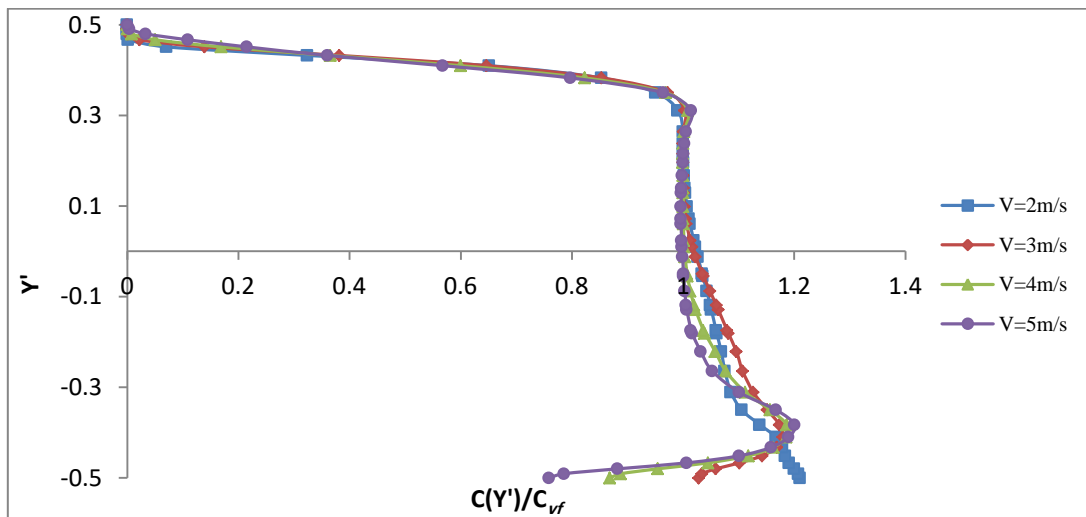


Figure 9. Plots of predicted solid concentration $\alpha_s(-y, y)$ at $C_{vf} = 0.4$

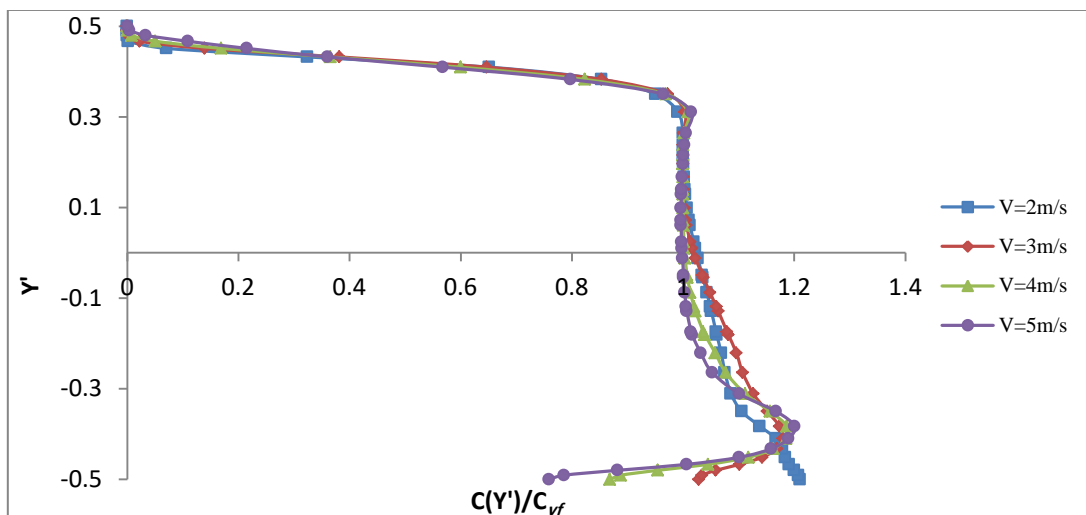


Figure 10. Plots of predicted solid concentration $\alpha_s(-y, y)$ at $C_{vf} = 0.5$

4.1.1. Effect of particle flow velocity and volumetric concentration of solid particles on concentration distribution of solid particles

It may be examined from figure 4 to 10 that solid particles distribution shows an asymmetrical nature along the vertical plane and the solid particles are likely to accumulate at the pipe base because of effect of gravitation and the high concentration zone is established at the base of the pipe. It is noteworthy that for each constant volumetric concentration as the flow velocity increases the particles become more buoyant and suspended in the fluid rather than settling down at the pipe bottom, this is because of the reason that with the rise in velocity the turbulence of the flow becomes high which is accountable for the buoyancy of solid particles. Furthermore, the contact of solid particles with the pipe wall becomes more visible at higher flow velocities [Refer Figure 4, 5, 7, 8, 9, 10]. It may also be noticed that when the volumetric concentration raises for each constant flow velocity the distribution of solid particles become more symmetric across the horizontal plane [Refer Figure 6]. This is because at high volumetric concentration turbulence of the flow increases, thereby providing a complete mixing of the solid particles with the fluid; yielding a more symmetrical particle distribution across the horizontal plane.

4.1.2. Effect of volumetric concentration of solid particles on turbulence of the flow

Figure 11 illustrates the impact of solid volumetric concentration on turbulence of the flow (Reynolds number) at a constant flow velocity viz. 1m/s, 3m/s, 4m/s and 5m/s respectively. It can be observed that at a given flow velocity the turbulence of the flow becomes higher with the rise in solid volumetric concentration. This happens because as the solid volumetric concentration rises, there is a raise in particle-particle, particle-fluid and particle-wall contacts. Moreover, at high concentration the solid particles try to gather more at the pipe bottom thereby blocking a part of

effective flow area, which causes an increase in flow velocity and hence turbulence increases.

4.2. Velocity profiles

Figure 12 to 17 demonstrate the distribution of particle flow velocity $v_{sz}(x, y)$ at solid volumetric concentration (C_{vf}) of 0.3, 0.4 and 0.5 respectively. $v_{sz}(x, y)$ is the Z component of the velocity perpendicular to the cross section of the pipe (X-Y plane). The velocity contours are obtained at the outlet of the pipe.

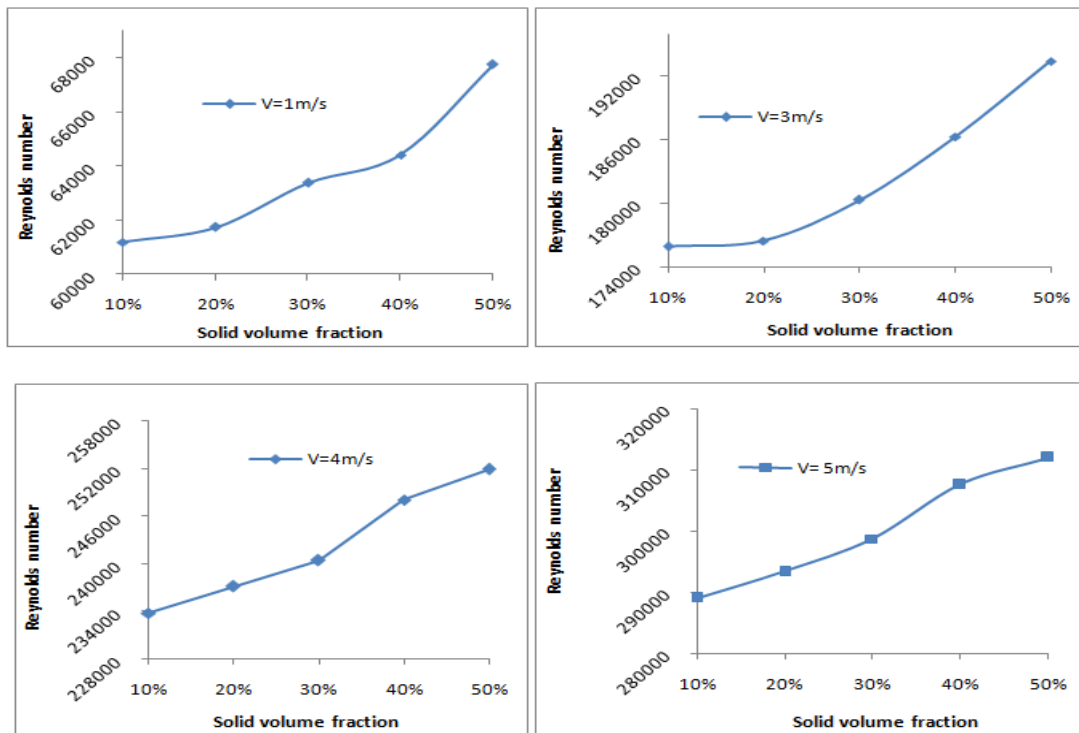


Figure 11. Plot of effects of solid volumetric concentration on turbulence of the flow.

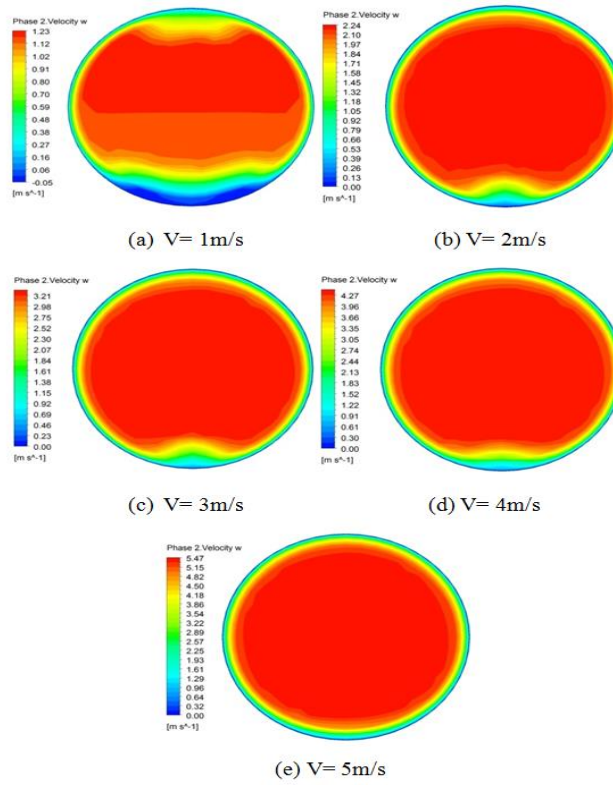


Figure 12. Simulated velocity distribution $v_{sz}(x, y)$ at $C_{vf} = 0.3$

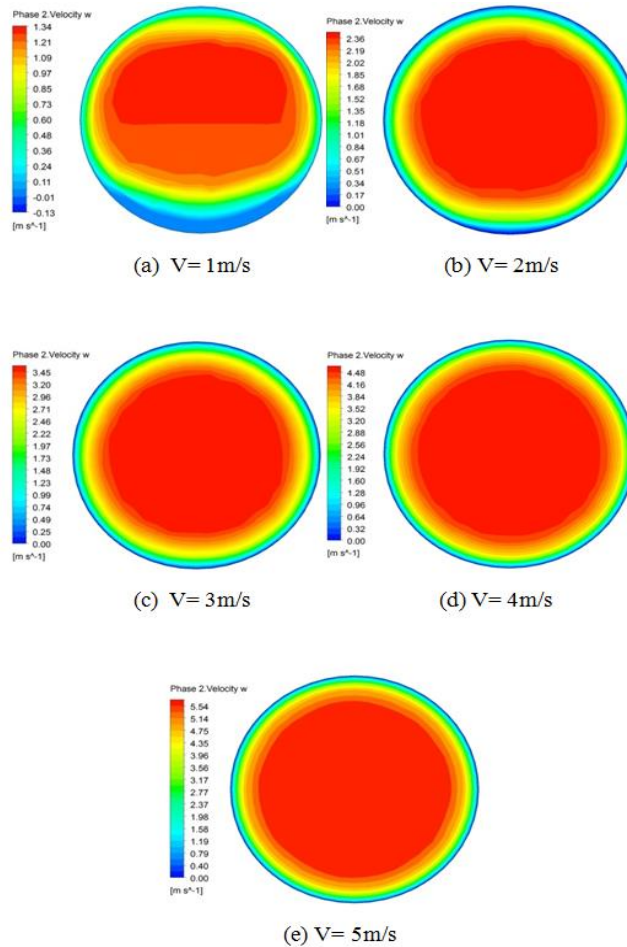


Figure 13. Simulated velocity distribution $v_{sz}(x, y)$ at $C_{vf} = 0.5$

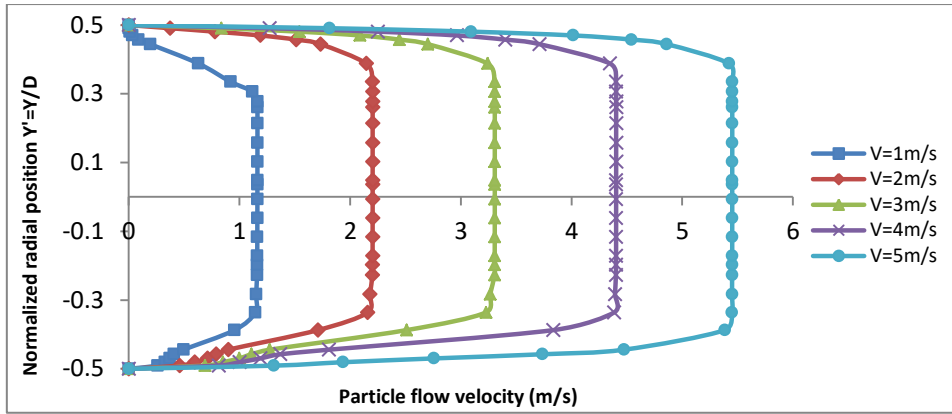


Figure 14. Plots of simulated velocity distribution $v_{sz}(x, y)$ at $C_{vf} = 0.3$

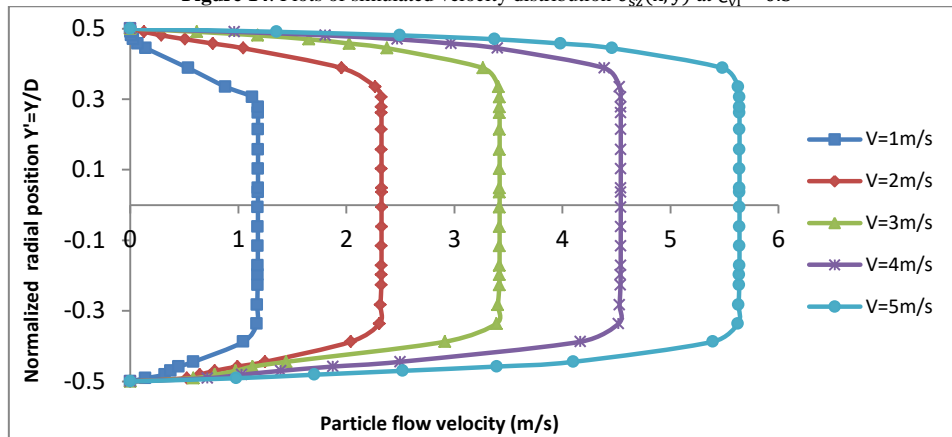


Figure 15. Plots of simulated velocity distribution $v_{sz}(x, y)$ at $C_{vf} = 0.4$

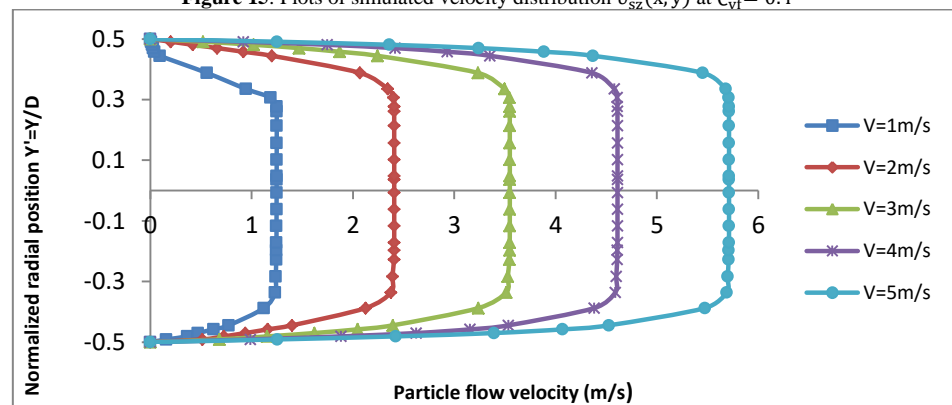


Figure 16. Plots of simulated velocity distribution $v_{sz}(x, y)$ at $C_{vf} = 0.5$

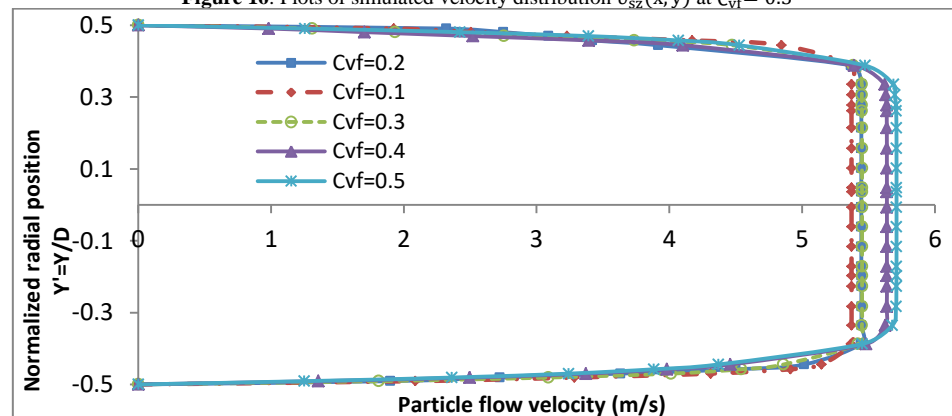


Figure 17. Plot of simulated flow velocity distribution of solid particles at given velocity $V=5\text{m/s}$ and different solid volumetric concentration level.

4.2.1. Effect of solid volumetric concentration on particle flow velocity

From figure 12 to 16 it can be monitored that the solid velocity distribution is parabolic and asymmetrical in the base section of the pipe at low velocities ($V= 1\text{m/s}$, 2m/s) due to larger shear force, as the particles are likely to accumulate at the pipe bottom owing to gravitational effect. However, the solid velocity distribution appears to be more symmetrical as the velocity increases ($V=5\text{ m/s}$). This happens because as velocity and solid volumetric concentration increases there is an increase in Reynolds number (turbulence) which provides a complete blending of fluid and solid particles, the solid particles no longer seem to be accumulated at the base of the pipe, accordingly distribution of particle flow velocity turns into more symmetric.

Figure 17 explains the allocation of particle flow velocity alongside vertical centerline of the pipe cross section from top to bottom at a given velocity viz. 5 m/s at different solid volumetric concentration level. From this figure, a remarkable change in velocity distribution can be observed. For a given velocity, as the volumetric concentration of solid particles raises the velocity distribution becomes more symmetric and the flow velocity increases. This is because of the reason that an increase in solid volumetric concentration causes rise in turbulence and hence rise in particle flow velocity.

4.3. Pressure drop

4.3.1. Effect of solid volumetric concentration on pressure drop

Figure 18 shows the impact of solid volumetric concentration on pressure drop. It is noteworthy that at a constant flow velocity the pressure gradient rises with the surge in solid volumetric concentration. This is because the rise in solid volumetric concentration causes an increase in turbulence of the flow (Reynolds number). Pressure drop is directly proportional to Reynolds number. Hence with the rise in solid volumetric concentration, the pressure drop increases. Moreover, it can be observed that at higher velocities the degree of rise in pressure drop is more.

4.3.2. Effect of turbulence of the flow (Reynolds number) on pressure drop

Figure 19 illustrates the influence of turbulence on pressure gradient at different solid volumetric concentration. It is noteworthy that the pressure drop rises with a raise in turbulence (Reynolds number). Moreover, it also may be scrutinized that as the solid volumetric concentration rises the degree of increase in pressure drop also increases. This is because Reynolds number raises with a rise in solid volumetric concentration.

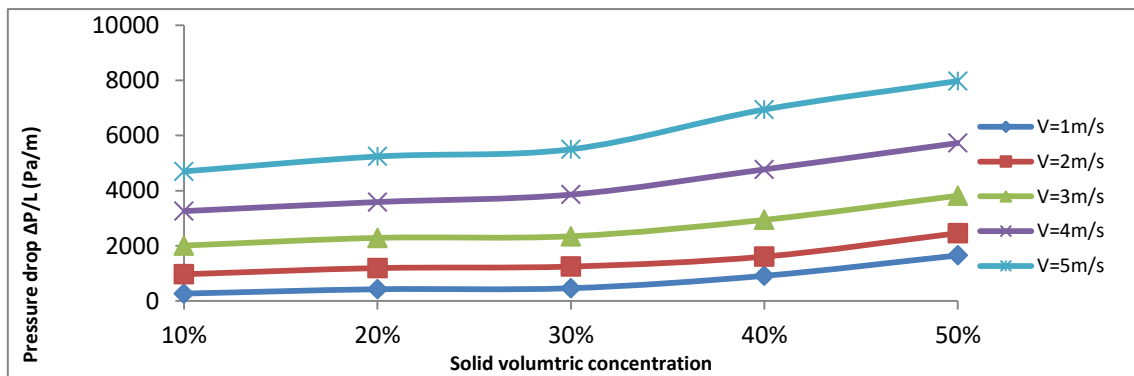


Figure 18. Plots of the effect of solid volumetric concentration on pressure drop at different flow velocity.

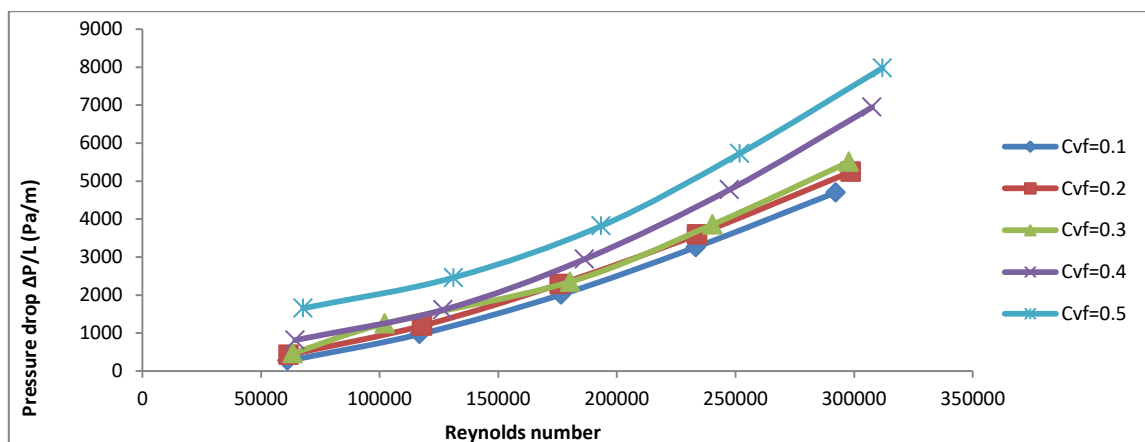


Figure 19. Plots of effect of Reynolds number on pressure drop at different solid volumetric concentration.

4.3.3. Mathematical relationship for pressure drop in terms of turbulence and solid volumetric concentration

The impact of turbulence on pressure gradient is discussed in section 4.3.2. A mathematical correlation is developed for analytical calculation of the influence of turbulence on pressure drop. Initially a polynomial graph was plotted for pressure drop with Reynolds number to predict the functional correlation between them. Then all data variation of pressure drop at different solid volumetric concentrations was plotted against Reynolds number (figure 19). The mathematical model is represented as

$$\frac{\Delta P}{L} = A(Re)^2 + B(Re) + C \tag{8}$$

Where, $\frac{\Delta P}{L}$ is the pressure drop.

Re is Reynolds number.

A, B and C are constants.

Table 3. Values of constants for equation (8) at different solid volumetric concentration

Solid volumetric concentration (C _{vf})	Values of constant A	Values of constant B	Values of constant C
C _{vf} = 0.1	3 × 10 ⁻⁸	0.008	-307
C _{vf} = 0.2	4 × 10 ⁻⁸	0.007	-250
C _{vf} = 0.3	5 × 10 ⁻⁸	0.006	+17.5
C _{vf} = 0.4	6 × 10 ⁻⁸	0.001	+426.4
C _{vf} = 0.5	7 × 10 ⁻⁸	0.000	+950

The effect of solid volumetric concentration on Reynolds number is discussed in the section 4.1.2. A mathematical correlation has been developed for the analytical calculation of the influence of solid volumetric concentration on Reynolds number. Initially an exponential graph has been plotted for the Reynolds number with solid volumetric concentration to establish the functional correlation between them. Then all information variation of Reynolds number at different velocities is plotted against solid volumetric concentration (figure 11). The developed mathematical relationship is represented as:

$$Re = \alpha(\beta e^{nC_{vf}}) \tag{9}$$

Where, Re is the Reynolds number.

C_{vf} is the volumetric concentration of solid particles. α, β and n are constants and their values at different velocities are enlisted in the following table 4

Table 4. Values of constants for equation (9) at different velocities.

Flow velocity	Values of α	Values of β	Values of n
V= 1m/s	59125	1.00	0.246
V= 2m/s	59125	1.857	0.3
V= 3m/s	59125	2.835	0.234
V= 4m/s	59125	3.586	0.193
V= 5m/s	59125	4.383	0.2

Combination of equation 8 and equation 9 yields a generalized form of mathematical correlation for the analytical prediction of pressure drop with different flow velocities at various solid volumetric concentration levels. Combining the two equations we get,

$$\frac{\Delta P}{L} = A(Re)^2 - B(Re) + C \tag{10}$$

Where, $Re = \alpha(\beta e^{nC_{vf}})$

The values of constants are enlisted in table 3 and 4.

Equation 10 confirms that the pressure drop is a function of Reynolds number and solid volumetric concentrations, represented as:

$$\frac{\Delta P}{L} = F_n\{Re, C_{vf}\} \tag{11}$$

4.3.4. Verification of the proposed mathematical relationship

For finding the accuracy and robustness of the developed mathematical correlation a test case is considered where pressure drop is calculated for different flow velocities at solid volumetric concentration of 0.1 to 0.5. This calculated result is then compared with the experimental result of pressure drop available in the literature [26]. Calculated results and the experimental results are enlisted in table 6 to 9. Initially from equation 9 Reynolds number at concentration level 0.1 to 0.5 for flow velocity of 1m/s to 5m/s is calculated. The results are displayed in table 5.

Table 5. Values of Reynolds number at different solid volumetric concentration for various flow velocities.

Velocity	Reynolds number at				
	C _{vf} = 0.1	C _{vf} = 0.2	C _{vf} = 0.3	C _{vf} = 0.4	C _{vf} = 0.5
V= 1m/s	60597	62106	63653	65238	66863
V= 2m/s	113712	117176	120744	124421	128210
V= 3m/s	172458	176541	180721	185000	189380
V= 4m/s	217250	221484	225800	230200	234684
V= 5m/s	265721	271089	276565	282152	287852

Now from the equation 8 pressure drop at different Reynolds number for velocity range of 1m/s to 5m/s at solid volumetric concentration of 0.1 to 0.5 are calculated and the results are displayed in table 6 to 9

Table 6: Comparison of calculated and experimental pressure drop at C_{vf} = 0.1

Reynolds number at C _{vf} = 0.1 for	Calculated Pressure drop (Pa/m)	Experimental pressure drop(Pa/m)	Average error (%)
V=1m/s	60597	287.93	3.19%
V=2m/s	113712	990.6	
V=3m/s	172458	1964.91	
V=4m/s	217250	2846.92	
V=5m/s	265721	3936.99	

Table 7. Comparison of calculated and experimental pressure drop at C_{vf} = 0.2

Reynolds number at C _{vf} = 0.2for	Calculated Pressure drop (Pa/m)	Experimental pressure drop(Pa/m)	Average error (%)
V=1m/s	62106	339.03	4.41%
V=2m/s	117176	1119.44	
V=3m/s	176541	2232.45	
V=4m/s	221484	3262.59	
V=5m/s	271089	4587.19	

Table 8. Comparison of calculated and experimental pressure drop at $C_{vf} = 0.4$

Reynolds number at $C_{vf} = 0.4$ for		Calculated Pressure drop (Pa/m)	Experimental pressure drop (Pa/m) for $C_{vf} = 0.4$	Average error (%)
V=1m/s	65238	746.99	717.181	
V=2m/s	124421	1479.65	1343.56	
V=3m/s	185000	2664.9	2378.46	
V=4m/s	230200	3836.12	3935.34	
V=5m/s	282152	5485.13	5741.88	

Table 9. Comparison of calculated and experimental pressure drop at $C_{vf} = 0.5$

Reynolds number at $C_{vf} = 0.5$ for		Calculated Pressure drop (Pa/m)	Experimental pressure drop (Pa/m) for $C_{vf} = 0.5$	Average error (%)
V=1m/s	66863	1262.94	1593.22	
V=2m/s	128210	2071	2090.4	
V=3m/s	189380	3435	3118.64	
V=4m/s	234684	4766.62	4655.37	
V=5m/s	287852	6691	6621.47	

The results of pressure drop calculated by the proposed mathematical relationship and experimental pressure drop can be plotted as follows:

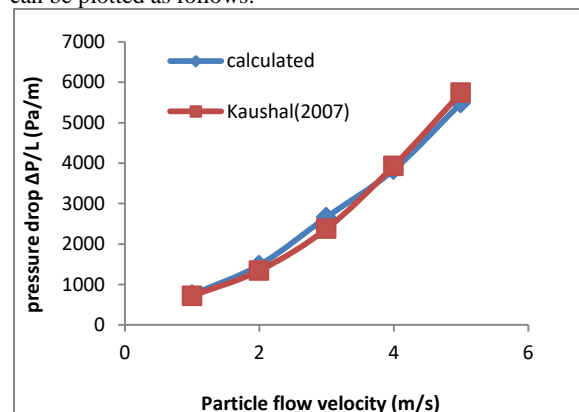


Figure 20. Comparison of calculated and experimental pressure drop at $C_{vf} = 0.1$

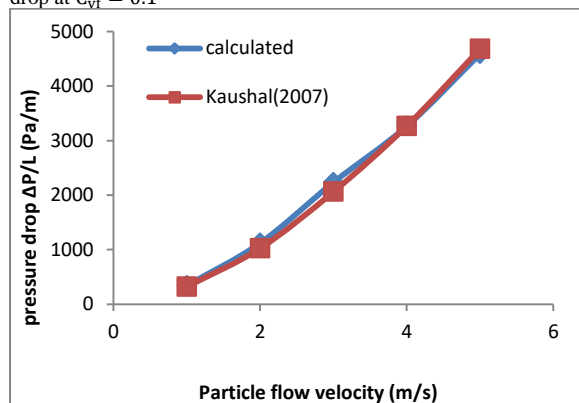


Figure 21. Comparison of calculated and experimental pressure drop at $C_{vf} = 0.2$

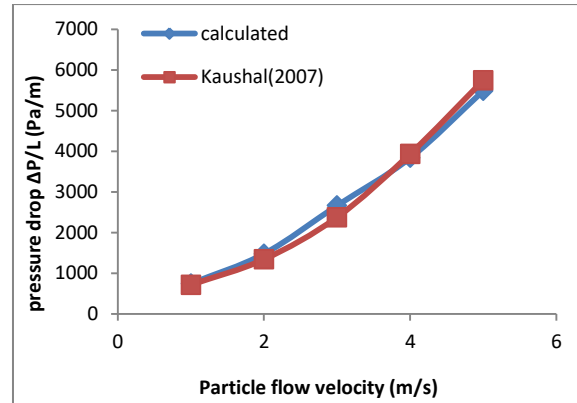


Figure 22. Comparison of calculated and experimental pressure drop at $C_{vf} = 0.4$

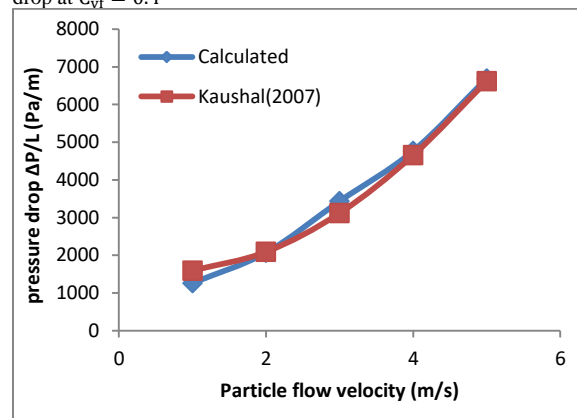


Figure 23. Comparison of calculated and experimental pressure drop at $C_{vf} = 0.5$

From table 6 to 9 and figure 20 to 23 it can be examined that the calculated pressure drop over flow velocity at solid volumetric concentration of 0.1, 0.2, 0.4 and 0.5 show an excellent conformity with the pressure drop data obtained from experiments available in the work of Kaushal and Tomita [26]. It can be concluded that the proposed mathematical relationship shows robustness and accuracy in analytical calculation of the pressure drop. The average percentage error of this correlation is found to be 3.449%.

4.3.5. Validation of the study

The intention of this work is to validate the simulated results

of the pressure drop over flow velocity at various solid volumetric concentrations with the experimental results of pressure drop available in the work of Kaushal and Tomita [19].

Figure 24 shows the impact of particle flow velocity on pressure drop at different solid volumetric concentration. Differential pressure along the length ($\Delta P/L$) is taken on Y-axis and particle flow velocity has been taken on X-axis for plotting the graphs. For comparing the simulated and experimental results, Plot digitizer software is used to extract the coordinates from the experimental results. The proposed investigations can also be carried out for the optimization of performance parameters of other systems like Brayton, Stirling heat engines etc. Further, the optimum value of pressure drops with the application evolutionary algorithms on these pipeline systems is the foremost need of this era [20-37].

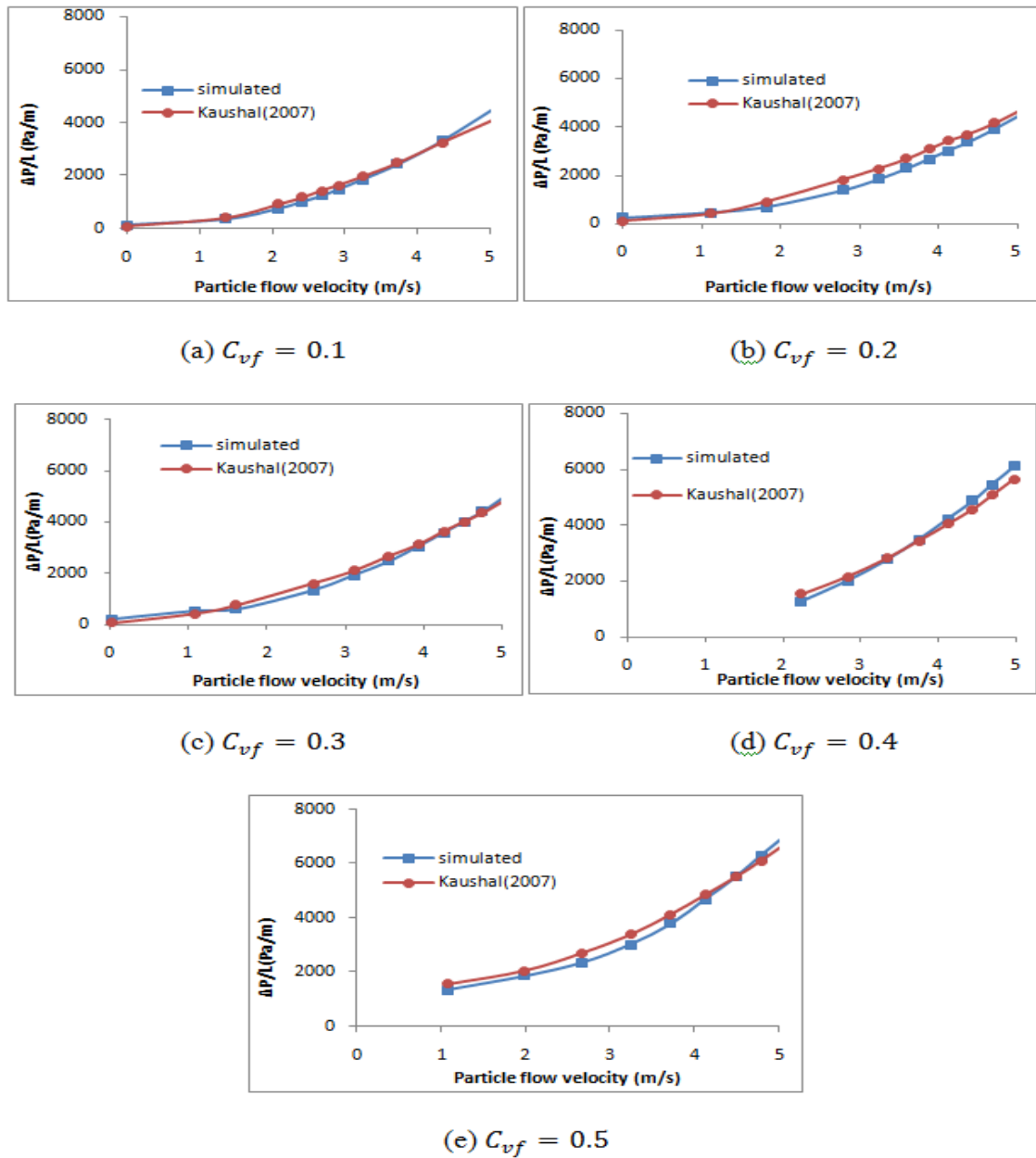


Figure 24. Comparison of simulated and experimental pressure drop over particle flow velocity at different solid volumetric concentration

5. Conclusions

This current study presents a three-dimensional CFD investigation of two phase (glass beads-water) flow through 54.9 mm diameter and 4 m long horizontal pipe for mixture velocity range of 1m/s to 5 m/s and solid volumetric concentration range of 10% to 50% by volume with one particle size 0.125 mm and particle density of 2470 kg/m³. Two phase Eulerian model with granular version and RNG K-ε turbulence model was verified and adopted for the slurry flow. The particles were treated as mono-dispersed. The subsequent conclusions can be drawn based on the current work:

- The solid particles are asymmetrically distributed alongside the vertical plane of cross section of the pipe
- When the particle flow velocity and volumetric concentration is low the higher concentration region is established at the lower half portion of the pipe, where the solid particles seem to be settled at the pipe base.
- For a given concentration as the flow velocity increases the turbulence energy increases which causes a decrease in the asymmetric distribution of the particles and particles tend to suspend rather than settling down at the bottom.
- The contacts of solid particles with the wall of pipe become more vivid with raise in flow velocity.
- Allocation of the solid particles in the horizontal plane turns into more visible with the increase in flow velocity and solid volumetric concentration, concentration distribution along the horizontal plane becomes more symmetric with raise in solid volumetric concentration.
- At a given flow velocity the turbulence of flow enhances with the rise in solid volumetric concentration.
- Velocity distribution is asymmetrical in the lower portion of the pipe along a vertical plane. This is due to the difference in density between the two phase and

because the solid particles are likely to accumulate at the base of the pipe.

- With the rise in flow velocity at a given solid volumetric concentration the velocity distribution becomes more symmetric as the increased turbulence energy provides a proper mixing of the solid particles and fluid at higher velocities.
- At a given velocity as the solid volumetric concentration increases the velocity distribution becomes more asymmetric and velocity increases as there is a rise in turbulence in the flow.
- The effect of solid volumetric concentration on pressure drop is such that pressure drop enhances with the rise in volumetric concentrations.
- The effect of turbulence on pressure drop shows that the pressure drop rises with the rise in turbulence for each level of solid volumetric concentration.

A mathematical correlation among pressure drop, turbulence and solid volumetric concentration is proposed which is developed from the simulated results. Calculated pressure drop using this proposed model illustrated an excellent concurrence with the experimental data. The obtained results of predetermined pressure drop are observed to be in synchronism with the experiment results. Moreover, the comparison of the simulated results proves the practical utility of proposed model, and high designing capability of Eulerian-Eulerian model with RNG $k-\epsilon$ turbulence model.

References

- [1] Seshadri, V., Malhotra, R.C., Sundar, K.S. Concentration and size distribution of solids in a slurry pipeline. In: Proc. 11th Nat. Conference on Fluid mechanics and fluid power, B.H.E.L., Hyderabad 1982.
- [2] Roco MC, Shook CA. Modeling of slurry flow: the effect of particle size. The Canadian Journal of Chemical Engineering. 1983;61(4):494-503.
- [3] Roco MC, Shook CA. Computational method for coal slurry pipelines with heterogeneous size distribution. Powder Technology. 1984;39(2):159-76.
- [4] Gillies RG, Shook CA, Wilson KC. An improved two layer model for horizontal slurry pipeline flow. The Canadian Journal of Chemical Engineering. 1991; 69(1):173-8.
- [5] Gillies RG, Shook CA, Xu J. Modeling heterogeneous slurry flows at high velocities. The Canadian Journal of Chemical Engineering. 2004;82(5):1060-5.
- [6] Doron P, Bamea D. Pressure drop and limit deposit velocity for solid-liquid flow in pipes. Chemical engineering science. 1995;50(10):1595-604.
- [7] Mukhtar A, Singh SN, Seshadri V. Pressure drop in a long radius 90° horizontal bend for the flow of multisized heterogeneous slurries. International journal of multiphase flow. 1995; 21(2):329-34.
- [8] Bellas J, Chaer I, Tassou SA. Heat transfer and pressure drop of ice slurries in plate heat exchangers. Applied Thermal Engineering. 2002; 22(7):721-32.
- [9] Matousek V. Pressure drops and flow patterns in sand-mixture pipes. Experimental thermal and fluid science. 2002; 26(6-7):693-702.
- [10] Scott SH, Abt SR. Hydraulic transport of fine and coarse sediment mixtures in pipelines. Journal of transportation engineering. 2002; 128(1):1-8.
- [11] Lahiri SK, Ghanta KC. Prediction of pressure drop of slurry flow in pipeline by hybrid support vector regression and genetic algorithm model. Chinese Journal of Chemical Engineering. 2008; 16(6):841-8.
- [12] Lahiri SK, Ghanta KC. Regime identification of slurry transport in pipelines: A novel modeling approach using ANN & differential evolution. Chemical Industry and Chemical Engineering Quarterly. 2010;16(4):329-43.
- [13] Chandel S, Singh SN, Seshadri V. Transportation of high concentration coal ash slurries through pipelines. International archive of applied sciences and technology. 2010; 1:1-9.
- [14] Kaushal DR, Kumar A, Tomita Y, Kuchii S, Tsukamoto H. Flow of mono-dispersed particles through horizontal bend. International Journal of Multiphase Flow. 2013; 52:71-91.
- [15] Nabil T, El-Sawaf I, El-Nahas K. Computational fluid dynamics simulation of the solid-liquid slurry flow in a pipeline. InProc. 17th International Water Technologies Conference IWTC17 2013 (Vol. 57).
- [16] Kumar, U., Singh, S. N., & Seshadri, V. experimental investigation on pressure drop characteristics of bi-modal slurry flow in a straight horizontal PIPE, International Journal of Scientific and Engineering Research, 2015; 11(6), 153-158.
- [17] Kumar A. CFD Modeling for Slurry Flow Through Bends and Straight Pipe Line. InCAD/CAM, Robotics and Factories of the Future 2016 (pp. 615-623). Springer, New Delhi.
- [18] Gopaliya MK, Kaushal DR. Modeling of sand-water slurry flow through horizontal pipe using CFD. Journal of Hydrology and Hydromechanics. 2016; 64(3):261-72.
- [19] Kaushal DR, Tomita Y. Experimental investigation for near-wall lift of coarser particles in slurry pipeline using γ -ray densitometer. Powder Technology. 2007; 172(3):177-87.
- [20] Arora R, Arora R. Multiobjective optimization and analytical comparison of single- and 2-stage (series/parallel) thermoelectric heat pumps. International Journal of Energy Research. 2018; 42(4):1760-1778. <https://doi.org/10.1002/er.3988>
- [21] Arora R, Arora R. Multicriteria optimization based comprehensive comparative analyses of single-and two-stage (series/parallel) thermoelectric generators including the influence of Thomson effect. Journal of Renewable and Sustainable Energy. 2018; 10(4): pp.044701.
- [22] Arora R, Kaushik SC, Arora R. Multi-objective and multi-parameter optimization of two-stage thermoelectric generator in electrically series and parallel configurations through NSGA-II. Energy. 2015; 91: 242-254.
- [23] Arora R, Kaushik SC, Arora R. Thermodynamic modeling and multi-objective optimization of two-stage thermoelectric generator in electrically series and parallel configurations. Applied Thermal Engineering. 2016; 25(103): 1312-1323.
- [24] Arora R, Kaushik SC, Kumar R. Multi-objective thermodynamic optimization of solar parabolic dish Stirling heat engine with regenerative losses using NSGA-II and decision making. Applied Solar Energy. 2016; 52(4): 295-304.
- [25] Arora R, Kaushik SC, Kumar R, Arora R. Multi-objective thermo-economic optimization of solar parabolic dish Stirling heat engine with regenerative losses using NSGA-II and decision making. International Journal of Electrical Power & Energy Systems. 2016; 74: 25-35.
- [26] Arora R, Kaushik SC, Kumar Raj, Arora R. Soft computing based multi-objective optimization of Brayton cycle power plant with isothermal heat addition using evolutionary algorithm and decision making. Applied Soft Computing. 2016; 46: 267-283.
- [27] Arora R, Kaushik SC, Kumar R. Multi-objective thermodynamic optimization of solar parabolic dish Stirling heat engine using NSGA-II and decision making. International Journal of Renewable Energy Technology. 2017; 8(1): 64-92.
- [28] Kaushik SC, Kumar R, Arora R. Thermo-economic optimization and parametric study of an irreversible Brayton

- heat engine cycle. *Journal of Thermal Engineering*. 2016; 2(4): 861-870.
- [29] Kumar R., Kaushik SC, Kumar Raj. Performance Analysis of an Irreversible Regenerative Brayton Cycle based on Ecological Optimization Criterion. *International Journal of Thermal and Environment Engineering*. 2015; 9(1): 25-32.
- [30] Kumar R, Kaushik SC, Kumar R. Performance optimization of Brayton heat engine at maximum efficient power using temperature dependent specific heat of working fluid. *Journal of Thermal Engineering*. 2015; 1(2): 345-354.
- [31] Kumar R, Kaushik SC, Kumar R. Power optimization of an Irreversible regenerative Brayton Cycle using isothermal heat addition. *Journal of Thermal Engineering*. 2015; 1(4): 279-286.
- [32] Kumar R, Kaushik SC, Kumar Raj, Hans R. Multi-objective thermodynamic optimization of irreversible regenerative Brayton cycle using evolutionary algorithm and decision making. *Ain Shams Engineering Journal*. 2016; 7(2): 741-753.
- [33] Chiteka K, Arora R, Jain V. CFD prediction of dust deposition and installation parametric optimisation for fouling mitigation in non-tracking solar PVmodules. *International Journal of Ambient Energy*. 2019; pp.1-36 <https://doi.org/10.1080/01430750.2019.1594373>
- [34] Ahmed S, Arora R. Optimization of turning parameters of Aluminum 6351 T6 using Taguchi decision making technique. *International Journal of Data and Network Science*. 2017; 1(2): 27-38.
- [35] Ahmed SU, Arora R. Quality characteristics optimization in CNC end milling of A36 K02600 using Taguchi's approach coupled with artificial neural network and genetic algorithm. *International Journal of System Assurance Engineering and Management*. 2019. pp.1-20
- [36] Maputi ES, Arora R. Design optimization of a three-stage transmission using advanced optimization techniques. *International Journal for Simulation and Multidisciplinary Design Optimization*. 2019; 10: p.A8
- [37] Arora R, Arora R. Performance Characteristics and Thermodynamic Investigations on Single-Stage Thermoelectric Generator and Heat Pump Systems. *Pertanika Journal of Science & Technology*. 2018; 26(4): 1975-19

Exact Thermomechanical Characteristics of a Pressurized Rotating Circular Annulus or a Disc Made of Functionally Graded (FG) Hypothetical and Physical Materials

Vebil Yıldırım

Department of Mechanical Engineering, University of Çukurova, Adana, Turkey

Received 3 Jun. 2018

Abstract

In the present study, thermomechanical characteristics of a functionally graded (FG) uniform traction-free circular annulus are determined analytically under separate and combined centrifugal, steady-state thermal and pressure loads based on the one-dimensional axisymmetric plane-stress assumption. It is assumed that elasticity modulus, density, thermal expansion coefficient and thermal conductivity are all to be continuously changed in the radial direction with different inhomogeneity indexes of a simple power law material grading rule while Poisson's ratio is kept constant. Hypothetically and physically chosen metal-ceramic pairs such as nickel-silicon nitride ($\text{Ni-Si}_3\text{N}_4$), aluminum-aluminum oxide ($\text{Al-Al}_2\text{O}_3$), and stainless steel-zirconium oxide (SUS304-ZrO_2) are included in the parametric studies. Results of conducting separate and combined effects of centrifugal, thermal, and pressure loadings are presented in both tabular and graphical forms in a comparative manner. Those works mostly suggest that the effect of thermal loads may be either negligible compared to inertia forces or may be having higher importance than the inertias. It is also deduced that the thermal characteristics of both individual metal and ceramic are totally different from FGM's thermal traits.

© 2018 Jordan Journal of Mechanical and Industrial Engineering. All rights reserved

Keywords: Thermomechanical, exact solution, functionally graded, circular annulus, rotating disc;

1. Introduction

As commonly known, functionally graded materials (FGM) have exceptional gradually changing mechanical and thermal properties along the preferred directions of the structure [1-2]. Due to this reason, they have gained great attention from many investigators. The significant number of studies have focused on the investigation of the elastic behavior of rotating circular annulus or discs which may be subject to individual or combined effects of mechanical and thermal loads. Investigations related to only a uniform circular annulus or a disc are to be considered in the following literature survey and have been classified by the load types as well.

Under only centrifugal force: By employing a simple-power rule, Horgan and Chan [3] analytically investigated the effects of material inhomogeneity on the response of linearly elastic isotropic solid circular disks or cylinders, rotating at a constant angular velocity about a central axis. Durodola and Attia [4] studied deformation and stressed the FG rotating disks by a direct numerical integration of the governing differential equations as well as the finite element method. Zenkour [5] presented an elastic solution in terms of Whittaker's functions for exponentially graded uniform rotating annular disks. He considered combinations of clamped and free boundary conditions.

Zenkour [6] later considered a rotating functionally graded annular disk with rigid casing. Eraslan and Akış [7] used two variants of a parabolic profile function for disks made of functionally graded materials. Generalizing an available two-dimensional plane-stress solution to a three-dimensional one, Asghari and Ghafoori [8] proposed a semi-analytical three-dimensional elasticity solution for rotating FG hollow and solid disks. Under the assumptions of plane stress, isotropy, and small deformations, Argeso [9] considered analytically both a homogeneous non-uniform rotating disk, and a FG uniform disc. He verified the results by the nonlinear shooting method. Peng and Li [10] employed Fredholm integrals for elastic analysis of arbitrarily graded uniform solid rotating disks. By employing the elasto-perfectly-plastic material model based on Tresca's yield criterion, Nejad et al. [11] presented firstly exact solutions for elasto-plastic deformations and stresses in a simple-power law graded rotating disk. Their work revealed that the plasticity can occur in different regions of the disk. By utilizing Runge-Kutta and shooting methods, Dai and Dai [12] considered the variation of angular speed of a FGM uniform rotating disc. Çallıoğlu et al. [13] investigated elastic-plastic stress analysis with non-work hardening case of power-law graded discs subjected to a constant angular velocity. They verified the results by Ansys.

* Corresponding author e-mail: vebil@cu.edu.tr.

Under only pressure loads: Horgan and Chan [14] showed that the stress response of an inhomogeneous cylinder (or disk) subjected to pressure is significantly different from that of a homogeneous body. Based on the hypergeometric functions, You et al. [15] presented an analytical solution for circular linearly graded uniform disks subject to internal and/or external pressure. Tutuncu and Temel [16] studied axisymmetric displacements and stresses in FG hollow cylinders, disks and spheres subject to only uniform internal pressure by using plane elasticity theory and complementary functions method. Lotfian et al. [17] presented a two-dimensional elasticity solution and a numerical solution using finite element method for elastic analysis of parabolically graded uniform disk subjected to both the internal and external pressures. Nejad et al. [18] extended the previous study by Lotfian et al. [17] to exponentially graded uniform discs that were subjected to internal and external pressures.

Under only thermal loads: Noda [19] has reviewed works conducted in 1980-1991 which covers a wide range of topics from thermo-elastic to thermo-inelastic problems with temperature-dependent properties. Tanigawa [20] also presented a comprehensive review on thermoelastic analysis of FGMs. Bakshi et al. [21] worked on coupled thermoelasticity of functionally graded disks. Tokovy and Ma [22] studied thermal stresses in anisotropic and radially inhomogeneous annular domains. Zenkour [23] carried out a functionally graded annular sandwich disk subjected to only steady-state thermal load. He presented a closed form solution in terms of Whittaker's functions. Peng and Li [24] studied analytically and numerically thermoelastic analysis of either power-law graded annulus or arbitrarily graded annulus. They transformed the governing equation to a Fredholm integral equation. Based on the two-dimensional thermoelastic theories and finite difference method, Arnab et al. [25] investigated numerically thermoelastic fields in a thin circular power-law and exponentially graded $\text{Al}_2\text{O}_3/\text{Al}$ disk with a concentric hole subjected to thermal loads. Under a logarithmic thermal gradients assumption, Aleksandrova [26] investigated analytically elasto-plastic thermal stresses and deformations in a thin annular plate embedded into a rigid container and made of a homogeneous and isotropic material based on the von Mises yield criterion with its associated flow rule.

Under combined pressure and thermal loads: Çallıoğlu et al. [27] analytically studied thermoelastic analysis of power-law graded stress-free annular discs subjected to both pressure and various assumed temperature distributions. Kurşun et al. [28] worked on the elastic stress analysis of power-law graded annular discs subjected to both uniform pressures on the inner surface and a linearly decreasing temperature distribution. Gönczi and Ecsedi [29] solved analytically and numerically governing equation govern the thermo-mechanical behavior of a hollow power-law graded stress-free uniform circular disc under axisymmetric pressure and thermal loads.

Under combined magnetic and thermal loads: Combined effects of magnetic and thermal loads on the elastic behavior of exponentially graded uniform annular discs were considered by Zenkour [30].

Under combined centrifugal and thermal loads: Zenkour [31] also proposed an analytical solution in terms of Whittaker's functions for exponentially graded uniform rotating annular disks under steady-state thermal and centrifugal loads. By dividing the radial domain into some virtual sub-domains, Kordkheili and Naghdabadi [32] presented a semi-analytical solution for a thin axisymmetric uniform rotating traction-free disk made of functionally graded materials with power-law distribution of the volume fraction under centrifugal force and uniform thermal loadings. Go et al. [33] developed a finite element method to demonstrate that a circular power-law graded free-free uniform cutter or grinding disk can be designed with better thermo-elastic characteristics if certain parameters, namely, temperature distribution, angular speed, radial thickness, and outer surface temperature, are controlled properly. A finite element model was developed by Afsar et al. [34] using the variational approach and Ritz method to study the thermoelastic characteristics due to a thermal load and rotation of a thin uniform circular rotating disk having a concentric hole and an exponentially-graded coating at the outer surface. Based on the two-dimensional thermoelastic theories, Afsar and Go [35] conducted a finite element analysis of thermoelastic field in a thin circular exponentially graded $\text{Al}_2\text{O}_3/\text{Al}$ disk subjected to a thermal load and an inertia force due to rotation of the disk. Afsar and Sohag [36] considered thermoelastic characteristics of a thin circular disc having a concentric hole and a functionally graded material (FGM) coating at the outer surface under thermal and centrifugal loads. Gong et al. [37] used a finite volume method for the steady 3-D thermoelastic analysis of the functionally graded uniform rotating discs. They showed that the least square method achieves better performances than the Gaussian method but least square method costs slightly more iteration and computer memory under different mesh types. Yıldırım [38], recently, investigated analytically the thermomechanical attributes of a power-law graded uniform mounted disc with or without rigid casing are under centrifugal and steady-state thermal loads.

In the present study, which is the complementary of Yıldırım's [38] study, a circular annulus or a disc is assumed to be made of both hypothetical and physical metal-ceramic pairs under combined pressure, centrifugal, and thermal loads (Fig. 1). A benchmark example using only hypothetical inhomogeneity indexes for both infinite FGM cylinders [39] and FGM spheres [40] is revisited with a rotating circular annulus or a disc. After this stage, another fresh study is conducted where traction-free annulus is assumed to be made of three types of physical metal-ceramic pairs. Separate and combined effects of mechanical and thermal loads are all investigated.

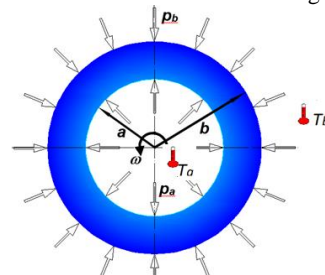


Figure 1. Combined pressure, centrifugal, and thermal loads for a traction-free annulus

2. Thermal Analysis

Let's consider a hollow disc of inside radius a , and outside radius b (Fig. 1). The radial and tangential coordinates are denoted by r , and θ . Let's use the prime symbol to indicate the derivatives with respect to the radial coordinate. For any arbitrary material grading rule of a non-uniform thermal conduction coefficient, $k(r)$, the differential equation which governs the temperature distribution along the radial coordinate in a uniform annulus/disc or a cylinder is defined by [41]

$$\frac{1}{r}(rk(r)T'(r))' = T''(r) + T'(r)\left(\frac{1}{r} + \frac{k'(r)}{k(r)}\right) = 0 \tag{1}$$

If the following power-law grading rule

$$k(r) = k_a \left(\frac{r}{a}\right)^\mu \tag{2}$$

Is employed, Eq. (1) turns into the following

$$T''(r) + \frac{(1+\mu)}{r}T'(r) = 0 \tag{3}$$

Yıldırım [41] solved Eq. (3) under Dirichlet's boundary conditions, $T(a) = T_a$ and $T(b) = T_b$, as follows

$$T(r) = \frac{r^{-\mu}(-b^\mu r^\mu T_b + a^\mu(r^\mu T_a + b^\mu(-T_a + T_b)))}{a^\mu - b^\mu} = \Phi_1 + r^{-\mu}\Phi_2 \tag{4}$$

where

$$\Phi_1 = \frac{a^\mu T_a - b^\mu T_b}{a^\mu - b^\mu}; \quad \Phi_2 = \frac{a^\mu b^\mu (-T_a + T_b)}{a^\mu - b^\mu} \tag{5}$$

Solution of Eq. (3) for isotropic and homogeneous materials, $\mu = 0$, under the same boundary conditions takes the following form [41]

$$T(r) = T_a + \frac{(T_b - T_a)}{\ln(\frac{b}{a})} \ln\left(\frac{r}{a}\right) = \ln r \Psi_2 + \Psi_1$$

$$\Psi_1 = \frac{\ln a T_b - T_a \ln b}{\ln(\frac{a}{b})}; \quad \Psi_2 = \frac{T_a - T_b}{\ln(\frac{a}{b})} \tag{6}$$

3. Derivation of Governing Equation

Under axisymmetric plane-stress assumptions, the strain-displacement relations for cylinders are given by

$$\epsilon_r(r) = u_r'(r); \quad \epsilon_\theta(r) = \frac{u_r(r)}{r} \tag{7}$$

where u_r is the radial displacement, ϵ_r is the unit radial strain, ϵ_θ is the unit tangential strain. Thermoelastic stress-strain constitutive relations for a FGM may be given in the form of [38]

$$\sigma_r(r) = C_{11}(r)\epsilon_r + C_{12}(r)\epsilon_\theta - (C_{11}(r) + C_{12}(r))\alpha(r)T(r)$$

$$\sigma_\theta(r) = C_{12}(r)\epsilon_r + C_{11}(r)\epsilon_\theta - (C_{11}(r) + C_{12}(r))\alpha(r)T(r) \tag{8}$$

where $\sigma_r(r)$ is the radial stress, $\sigma_\theta(r)$ is the hoop stress, $\alpha(r)$ is the coefficient of thermal expansion, and

$$C_{11}(r) = \frac{1}{1-\nu^2}E(r); \quad C_{12}(r) = \frac{\nu}{1-\nu^2}E(r) = \nu C_{11}(r) \tag{9}$$

where $E(r)$ is Young's modulus and ν is Poisson's ratio. The arithmetic mean of Poisson's ratios of ceramic

and metal is used in the present numerical calculations. Substituting Eq. (7) into Eq. (8), Hooke's law, then, takes the following form of

$$\sigma_r(r) = C_{11}(r) \left(u_r'(r) + \nu \frac{u_r(r)}{r} \right) - (1+\nu)C_{11}(r)\alpha(r)T(r) \tag{10}$$

$$\sigma_\theta(r) = C_{11}(r) \left(\nu u_r'(r) + \frac{u_r(r)}{r} \right) - (1+\nu)C_{11}(r)\alpha(r)T(r)$$

The equilibrium equation in the radial coordinate of an annulus/disc rotating at a constant circular velocity, ω , is

$$(r\sigma_r(r))' - \sigma_\theta = \sigma_r'(r) + \frac{\sigma_r(r) - \sigma_\theta(r)}{r} = -\rho(r)\omega^2 r \tag{11}$$

where $\rho(r)$ is the material density. After substitution of Eq. (10) into Eq. (11), Navier equation in general form is obtained.

$$u_r''(r) + \left(\frac{1}{r} + \frac{C_{11}'(r)}{C_{11}(r)}\right)u_r'(r) + \left(-\frac{1}{r^2} + \frac{\nu C_{11}'(r)}{r C_{11}(r)}\right)u_r(r) = -\frac{\rho(r)\omega^2 r}{C_{11}(r)} + (1+\nu)\alpha(r)T'(r) + \left(\frac{C_{11}'(r)}{C_{11}(r)}\alpha(r) + \alpha'(r)\right)(1+\nu)T(r) \tag{12}$$

If the following material gradients are used in Eq. (12),

$$E(r) = E_a \left(\frac{r}{a}\right)^\beta; \quad \rho(r) = \rho_a \left(\frac{r}{a}\right)^q; \quad \alpha(r) = \alpha_a \left(\frac{r}{a}\right)^n \tag{13}$$

then Navier equation for thermomechanical analysis of a power-law graded annulus/disc is obtained as follows [38]

$$\frac{(-1+\beta\nu)}{r^2}u_r(r) + \frac{(1+\beta)}{r}u_r'(r) + u_r''(r) = \frac{a^{-q+\beta}r^{1+q-\beta}(1-\nu^2)\rho_a\omega^2}{E_a} + a^{-n}r^{-1+n-\mu}\alpha_a(1+\nu)(r^\mu(n+\beta)\Phi_1 + (n+\beta-\mu)\Phi_2) \tag{14}$$

where inhomogeneity indexes are denoted by β, q, μ and n . By using the followings,

$$\Delta_1 = a^{-n}\alpha_a(n+\beta)(1+\nu)\Phi_1$$

$$\Delta_2 = a^{-n}\alpha_a(n+\beta-\mu)(1+\nu)\Phi_2 \tag{15}$$

Navier equation may be rewritten in a more compact form as

$$\frac{(-1+\beta\nu)}{r^2}u_r(r) + \frac{(1+\beta)}{r}u_r'(r) + u_r''(r) = \frac{a^{-q+\beta}r^{1+q-\beta}(1-\nu^2)\rho_a\omega^2}{E_a} + r^{-1+n-\mu}(r^\mu\Delta_1 + \Delta_2) \tag{16}$$

This is a second order non-homogeneous Euler-Cauchy differential equation with constant coefficients [38]. It is possible to find a closed form general solution (homogeneous+particular) to this equation. After getting the solution, combined radial and hoop stresses may be determined based on the superposition principle for linearly elastic materials as follows.

$$\sigma_{total} = \sigma_{thermal} + \sigma_{rotation} + \sigma_{pressure} \tag{17}$$

Equivalent stress at any surface in the radial direction is computed with the help of von-Mises failure criterion as follows

$$\sigma_{eq}(r) = \sqrt{\sigma_r^2 - \sigma_r\sigma_\theta + \sigma_\theta^2} \quad (18)$$

The general solutions of Eq. (16), obtained with the help of Euler-Cauchy technique, are given directly in the following sections for each separate mechanical and thermal load.

3.1. Elastic Fields under both Internal and External Pressures

Homogeneous solution of the Navier equation in Eq. (16)

$$\frac{(-1 + \beta\nu)}{r^2} u_r(r) + \frac{(1 + \beta)}{r} u_r'(r) + u_r''(r) = 0 \quad (19)$$

under boundary conditions, $\sigma_r(a) = -p_a$ and $\sigma_r(b) = -p_b$, renders the elastic field due to both internal and external pressures, p_a and p_b , as follows

$$u_r(r) = \frac{2(\nu^2 - 1)p_a a^{\frac{1}{2}(\beta + \xi + 2)} r^{\frac{1}{2}(-\beta - \xi)} (b^\xi (\beta - 2\nu - \xi) - r^\xi (\beta - 2\nu + \xi))}{E_a (a^\xi - b^\xi) (\beta - 2\nu - \xi) (\beta - 2\nu + \xi)} + \frac{2(\nu^2 - 1)p_b a^\beta b^{\frac{1}{2}(-\beta + \xi + 2)} r^{\frac{1}{2}(-\beta - \xi)} (a^\xi (\beta - 2\nu - \xi) - r^\xi (\beta - 2\nu + \xi))}{E_a (a^\xi - b^\xi) (\beta - 2\nu + \xi) (-\beta + 2\nu + \xi)} \quad (22a)$$

$$\sigma_r(r) = \frac{p_a a^{\frac{1}{2}(-\beta + \xi + 2)} (b^\xi - r^\xi) r^{\frac{1}{2}(\beta - \xi - 2)}}{a^\xi - b^\xi} + \frac{p_b (a^\xi - r^\xi) b^{\frac{1}{2}(-\beta + \xi + 2)} r^{\frac{1}{2}(\beta - \xi - 2)}}{b^\xi - a^\xi} \quad (22b)$$

$$\sigma_\theta(r) = \frac{1}{(a^\xi - b^\xi) (\beta - 2\nu - \xi) (\beta - 2\nu + \xi)} \left(p_a a^{\frac{1}{2}(-\beta + \xi + 2)} r^{\frac{1}{2}(\beta - \xi - 2)} (b^\xi (\beta - 2\nu - \xi) (\nu(\beta + \xi) - 2) + r^\xi (\beta - 2\nu + \xi) (-\beta\nu + \nu\xi + 2)) \right) + \frac{1}{(a^\xi - b^\xi) (\beta - 2\nu + \xi) (-\beta + 2\nu + \xi)} \left(p_b b^{\frac{1}{2}(-\beta + \xi + 2)} r^{\frac{1}{2}(\beta - \xi - 2)} (a^\xi (\beta - 2\nu - \xi) (\nu(\beta + \xi) - 2) + r^\xi (\beta - 2\nu + \xi) (-\beta\nu + \nu\xi + 2)) \right) \quad (22c)$$

For a disk made of an isotropic and homogeneous material, solution of the following under boundary conditions, $\sigma_r(a) = -p_a$ and $\sigma_r(b) = -p_b$,

$$u_r''(r) + \frac{1}{r} u_r'(r) - \frac{1}{r^2} u_r(r) = 0 \quad (23)$$

gives the elastic field due to both internal and external pressures as follows [42]

$$u_r(r) = -\frac{a^2 p_a (b^2 (\nu + 1) - (\nu - 1) r^2)}{Er (a^2 - b^2)} + \frac{b^2 p_b (a^2 (\nu + 1) - (\nu - 1) r^2)}{Er (a^2 - b^2)}$$

$$\sigma_r(r) = \frac{a^2 p_a (b^2 - r^2)}{r^2 (a^2 - b^2)} + \frac{b^2 (a - r) (a + r) p_b}{r^2 (b^2 - a^2)} \quad (24)$$

$$\sigma_\theta(r) = -\frac{a^2 p_a (b^2 + r^2)}{r^2 (a^2 - b^2)} + \frac{b^2 (a^2 + r^2) p_b}{r^2 (a^2 - b^2)}$$

Explicit forms of Eq. (20) are as follows

$$u_r(r) = r^{\frac{1}{2}(-\beta - \xi)} (A_1 + A_2 r^\xi) \quad (20)$$

$$\sigma_r(r) = -\frac{1}{2} C_{11}(r) r^{\frac{1}{2}(-2 - \beta - \xi)} \left(A_2 r^\xi (\beta - 2\nu - \xi) + A_1 (\beta - 2\nu + \xi) \right)$$

$$\sigma_\theta(r) = \frac{1}{2} r^{\frac{1}{2}(-2 - \beta - \xi)} C_{11}(r) \left(A_2 r^\xi (2 - \beta\nu + \nu\xi) - A_1 (-2 + \nu(\beta + \xi)) \right)$$

Where

$$\xi = \sqrt{4 + \beta^2 - 4\beta\nu} \quad (21a)$$

$$A_1 = -\frac{2(\nu^2 - 1) a^{\frac{\beta + \xi}{2}} b^{\frac{\xi - \beta}{2}} \left(b p_b a^{\frac{\beta + \xi}{2}} - a p_a b^{\frac{\beta + \xi}{2}} \right)}{E_a (a^\xi - b^\xi) (\beta - 2\nu + \xi)} \quad (21b)$$

$$A_2 = \frac{b^{-\beta/2} \left(2(\nu^2 - 1) p_b a^\beta b^{\frac{\xi}{2} + 1} - 2(\nu^2 - 1) p_a b^{\beta/2} a^{\frac{1}{2}(\beta + \xi + 2)} \right)}{E_a (a^\xi - b^\xi) (\beta - 2\nu - \xi)} \quad (21c)$$

3.2. Elastic Fields under Rotation at a Constant Angular Speed

Homogeneous and particular solutions of the Navier equation given in Eq. (16)

$$\frac{(-1 + \beta v)}{r^2} u_r(r) + \frac{(1 + \beta)}{r} u_r'(r) + u_r''(r) = - \frac{a^{-q+\beta} r^{1+q-\beta} (1 - v^2) \rho_a \omega^2}{E_a} \quad (25)$$

give the elastic fields in terms of integration constants due to the rotation about an axis passing through the center of annulus as

$$u_r(r) = r^{-\beta} \left(r^{\frac{\beta-\xi}{2}} (B_1 + B_2 r^\xi) + r^{3+q} \Omega \right)$$

$$\sigma_r(r) = \frac{1}{2} r^{-1-\beta-\frac{\xi}{2}} C_{11}(r) \left(r^{\beta/2} (-B_1(\beta - 2v + \xi) + B_2 r^\xi (-\beta + 2v + \xi)) + 2r^{3+q+\frac{\xi}{2}} (3 + q - \beta + v) \Omega \right) \quad (26)$$

$$\sigma_\theta(r) = \frac{1}{2} r^{-1-\beta-\frac{\xi}{2}} C_{11}(r) \left(-r^{\beta/2} (-B_2 r^\xi (2 - \beta v + v\xi) + B_1 (-2 + v(\beta + \xi))) + 2r^{3+q+\frac{\xi}{2}} (1 + (3 + q - \beta)v) \Omega \right)$$

where

$$\xi = \sqrt{4 + \beta^2 - 4\beta v}$$

$$\Omega = \frac{a^{-q+\beta} (-1 + v^2) \rho_a \omega^2}{E_a (8 + q(6 + q - \beta) - 3\beta + \beta v)} \quad (27)$$

Integration constants in Eq. (26) are determined under free-free boundary conditions, $\sigma_r(a) = 0$ and $\sigma_r(b) = 0$, as

$$B_1 = \frac{2\Omega a^{\frac{\xi-\beta}{2}} b^{\frac{\xi-\beta}{2}} (\beta - v - q - 3) \left(a^{q+3} b^{\frac{\beta+\xi}{2}} - b^{q+3} a^{\frac{\beta+\xi}{2}} \right)}{(a^\xi - b^\xi)(\beta - 2v + \xi)}$$

$$B_2 = \frac{2\Omega a^{-\beta/2} b^{-\beta/2} (-\beta + v + q + 3) \left(b^{\beta/2} a^{\frac{\xi}{2}+q+3} - a^{\beta/2} b^{\frac{\xi}{2}+q+3} \right)}{(a^\xi - b^\xi)(\beta - 2v - \xi)} \quad (28)$$

If the disk material is homogeneous and isotropic, then, Eq. (25) turns into the following

$$u_r''(r) + \frac{1}{r} u_r'(r) - \frac{1}{r^2} u_r(r) = - \frac{\rho \omega^2 r}{C_{11}} = - \frac{r(1 - v^2) \rho \omega^2}{E} \quad (29)$$

Solution of this equation given above under the free-free boundary conditions is [43]

$$u_r(r) = \frac{1}{8Er} \left(\rho \omega^2 (a^2(v + 3)(b^2(v + 1) - (v - 1)r^2) - (v - 1)r^2(b^2(v + 3) - (v + 1)r^2)) \right)$$

$$\sigma_r(r) = \frac{(v + 3)\rho \omega^2 (a - r)(a + r)(r^2 - b^2)}{8r^2} \quad (30)$$

$$\sigma_\theta(r) = \frac{\rho \omega^2 (a^2(v + 3)(b^2 + r^2) + r^2(b^2(v + 3) - (3v + 1)r^2))}{8r^2}$$

3.3. Elastic Fields under Thermal Loads

Homogeneous and particular solutions of Navier equation given in Eq. (16) together with Dirichlet's boundary conditions, $T(a) = T_a$ and $T(b) = T_b$,

$$\frac{(-1 + \beta v)}{r^2} u_r(r) + \frac{(1 + \beta)}{r} u_r'(r) + u_r''(r) = r^{-1+n-\mu} (r^\mu \Delta_1 + \Delta_2) \quad (31)$$

give the elastic field as

$$u_r(r) = \Delta_3 \left(r^{1+n-\mu} \Delta_4 + r^{1+n} \Delta_1 \Delta_5 + C_1 r^{\frac{1}{2}(-\beta-\xi)} \Delta_5 \Delta_6 + C_2 r^{\frac{1}{2}(-\beta+\xi)} \Delta_5 \Delta_6 \right)$$

$$\sigma_r(r) = C_{11}(r) r^n \Delta_3 (\Delta_1 \Delta_5 (1 + n + v) + r^{-\mu} \Delta_4 (1 + n - \mu + v)) + \frac{1}{2} C_{11}(r) r^{\frac{1}{2}(-2-\beta-\xi)} \Delta_3 \Delta_5 \Delta_6 (-C_1(\beta - 2v + \xi) + C_2 r^\xi (-\beta + 2v + \xi)) + \frac{a^{-n-\beta} E_a r^{n+\beta-\mu} \alpha_a (r^\mu \Phi_1 + \Phi_2)}{-1 + v} \quad (32)$$

$$\sigma_\theta(r) = C_{11}(r) r^n \Delta_3 (\Delta_1 \Delta_5 (1 + v + nv) + r^{-\mu} (\Delta_4 + \Delta_4 (1 + n - \mu)v)) + \frac{1}{2} C_{11}(r) r^{\frac{1}{2}(-2-\beta-\xi)} \Delta_3 \Delta_5 \Delta_6 (C_2 r^\xi (2 - \beta v + v\xi) - C_1 (-2 + v(\beta + \xi))) + \frac{a^{-n-\beta} E_a r^{n+\beta-\mu} \alpha_a (r^\mu \Phi_1 + \Phi_2)}{-1 + v}$$

where auxiliary constants are

$$\xi = \sqrt{4 + \beta^2 - 4\beta v} \quad (33a)$$

$$\Delta_3 = 16((-2 - 2n - \beta + \xi)(2 + 2n + \beta + \xi)(2 + 2n + \beta - 2\mu + \xi)(-2 - 2n - \beta + 2\mu + \xi))^{-1} \quad (33b)$$

$$\Delta_4 = \Delta_2(\beta + n(2 + n + \beta) + \beta v)$$

$$\Delta_5 = n^2 + n(2 + \beta - 2\mu) + (-2 + \mu)\mu + \beta(1 - \mu + v)$$

$$\Delta_6 = \beta + n(2 + n + \beta) + \beta v$$

Integration constants in the solution of Eq. (32) are determined for free-free boundary conditions as

$$\begin{aligned}
 C_1 &= \frac{2b^{\frac{1}{2}(\xi-2\mu)} a^{\frac{1}{2}(\xi-2(\mu+n))}}{\Delta_3 \Delta_5 \Delta_6 (a^\xi - b^\xi) (\beta - 2\nu + \xi)} \left(a^{\mu+\frac{\xi}{2}} b^{\frac{\beta}{2}+n+1} \left(\Delta_3 a^n (\Delta_1 \Delta_5 b^\mu (\nu + n + 1) + \Delta_4 (-\mu + \nu + n + 1)) \right. \right. \\
 &\quad \left. \left. - \alpha_a (\nu + 1) (\Phi_1 b^\mu + \Phi_2) \right) \right. \\
 &\quad \left. + a^{\frac{\beta}{2}+n+1} b^{\mu+\frac{\xi}{2}} (-\Delta_1 \Delta_3 \Delta_5 (\nu + n + 1) a^{\mu+n} + \alpha_a (\nu + 1) \Phi_1 a^\mu \right. \\
 &\quad \left. - \Delta_3 \Delta_4 a^n (-\mu + \nu + n + 1) + \alpha_a (\nu + 1) \Phi_2) \right) \\
 C_2 &= -\frac{1}{\Delta_3 \Delta_5 \Delta_6 (a^\xi - b^\xi) (-\beta + 2\nu + \xi)} 2b^{-\mu} a^{-\mu-n} \left(-\alpha_a (\nu + 1) \Phi_1 b^\mu a^{\frac{\beta}{2}+\mu+n+\frac{\xi}{2}+1} \right. \\
 &\quad \left. - \alpha_a (\nu + 1) \Phi_2 b^\mu a^{\frac{1}{2}(\beta+2n+\xi+2)} + \Delta_1 \Delta_3 \Delta_5 b^\mu (\nu + n + 1) a^{\frac{1}{2}(\beta+2\mu+4n+\xi+2)} \right. \\
 &\quad \left. + \Delta_3 \Delta_4 b^\mu (-\mu + \nu + n + 1) a^{\frac{1}{2}(\beta+4n+\xi+2)} \right. \\
 &\quad \left. - \Delta_3 a^{\mu+n} b^{\frac{1}{2}(\beta+2n+\xi+2)} (\Delta_1 \Delta_5 b^\mu (\nu + n + 1) + \Delta_4 (-\mu + \nu + n + 1)) \right. \\
 &\quad \left. + \alpha_a (\nu + 1) a^\mu (\Phi_1 b^\mu + \Phi_2) b^{\frac{1}{2}(\beta+2n+\xi+2)} \right)
 \end{aligned} \tag{34}$$

If the disk is made of an isotropic and homogeneous material, Eq. (31) turns into [42]

$$u_r''(r) + \frac{1}{r} u_r'(r) - \frac{1}{r^2} u_r(r) = (1 + \nu) \alpha T'(r) = (1 + \nu) \frac{\alpha}{r} \left(\frac{T_a - T_b}{\ln\left(\frac{a}{b}\right)} \right) = (1 + \nu) \frac{\alpha}{r} \Psi_2 = \frac{\Delta}{r} \tag{35}$$

Solution of Eq. (35) under free-free boundary condition is

$$\begin{aligned}
 u_r(r) &= \frac{1}{2(\nu - 1)(\nu + 1)r^2(a - b)(a + b)} \{ a^2(\nu + 1) \ln a (\Delta - 2\alpha \Psi_2) (b^2(\nu + 1) - (\nu - 1)r^2) \\
 &\quad - b^2(\nu + 1) \ln b (a^2(\nu + 1) - (\nu - 1)r^2) (\Delta - 2\alpha \Psi_2) \\
 &\quad + (\nu - 1)r^2(a - b)(a + b) (2\alpha(\nu + 1)\Psi_1 - \Delta + \Delta(\nu + 1) \ln r) \} \\
 \sigma_r(r) &= -\frac{E(\Delta - 2\alpha \Psi_2)(b^2(r^2 - a^2) \ln b + a^2 \ln a (b - r)(b + r) + r^2(a - b)(a + b) \ln r)}{2(\nu - 1)r^2(a - b)(a + b)} \tag{36}
 \end{aligned}$$

$$\begin{aligned}
 \sigma_\theta(r) &= \frac{1}{2(\nu - 1)(\nu + 1)r^2(a - b)(a + b)} \left(E((\nu + 1)(\Delta - 2\alpha \Psi_2)(a^2 \ln a (b^2 + r^2) - b^2(a^2 + r^2) \ln b + r^2(b^2 - a^2) \ln r) \right. \\
 &\quad \left. - \Delta(\nu - 1)r^2(a - b)(a + b)) \right)
 \end{aligned}$$

4. Revisited the Benchmark Example

Jabbari et al. [39] and Eslami et al. [40] used the following material and geometrical properties to study the thermo-mechanical analysis of both traction-free cylinders and spheres which are subjected to both internal pressure and surface temperature differences.

$$\begin{aligned}
 a &= 1.0m; b = 1.2m; \nu = 0.3; E_a = 200 \text{ GPa}; \\
 \rho_a &= 7800 \frac{\text{kg}}{\text{m}^3}; \alpha_a = 1.2 \cdot 10^{-6} \frac{1}{^\circ\text{C}}; k_a = 15.379 \frac{\text{W}}{\text{m}^\circ\text{C}}; \\
 p_a &= 50 \text{ MPa}; p_b = 0; T_a = 10^\circ\text{C}; T_b = 0^\circ\text{C}
 \end{aligned}$$

In the present study the same example is to be extended to a hollow disk or annulus under free-free boundary conditions. In the benchmark examples, the homogeneity indexes are to be all the same, $\beta = n = \mu = q$, and they are determined hypothetically. Jabbari et al. [39] and Eslami et al. [40] did not consider the centrifugal forces. The constant angular velocity is assumed to be $\omega = 100 \text{ rad/s}$, and the hypothetically chosen values of the inhomogeneity indexes are to be $-3 \leq \beta \leq 3$ in the present example. The results are presented in Figs. 2-3 and Table 1. It may be noted that, for the disks made of

isotropic and homogeneous materials, $\beta = n = \mu = q = 0$, Eqs. (24), (30), and (36) are used in all examples instead other closed-form expressions derived from FGM discs. This allows an auto-control mechanism for the present computations.

Variations of the dimensionless elastic fields with the inhomogeneity index under individual and combined loads are illustrated in Fig. 2. Variation of the dimensionless equivalent stress with the inhomogeneity index under combined loads is also shown in Fig. 3. If the present graphs for combined thermal and pressure loads in Figs. 2-3 are compared with the benchmark graphs, it is seen that the present graphs are very close to the graphs for cylinders [39]. Fig. 2 and 3 suggest

- The rotation effects seem to be much important than the thermal effects. The thermal effects may be negligible for this example.
- As r/a increases the dimensionless radial displacement increases under individual thermal loads for all inhomogeneity indexes. Maximum combined radial displacements are observed at the inner surface.

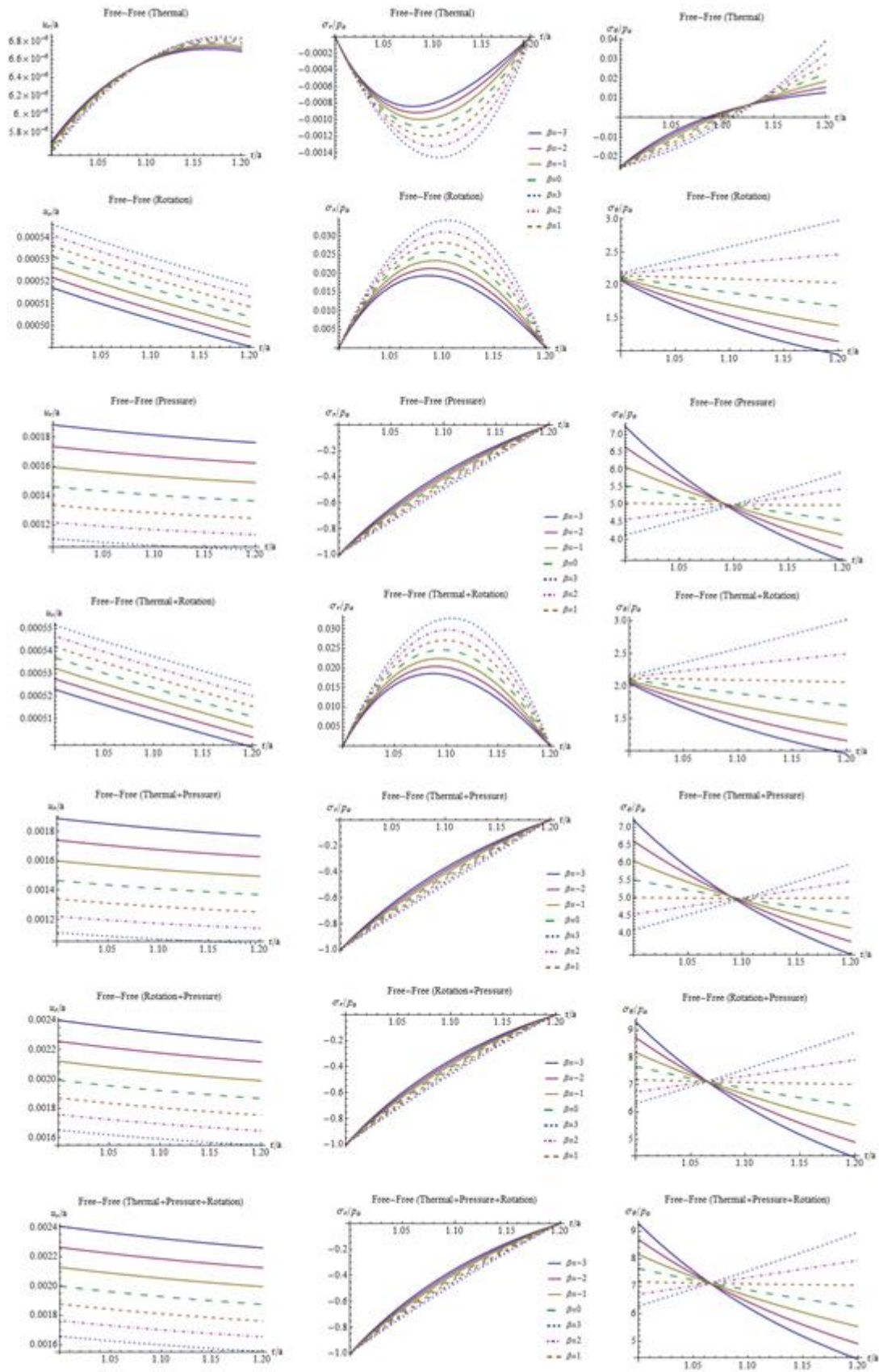


Figure 2. Variation of the elastic fields in an annulus with the inhomogeneity index

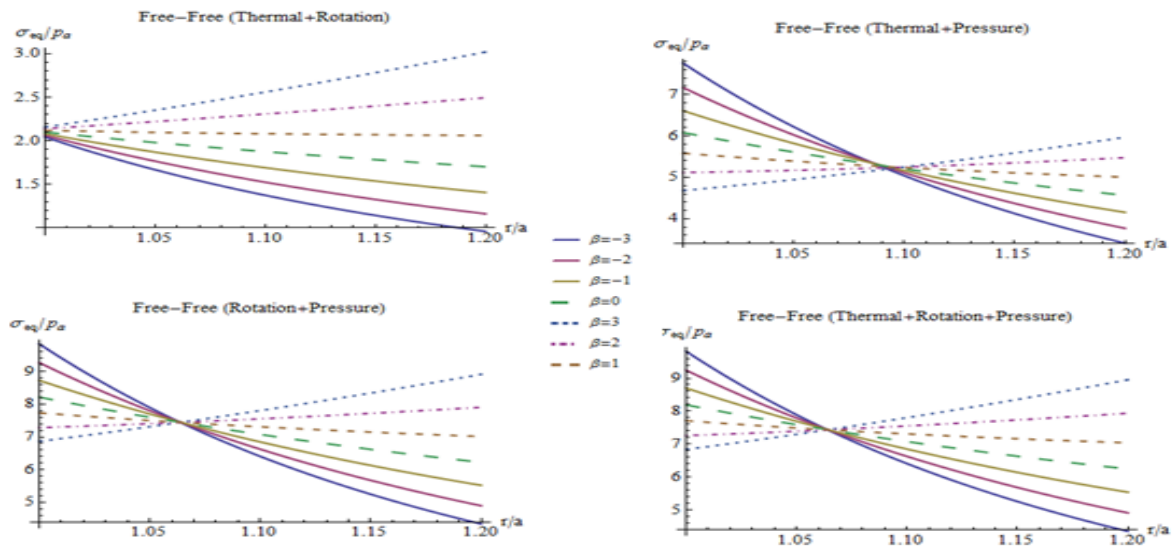


Figure 3. Variation of the dimensionless equivalent stress with the inhomogeneity index under combined loads for free-free boundary conditions.

Table 1. Variation of the dimensionless elastic fields with the inhomogeneity indexes

r/a	u_r/a		σ_r/p_a		σ_θ/p_a	
	$\beta = -2$	$\beta = 2$	$\beta = -2$	$\beta = 2$	$\beta = -2$	$\beta = 2$
Thermal						
1.	0.00000568	0.0000056	0.	0.	-0.0252823	-0.0256429
1.04	0.00000615	0.0000061	-0.0006996	-0.0008291	-0.0117571	-0.0172315
1.08	0.00000647	0.0000065	-0.0009132	-0.0012579	-0.0016646	-0.0073190
1.12	0.00000666	0.0000067	-0.0007991	-0.0012733	0.00585425	0.00421912
1.16	0.00000674	0.0000068	-0.0004687	-0.0008510	0.011432	0.017512
1.2	0.00000671	0.0000068	0.	0.	0.0155387	0.032693
Centrifugal						
1.	0.00052199	0.0005413	0.	0.	2.08796	2.16504
1.04	0.00051597	0.0005350	0.0153977	0.0195631	1.83938	2.23156
1.08	0.00051035	0.0005292	0.0211395	0.0296796	1.62687	2.29506
1.12	0.00050504	0.0005237	0.0194235	0.0300443	1.44374	2.35514
1.16	0.00049994	0.0005184	0.0119405	0.0202913	1.28474	2.4114
1.2	0.00049496	0.0005132	0.	0.	1.14574	2.46342
Pressure						
1.	0.00173548	0.0012174	-1.	-1.	6.64192	4.56964
1.04	0.00170714	0.0011954	-0.721683	-0.782553	5.85405	4.73815
1.08	0.00168181	0.0011765	-0.490729	-0.574911	5.19307	4.90994
1.12	0.00165928	0.0011602	-0.29798	-0.375911	4.63479	5.08474
1.16	0.00163939	0.0011461	-0.136284	-0.184559	4.16027	5.26232
1.2	0.00162198	0.0011339	0.	0.	3.75458	5.4425
Combined (thermal+pressure)						
1.	0.00174116	0.001223	-1.	-1.	6.61664	4.54399
1.04	0.00171329	0.0012015	-0.722383	-0.783383	5.84229	4.72092
1.08	0.00168828	0.0011829	-0.491642	-0.576169	5.1914	4.90262
1.12	0.00166594	0.0011669	-0.29878	-0.377184	4.64064	5.08896
1.16	0.00164613	0.0011529	-0.136752	-0.185419	4.1717	5.27984
1.2	0.00162869	0.0011407	0.	0.	3.77012	5.4752
Combined (thermal+centrifugal)						
1.	0.00052767	0.0005469	0.	0.	2.06267	2.1394
1.04	0.00052212	0.0005411	0.0146981	0.018734	1.82763	2.21432
1.08	0.00051682	0.0005357	0.0202264	0.0284217	1.62521	2.28774
1.12	0.0005117	0.0005304	0.0186244	0.028771	1.44959	2.35936
1.16	0.00050668	0.0005252	0.0114718	0.0194313	1.29618	2.42891
1.2	0.00050167	0.0005200	0.	0.	1.16128	2.49612
Combined (centrifugal+pressure)						
1.	0.00225747	0.0017587	-1.	-1.	8.72988	6.73468
1.04	0.0022231	0.0017304	-0.706286	-0.76299	7.69343	6.96971
1.08	0.00219216	0.0017057	-0.469589	-0.545232	6.81994	7.20499
1.12	0.00216432	0.0016839	-0.278557	-0.345867	6.07852	7.43988
1.16	0.00213933	0.0016644	-0.124343	-0.164267	5.44502	7.67372
1.2	0.00211694	0.0016471	0.	0.	4.90032	7.90593
Combined (thermal+centrifugal+pressure)						
1.	0.00226315	0.0017643	-1.	-1.	8.7046	6.70904
1.04	0.00222925	0.0017365	-0.706985	-0.763819	7.68168	6.95248
1.08	0.00219863	0.0017121	-0.470502	-0.54649	6.81827	7.19767
1.12	0.00217098	0.0016905	-0.279356	-0.34714	6.08438	7.4441
1.16	0.00214607	0.0016713	-0.124812	-0.165127	5.45645	7.69124
1.2	0.00212365	0.0016539	0.	0.	4.91586	7.93862

- The dimensionless radial stresses are all in compression under individual thermal and pressure loads, combined (thermal+pressure), (centrifugal+pressure) and thermo-mechanical loads, viz., combined thermal, pressure and centrifugal loads. The absolute value of the maximum radial stress is observed at the vicinity of mid-surface under individual thermal, individual centrifugal, combined (thermal+centrifugal) loads while it is on the inner surface under other loads.
- Tangential stresses are all in tension except for thermal loads for all inhomogeneity indexes. Maximum hoop stress is at the inner surface for negative inhomogeneity indexes.
- While $\beta = -1$ seems to be a better choice for almost uniform equivalent stress variation under combined (thermal+centrifugal) loads, $\beta = 2$ is the best for other types of combined loads (Fig. 3).

5. Examples with Physical FGMs

In the present study, three types of physical metal-ceramic pairs are considered to understand the thermo-mechanical behavior of such structures. Material properties of the constituents are given in Table 2 for nickel-silicon nitride (Ni-Si₃N₄), aluminum-aluminum oxide (Al-Al₂O₃), and stainless steel-zirconium oxide (SUS304-ZrO₂). Contrary to the benchmark example, the inhomogeneity indexes are now to be determined exactly regarding to the types of metal and ceramic and their locations. Assume that the inner surface is to be full ceramic and the outer surface is to be full metal. In this case the intermediate surface consists of a mixture of metal and ceramic which obeys the power law gradient given by Eqs. (2) and (13). The values of inhomogeneity indexes depend on the annulus aspect ratio, a/b , as well as the constituents' material properties. Positive inhomogeneity index means an increase from the inner surface towards the outer. The contrary is true for negative inhomogeneity indexes. The inhomogeneity indexes are computed under this assumption as follows

$$\beta = \ln\left(\frac{E_a}{E_b}\right) / \ln\left(\frac{a}{b}\right); \quad q = \ln\left(\frac{\rho_a}{\rho_b}\right) / \ln\left(\frac{a}{b}\right); \quad (37)$$

$$n = \ln\left(\frac{\alpha_a}{\alpha_b}\right) / \ln\left(\frac{a}{b}\right); \quad \mu = \ln\left(\frac{k_a}{k_b}\right) / \ln\left(\frac{a}{b}\right)$$

Material and geometrical properties of the annulus are determined as: $\omega = 100 \frac{rad}{s}$; $p_a = 30MPa$; $p_b = 5MPa$; $T_a = 373K$; $T_b = 273K$; $a = 0.5m$; $b = 1.0m$. Results are tabulated in Tables 3-5 and illustrated in Figs. 4-5. From those tables and figures, it is mostly observed that the thermal effects are not negligible as in the previous example since the surface temperature difference has been taken much higher than the previous example.

Combined radial displacements of three types FGMs are closer to the ceramic constituents. The radial displacements build-up as r/b increases under thermal loadings for three FGMs while they decrease with increasing r/b ratios under individual pressure and centrifugal loads. Ni/ Si₃N₄ has the smallest radial displacements than other two FGMs while Al/Al₂O₃ has the highest ones.

The characteristic variation of radial stresses of Ni/ Si₃N₄ and Al/Al₂O₃ are similar to each other to some extent. SUS304/ ZrO₂ has entirely combined thermo-mechanical radial compression stresses while the others have tension-compression in nature. It is fascinating that the behavior of FGMs are totally different from the behaviors of individual metal and ceramics under thermal loading. While individual ceramic and metal give thermal radial stresses in compression, FGM offers radial stresses in tension. Maximum combined thermo-mechanical radial stress is observed at both the inner surface and at the surface between the inner and mid-surface for both Ni/ Si₃N₄ and Al/Al₂O₃.

It is observed from Fig. 4 that the characteristic behaviors of Ni/ Si₃N₄ and Al/Al₂O₃ are similar under both individual pressure and centrifugal loads. However, Ni/ Si₃N₄ seems much proper than Al/Al₂O₃ under individual pressure while it is the worst for individual rotation. For combined thermo-mechanical loadings, SUS304/ ZrO₂ exhibits the most appropriate hoop and equivalent stresses (Figs. 4-5). The performance of SUS304/ ZrO₂ under centrifugal forces are better than the others. SUS304/ ZrO₂ also shows the best performance under individual thermal loading and combined thermal and mechanical loads.

Table 2. The physical constituent materials used in the present study

		E (GPa)	ρ (kg/m ³)	ν	k (W/mK)	α (1/K)
Metal	Nickel (Ni)	199.5	8900	0.3	90.7	13.3E-6
	Aluminum (Al)	70	2700	0.3	204	23.E-6
	SUS304 (Stainless Steel)	201.04	7800	0.3262	15.379	12.33E-6
Ceramic	Silicon Nitride (Si ₃ N ₄)	348.43	4429	0.24	1.209	5.8723E-6
	Aluminum Oxide (Al ₂ O ₃)	393	3970	0.3	30.1	8.8E-6
	Zirconium oxide (ZrO ₂)	116.4	3657	0.3	1.78	8.7E-6

Table 3. Elastic fields of circular annulus with physical FGMs ($Ni-Si_3N_4$ and $Al-Al_2O_3$) under thermal and centrifugal loads

r/b	Thermal			Centrifugal		
	Si_3N_4	$Ni-Si_3N_4$	Ni	Si_3N_4	$Ni-Si_3N_4$	Ni
u_r (mm)						
0.5	0.915496	1.35275	2.07348	0.0544997	0.111344	0.193781
0.6	1.13013	1.56113	2.56306	0.0527081	0.107424	0.18533
0.7	1.32442	1.79872	3.00432	0.0518973	0.106284	0.180747
0.8	1.50395	2.07772	3.41054	0.0514076	0.106298	0.177593
0.9	1.67208	2.4001	3.78969	0.0508324	0.106125	0.174377
1.	1.83099	2.76541	4.14696	0.0498919	0.10448	0.170081
σ_r (GPa)						
0.5	0.	0.	0.	0.	0.	0.
0.6	-0.01477	0.0265844	-0.0191536	0.0035078	0.00849608	0.0071793
0.7	-0.0171497	0.0339282	-0.0222396	0.0044807	0.0108177	0.0091706
0.8	-0.0137526	0.0285571	-0.0178342	0.0039350	0.00958235	0.0080538
0.9	-0.0075515	0.0161291	-0.00979269	0.0023562	0.00583515	0.0048225
1.	0.	0.	0.	0.	0.	0.
σ_θ (GPa)						
0.5	-0.125218	0.17949	-0.16238	0.0379787	0.0775914	0.0773188
0.6	-0.0566285	0.123614	-0.07344	0.0314503	0.0561662	0.0637759
0.7	-0.0087453	0.0326852	-0.01134	0.0269076	0.0432787	0.0542641
0.8	0.0272743	-0.0484405	0.035369	0.0233343	0.0343077	0.0467034
0.9	0.0558414	-0.116065	0.072415	0.020245	0.0271806	0.0401003
1.	0.079391	-0.172665	0.102954	0.0173838	0.0208437	0.0339313
r/b	Al_2O_3	$Al-Al_2O_3$	Al	Al_2O_3	$Al-Al_2O_3$	Al
u_r (mm)						
0.5	1.37193	2.10962	3.58572	0.0438796	0.0680382	0.167545
0.6	1.69586	2.44523	4.43236	0.0419658	0.0652997	0.160237
0.7	1.98782	2.85505	5.19543	0.0409282	0.0645656	0.156275
0.8	2.2566	3.34168	5.89792	0.040214	0.0648825	0.153548
0.9	2.50747	3.90588	6.55361	0.0394857	0.0652246	0.150767
1.	2.74385	4.54737	7.17143	0.038513	0.0643676	0.147054
σ_r (GPa)						
0.5	0.	0.	0.	0.	0.	0.
0.6	-0.024965	0.0363991	-0.011622	0.0032025	0.00463795	0.002178
0.7	-0.0289873	0.0364721	-0.0134946	0.0040907	0.00508015	0.0027821
0.8	-0.0232453	0.0257909	-0.0108215	0.0035925	0.00395046	0.0024433
0.9	-0.0127639	0.0126957	-0.00594201	0.0021512	0.0021415	0.001463
1.	0.	0.	0.	0.	0.	0.
σ_θ (GPa)						
0.5	-0.211649	0.36818	-0.0985297	0.0344894	0.053478	0.0234563
0.6	-0.0957164	0.104515	-0.0445591	0.0284484	0.0285597	0.0193478
0.7	-0.0147818	-0.0160097	-0.00688143	0.0242055	0.0172121	0.0164621
0.8	0.0461005	-0.0752527	0.0214613	0.0208329	0.0110787	0.0141685
0.9	0.094386	-0.105572	0.0439398	0.0178874	0.00723665	0.0121652
1.	0.134191	-0.121214	0.0624703	0.0151356	0.00450573	0.0102938

Table 4. Elastic fields of circular annulus with physical FGMs ($Ni-Si_3N_4$ and $Al-Al_2O_3$) under pressure and combined loads

r/b	Pressures			Thermo-mechanical		
	Si_3N_4	$Ni-Si_3N_4$	Ni	Si_3N_4	$Ni-Si_3N_4$	Ni
u_r (mm)						
0.5	0.062949	0.079638	0.114453	1.03294	1.54374	2.38171
0.6	0.053791	0.069195	0.097522	1.23663	1.73775	2.84591
0.7	0.047456	0.061447	0.085762	1.42377	1.96645	3.27082
0.8	0.042888	0.055445	0.077235	1.59824	2.23946	3.66537
0.9	0.039496	0.050644	0.070862	1.76241	2.55687	4.03493
1.	0.036928	0.046708	0.065998	1.91781	2.9166	4.38304
σ_r (GPa)						
0.5	-0.03	-0.03	-0.03	-0.03	-0.03	-0.03
0.6	-0.0198148	-0.0187403	-0.0198148	-0.031077	0.016340	-0.031789
0.7	-0.0136735	-0.0125855	-0.0136735	-0.0263425	0.032160	-0.026743
0.8	-0.0096875	-0.0089115	-0.0096875	-0.019505	0.029228	-0.019468
0.9	-0.0069547	-0.0065699	-0.0069547	-0.01215	0.015394	-0.011925
1.	-0.005	-0.005	-0.005	-0.005	-0.005	-0.005
σ_θ (GPa)						
0.5	0.0366667	0.0473966	0.0366667	-0.05057	0.304478	-0.048396
0.6	0.0264815	0.0296411	0.0264815	0.001303	0.209421	0.016822
0.7	0.0203401	0.0199344	0.0203401	0.038502	0.0958984	0.0632634
0.8	0.0163542	0.0141393	0.0163542	0.066963	6.543.10 ⁻⁶	0.0984268
0.9	0.0136214	0.0104453	0.0136214	0.089708	-0.0784388	0.126136
1.	0.0116667	0.0079682	0.0116667	0.108442	-0.143853	0.148552
r/b	Al_2O_3	$Al-Al_2O_3$	Al	Al_2O_3	$Al-Al_2O_3$	Al
u_r (mm)						
0.5	0.0581001	0.106582	0.32619	1.47391	2.28424	4.07945
0.6	0.0495052	0.0946808	0.277937	1.78733	2.60521	4.87054
0.7	0.0435357	0.0847664	0.244422	2.07228	3.00439	5.59613
0.8	0.039207	0.07593	0.220119	2.33602	3.48249	6.27159
0.9	0.0359721	0.0675964	0.201958	2.58292	4.0387	6.90633
1.	0.033503	0.0593678	0.188095	2.81587	4.6711	7.50658
σ_r (GPa)						
0.5	-0.03	-0.03	-0.03	-0.03	-0.03	-0.03
0.6	-0.0198148	-0.0164097	-0.0198148	-0.0415773	0.024627	-0.029259
0.7	-0.0136735	-0.0105156	-0.0136735	-0.0385701	0.031037	-0.024386
0.8	-0.0096875	-0.0075873	-0.0096875	-0.0293403	0.022154	-0.018066
0.9	-0.0069547	-0.0059712	-0.0069547	-0.0175675	0.008866	-0.011434
1.	-0.005	-0.005	-0.005	-0.005	-0.005	-0.005
σ_θ (GPa)						
0.5	0.0366667	0.0747737	0.0366667	-0.140493	0.496432	-0.038407
0.6	0.0264815	0.0344695	0.0264815	-0.0407865	0.167544	0.0012701
0.7	0.0203401	0.0174417	0.0203401	0.0297638	0.018644	0.0299209
0.8	0.0163542	0.009302	0.0163542	0.0832876	-0.05487	0.051984
0.9	0.0136214	0.0050426	0.0136214	0.125895	-0.09329	0.0697264
1.	0.0116667	0.0026557	0.0116667	0.160993	-0.11405	0.0844307

Table 5. Elastic fields of circular annulus with SUS304 – ZrO₂.

<i>r/b</i>	<i>Thermal</i>			<i>Centrifugal</i>		
	<i>ZrO₂</i>	<i>SUS304 – ZrO₂</i>	<i>SUS304</i>	<i>ZrO₂</i>	<i>SUS304 – ZrO₂</i>	<i>SUS304</i>
<i>u_r (mm)</i>						
0.5	1.35634	1.5991	1.92226	0.13647	0.173756	0.169483
0.6	1.67659	1.91271	2.37753	0.130518	0.165861	0.161298
0.7	1.96523	2.21899	2.7871	0.127291	0.161489	0.156647
0.8	2.23095	2.53105	3.16354	0.125069	0.158363	0.153359
0.9	2.47897	2.8539	3.51438	0.122804	0.155188	0.150113
1.	2.71267	3.18944	3.84451	0.119779	0.151119	0.146012
<i>σ_r (GPa)</i>						
0.5	0.	0.	0.	0.	0.	0.
0.6	-0.00731	0.001025	-0.01789	0.002950	0.004511	0.0063420
0.7	-0.00849	0.002963	-0.02078	0.003768	0.006304	0.0081010
0.8	-0.00681	0.003702	-0.01666	0.003309	0.006010	0.0071144
0.9	-0.00374	0.002721	-0.00915	0.001982	0.003883	0.00426
1.	0.	0.	0.	0.	0.	0.
<i>σ_θ (GPa)</i>						
0.5	-0.06197	-0.00546	-0.1517	0.031770	0.040451	0.0681457
0.6	-0.02803	0.013470	-0.06861	0.026206	0.038564	0.0561143
0.7	-0.00433	0.013459	-0.01059	0.022297	0.036985	0.0476314
0.8	0.013499	0.002947	0.03304	0.019190	0.035259	0.0408597
0.9	0.027638	-0.01408	0.06765	0.016477	0.033118	0.0349215
1.	0.039293	-0.03551	0.096182	0.013942	0.030381	0.0293543
<i>Pressures</i>			<i>Thermo-mechanical</i>			
<i>u_r (mm)</i>						
0.5	0.196163	0.157868	0.115531	1.68897	1.93073	2.20727
0.6	0.167144	0.131506	0.098324	1.97425	2.21007	2.63715
0.7	0.146989	0.114426	0.086352	2.23951	2.49491	3.0301
0.8	0.132374	0.102797	0.077653	2.4884	2.79221	3.39455
0.9	0.121452	0.094606	0.071135	2.72323	3.10369	3.73562
1.	0.113116	0.088701	0.066144	2.94557	3.42926	4.05667
<i>σ_r (GPa)</i>						
0.5	-0.03	-0.03	-0.03	-0.03	-0.03	-0.03
0.6	-0.01981	-0.02084	-0.01981	-0.02418	-0.01530	-0.0313666
0.7	-0.01367	-0.01480	-0.01367	-0.01839	-0.00553	-0.0263493
0.8	-0.00969	-0.01055	-0.00969	-0.01318	-0.00084	-0.0192342
0.9	-0.00695	-0.00741	-0.00695	-0.00871	-0.00080	-0.0118433
1.	-0.005	-0.005	-0.005	-0.005	-0.005	-0.005
<i>σ_θ (GPa)</i>						
0.5	0.036667	0.027359	0.036667	0.006462	0.062351	-0.0468881
0.6	0.026482	0.022931	0.026482	0.024660	0.074965	0.0139907
0.7	0.020340	0.020174	0.020340	0.038309	0.070618	0.0573767
0.8	0.016354	0.018363	0.016354	0.049044	0.056569	0.0902567
0.9	0.013621	0.017129	0.013621	0.057736	0.036171	0.116194
1.	0.011667	0.016267	0.011667	0.064902	0.011134	0.137203

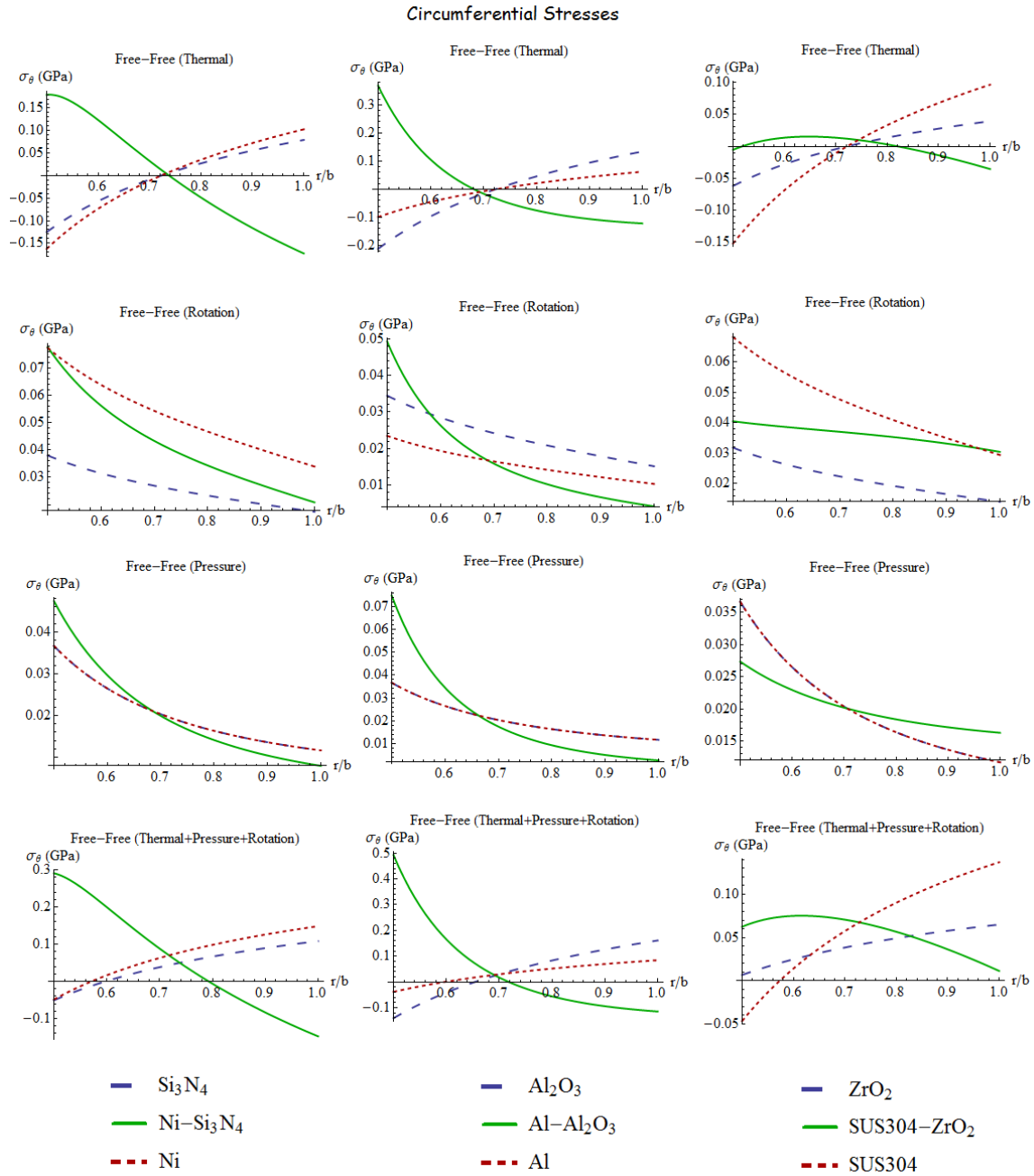


Figure 4. Variation of the hoop stress with FGM types under individual and combined loads

6. Conclusions

The present study addresses exact thermo-mechanical analysis of a rotating FGM circular annulus or disc. After proposing closed form solutions for separate loads such as centrifugal, thermal, and pressure, two parametric studies are conducted. The first study is related to the benchmark example with hypothetically chosen inhomogeneity parameters. This example is originally handled for circular annuli in this manuscript. The second study considers the thermo-mechanical behavior of three types of physical ceramics, metals, and FGMs.

Separate and combined effects of each loading are studied in two examples. Those studies generally imply that the effect of thermal loads may be either negligible compared to inertia forces as in the first benchmark example or may be having higher importance than the inertias as in the second example. It is also concluded that the thermal characteristics of both individual metal and ceramic are totally different from FGM's thermal traits. The author hopes that both the formulas proposed in the present study and graphs are to be helpful for the demands of the related industries.

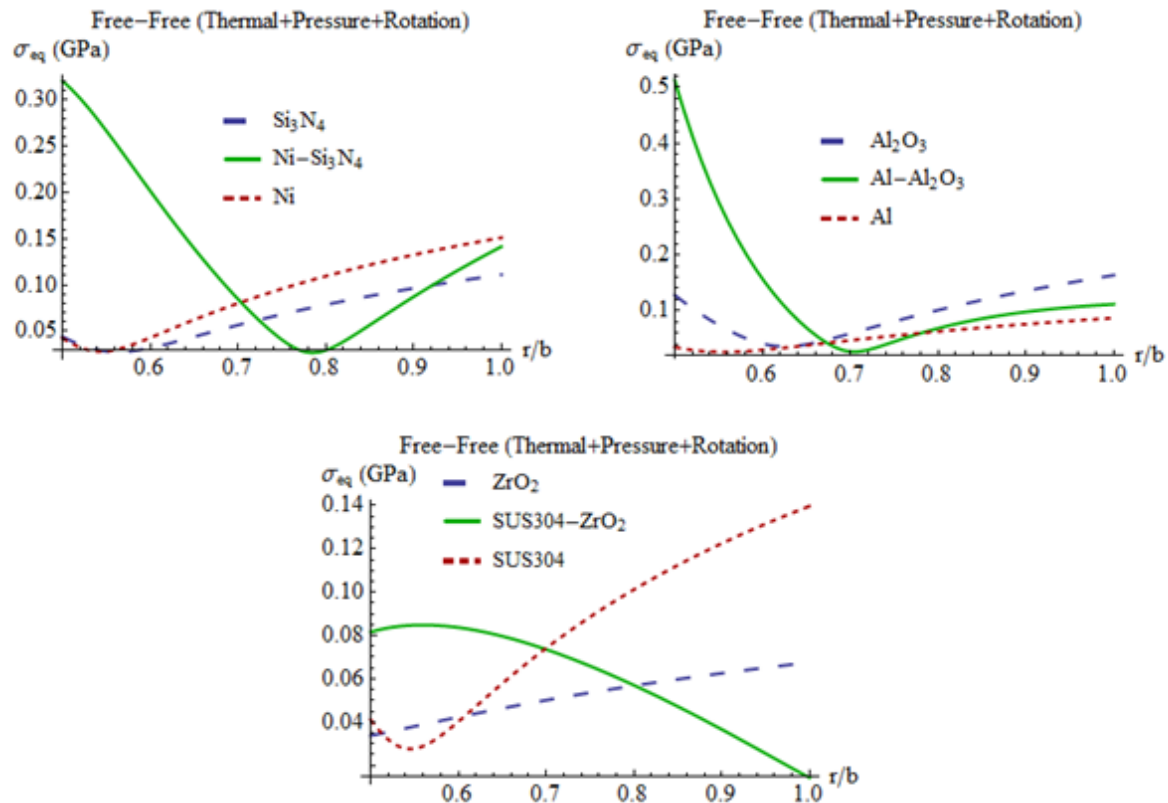


Figure 5. Variation of the equivalent stress with FGMs under combined loads

References

- [1] B.S. Reddy, J. S. Kumar, C.E. Reddy, K.V.K. Reddy, "Static Bending Behavior of Functionally Graded Plates Subjected to Mechanical Loading". *Jordan Journal of Mechanical and Industrial Engineering, JJMIE*, Vol. 8, No. 4, 2014, 193-206.
- [2] H. Eskandari, "Three-dimensional investigations of stress intensity factors in a rotating thick-walled FGM cylinder". *Jordan Journal of Mechanical and Industrial Engineering, JJMIE*, Vol. 10, No. 2, 2016, 105-113.
- [3] C.O. Horgan, A.M. Chan, "The stress response of functionally graded isotropic linearly elastic rotating disks". *Journal of Elasticity*, Vol. 55, No. 3, 1999, 219-230.
- [4] J.F. Durodola, O. Attia, "Deformation and stresses in FG rotating disks". *Compos Sci Technol*, Vol. 60, 2000, 987-995.
- [5] A.M. Zenkour, "Analytical solutions for rotating exponentially-graded annular disks with various boundary conditions". *Int J Str Stab Dyn*, Vol. 5, No. 4, 2005, 557-577.
- [6] A.M. Zenkour, "Elastic deformation of the rotating functionally graded annular disk with rigid casing". *J Mater Sci*, Vol. 42, 2007, 9717-9724.
- [7] A.N. Eraslan, T. Akiş, "On the plane strain and plane stress solutions of functionally graded rotating solid shaft and solid disk problems". *Acta Mechanica*, Vol. 181, No. 1-2, 2006, 43-63.
- [8] M. Asghari, E. Ghafoori, "A three-dimensional elasticity solution for functionally graded rotating disks". *Composite Structures*, Vol. 92, No. 5, 2010, 1092-1099.
- [9] H. Argeso, "Analytical solutions to variable thickness and variable material property rotating disks for a new three-parameter variation function". *Mech Based Des Struc*, Vol. 40, No. 2, 2012, 133-152.
- [10] X.L. Peng, X.F. Li, "Effects of gradient on stress distribution in rotating functionally graded solid disks". *J Mech Sci Technol*, Vol. 26, 2012, 1483-1492.
- [11] M.Z. Nejad, A. Rastgoo, A. Hadi, "Exact elasto-plastic analysis of rotating disks made of functionally graded materials". *Int J Eng Sci*, Vol. 85, 2014, 47-57.
- [12] T. Dai, H.L. Dai, "Investigation of mechanical behavior for a rotating FGM circular disk with a variable angular speed". *J Mech Sci Technol*, Vol. 29, No. 9, 2015, 3779-3787.
- [13] H. Çallıoğlu, M. Sayer, E. Demir, "Elastic-plastic stress analysis of rotating functionally graded discs". *Thin-Walled Structures*, Vol. 94, 2015, 38-44.
- [14] C.O. Horgan, A.M. Chan, "The pressurized hollow cylinder or disk problem for functionally graded isotropic linearly elastic materials". *Journal of Elasticity*, Vol. 55, No. 1, 1999, 43-59.
- [15] L.H. You, J.X. Wang, B.P. Tang, "Deformations and stresses in annular disks made of functionally graded materials subjected to internal and/or external pressure". *Meccanica*, Vol. 44, 2009, 283-292.
- [16] N. Tutuncu, B. Temel, "A novel approach to stress analysis of pressurized FGM cylinders, disks and spheres". *Composite Structures*, Vol. 91, 2009, 385-390.
- [17] M.H. Lotfian, M.Z. Nejad, M. Abedi, M. Ghannad, "An elasticity solution for functionally graded hollow disks under radially symmetry loads". *J Basic Appl Sci Res*, Vol. 1, No. 11, 2011, 2435-2441.
- [18] M.Z. Nejad, M. Abedi, M.H. Lotfian, M. Ghannad, "Elastic analysis of exponential FGM disks subjected to internal and external pressure". *Central European Journal of Engineering*, Vol. 3, No. 3, 2013, 459-465.
- [19] N. Noda, "Thermal stress in materials with temperature-dependent properties". *Appl Mech Rev*, Vol. 44, No. 9, 1991, 383-397.

- [20] Y. Tanigawa, "Some basic thermoplastic problems for nonhomogeneous structural materials". *Appl Mech Rev*, Vol. 48, 1995, 377–389.
- [21] M. Bakshi, A. Bagri, M.R. Eslami, "Coupled thermoelasticity of functionally graded disk". *Mech Adv Mater Struct*, Vol. 13, 2006, 219–225.
- [22] Y.V. Tokovy, C.C. Ma, "Thermal stresses in anisotropic and radially inhomogeneous annular domains". *J. Therm. Stress*, Vol. 31, 2008, 892–913.
- [23] A.M. Zenkour, "Thermoelastic analysis of an annular sandwich disk with metal/ceramic faces and functionally graded core". *J Thermoplas Compos*, Vol. 22, 2009, 163–181.
- [24] X.L. Peng, X.F. Li, "Thermoelastic analysis of functionally graded annulus with arbitrary gradient". *Appl. Math. Mech. - Engl. Ed.*, Vol. 30, No. 10, 2009, 1211–1220.
- [25] B. Arnab, S.M.R. Islam, A.A. Khalak, A.M. Afsar, "Finite difference solution to thermoelastic field in a thin circular FGM disk with a concentric hole". *Procedia Engineering*, Vol. 90, 2014, 193-198.
- [26] N.N. Aleksandrova, "Effect of thermal gradients on stress/strain distributions in a thin circular symmetric plate". *Structural Engineering and Mechanics*, Vol. 58, No. 4, 2016, 627-639.
- [27] H. Çallıoğlu, M. Sayer, E. Demir, "Stress analysis of functionally graded discs under mechanical and thermal loads". *Indian J Eng Mater Sci*, Vol. 18, 2011, 111-118.
- [28] A.Kursun, M. Topçu, T. Tetik, "Stress analysis of functionally graded disc under thermal and mechanical loads". *Procedia Engineering*, Vol. 10, 2011, 2949–2954.
- [29] D. Gönczi, I. Ecsedi, "Thermoelastic analysis of functionally graded hollow circular disc". *Archive of Mechanical Engineering*, Vol. LXII, No. 1, 2015, 5-18.
- [30] A.M. Zenkour, "On the magneto-thermo-elastic responses of FG annular sandwich disks", *International Journal of Engineering Science*, Vol. 75, 2014, 54–66.
- [31] A.M. Zenkour, "Steady-state thermoelastic analysis of a functionally-graded rotating annular disk". *International Journal of Structural Stability and Dynamics*, Vol. 6, No. 4, 2006, 1-16.
- [32] S.A.H. Kordkheili, R. Naghdabadi, "Thermoelastic analysis of a functionally graded rotating disk". *Compos Struct*, Vol. 79, No. 4, 2007, 508–516.
- [33] J. Go, A.M. Afsar, J.I. Song, "Analysis of thermoelastic characteristics of a rotating FGM circular disk by finite element method". *Adv Compos Mater*, Vol. 19, No. 2, 2010, 197–213.
- [34] A.M. Afsar, J. Go, J.I. Song, "A mathematical analysis of thermoelastic characteristics of a rotating circular disk with an FGM coating at the outer surface". *Adv Compos Mater*, Vol. 19, No. 3, 2010, 269-288.
- [35] A.M. Afsar, J. Go, "Finite element analysis of thermoelastic field in a rotating FGM circular disk". *Applied Mathematical Modelling*, Vol. 34, 2010, 3309-3320.
- [36] A.M. Afsar, F.A. Sohag, "Effect of FGM coating on thermoelastic characteristics of a rotating circular disk". *Proceedings of MARTEC 2010, The International Conference on Marine Technology*, 11-12 December BUET, Dhaka, Bangladesh. 2010, 459-464.
- [37] J.F. Gong, P.J. Ming, L.K. Xuan, W.P. Zhang, "Thermoelastic analysis of three dimensional functionally graded rotating disks based on finite volume method". *Proc. Inst. Mech. Eng. C: Journal of Mechanical Engineering Science*. Vol. 228, No. 4, 2014, 583-598.
- [38] V. Yıldırım, "Thermomechanical characteristics of a functionally graded mounted uniform disc with/without rigid casing". *The Journal of Aerospace Technology and Management (JATM)*, Vol. 11, 2019, <http://dx.doi.org/10.5028/jatm.v11.1008>
- [39] M. Jabbari, S. Sohrabpour, M.R. Eslami, "Mechanical and thermal stresses in a functionally graded hollow cylinder due to radially symmetric loads". *Int J Pressure Vessels and Piping*, Vol. 79, 2002, 493–497.
- [40] M.R. Eslami, M.H. Babaei, R. Poultangari, "Thermal and mechanical stresses in a functionally graded thick sphere". *Int J Pressure Vessel Piping*, Vol. 82, 2005, 522–527.
- [41] V. Yıldırım, "Exact thermal analysis of functionally graded cylindrical and spherical vessels". *International Journal of Engineering & Applied Sciences (IJEAS)*, Vol. 9, No. 2, 2017, 112-126. [doi.org/10.24107/ijeas.318459](http://dx.doi.org/10.24107/ijeas.318459)
- [42] V. Yıldırım, "Heat-induced, pressure-induced and centrifugal-force-induced exact axisymmetric thermo-mechanical analyses in a thick-walled spherical vessel, an infinite cylindrical vessel, and a uniform disk made of an isotropic and homogeneous material". *International Journal of Engineering & Applied Sciences (IJEAS)*, Vol. 9, No. 2, 2017, 66-87. <http://dx.doi.org/10.24107/ijeas.309786>
- [43] V. Yıldırım, "Analytic solutions to power-law graded hyperbolic rotating discs subjected to different boundary conditions". *International Journal of Engineering & Applied Sciences (IJEAS)*, Vol. 8, No. 1, 2016, 38-52.

Nabatean Archaeometallurgy at Petra, Jordan

Khrisat, Bilal^{a,*}, L.Campanella^b, D.Ferro^c, S.Bovani^b, T.Akashah^a

^a Hashemite University, POB 150459, Zarqa - 13133 Jordan.

^b University of Rome "La Sapienza", P.le Aldo Moro 5, 00185 Rome, Italy.

^c Institute for Nanostructured Materials, Via dei Taurini 19, 00185 Rome, Italy.

Received 10 Jan. 2018

Abstract

Since the establishment of the Nabatean capital city ca. 300 B.C, stone craftsmen must have needed immense quantities of metal tools to carve the many and huge monuments of Petra. Though many researchers agreed that large metal consumption relates to the carving of the rock city, the enigma about the source of the metal and metal tools is still never fully understood. Surveys at the central area of the world cultural heritage site of Petra in Southern Jordan revealed evidence of what may be the first known metal smelting locality or workshop associated with the Nabatean occupation of Petra. In an area close to the famous Sextius Florentinus tomb, a thick layer on the surface testifying debris with ash, charcoal, slag, and junks of raw material related to smelting activities was found. Surface mapping and analyses of the exposed wall structures indicate a special construction in this area that is different from the regular habitation areas in the site. Samples from the site, potential raw material sources, and finished objects from excavations were analyzed using mainly Scanning Electron Microscopy (SEM) and Electron Beam Microanalysis Energy Dispersion (EDS) to produce valuable elements for samples comparison. Other methods like X-ray radiography, XRF, XRD analyses and general metallographic studies, were employed too. The mineralogical structure of the slag indicates medium to high furnace temperatures. Elements present in the analyzed samples indicate that the ore used was probably mined from the nearby hematite and manganese rich layers and veins of the local sandstone rocks at Wadi Al Mataha at the ancient city's fringes.

© 2018 Jordan Journal of Mechanical and Industrial Engineering. All rights reserved

Keywords: Nabatean, archaeometallurgy, Petra, slag, EDS, XRF;

1. Introduction

Metalwork was well known by the inhabitants of southern Jordan since late prehistory as known through the analytical studies of metallurgical findings from broad archaeological exposures in Wadi Faynan [1,2]. Analytical studies of metal samples from two oases in Northwest Arabia, Qurayyah and Tayma concluded that arsenical copper mainly of tin bronze and leaded tin bronze was processed at both sites [3].

Researchers in the Nabatean history believed that since the early days of the city's establishment (ca. 5th century B.C), the Nabatean must have searched for hard metal to carve their enormous rock-cut architectural monuments on the sandstone rocks, especially, during the sudden expansion and urbanization of Petra city at the end of the 1st century B.C.

Even with these logical needs, the question about these needs has never been well answered in the Nabatean archaeological research. Local sources and manufacturing were not proposed.

Since 1999, a systematic survey was carried out by the Hashemite University at Petra and the adjacent Nabatean settlements which sought to document and clarify the archaeological and architectural monuments and their

geoarchitectural characteristics. The survey attempts to produce a database about the archaeological monuments and their deterioration conditions for conservation [4]. During the undergoing survey Dr. Khrisat came across the unusual surface scatter of metal slag concentrations resting over dark grayish sediments in spatial association with a southwest facing masonry construction located northeast of the famous Sextius Florentinus tomb at Wadi Al Mataha area (also known as Tomb number 763 according to Brunnow and Domaszewski survey (Fig. 1)[5]. Several studies have used slags as a source of information on ancient metallurgical processes [6,7,8,9,10].

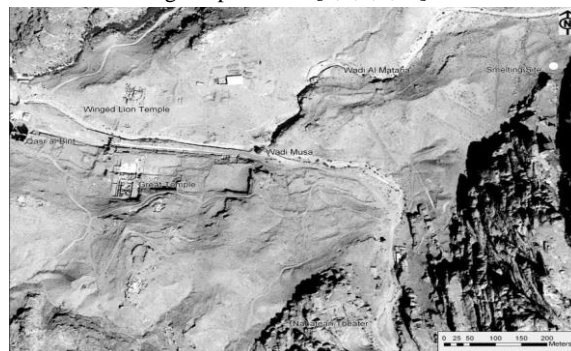


Figure 1. An aerial photo showing the major monuments in the central area and the smelting site

Our evidence is the first of its kind relating to metalworking in Petra. The term metalworking however, in the Nabatean archaeological context, inevitably conjures to a commercial or trade exchange practices of the Nabatean culture rather than a great metallurgical competence of the Nabatean themselves.

Easily recognized tooling marks are seen all over the rock-cut facades and stone-quarry areas of Petra. A limited number of metals, especially iron tools and weapons that were recovered from the archaeological investigations at Petra. According to Hammond, the evidence of a Nabatean iron tool kit transmitted to us by the different excavations revealed that copper and iron were used in building for both domestic and public structures at Petra [12]. During the excavation of the main theatre, Hammond found that metals were employed in its construction in which iron and copper fixtures were used to attach moldings. Additionally, iron nails keyed the plaster to the walls, and metal tools such as picks were used in carving the sandstone seats and entrance ways. At the Nabatean theatre, a possible iron dagger was found and is believed to date to 100 B.C [12]. Similarly, the excavations at the temple of the Winged Lions provided clear evidence that the Nabateans used copper and iron nails to key plaster elements in this temple and in the domestic structures adjacent to the temple, in addition a cube of iron was found in a ca. 200 B.C. grave at the same temple [13]. Other iron objects such as nails and knives were recovered from the residential area in Az-Zantur in the central area of the site, which is believed to go back in time to about 50 B.C. [14,15]. Tombs at Petra in the Wadi Sabra area revealed iron finger rings dated to around 50 B.C [16]. On the other hand, remains of metalworking sites or furnaces were never been unearthed or reported from the site.

Hence, the source of metal technologies and of the metals used as well by the Nabatean at the site has been always explained as being imported [5,17,11,18]. The general opinion is that the Nabatean strong trade and commercial relations with many contemporary cultures made it easier for them to obtain the metal objects through trade than maintaining over metal industries, especially during the urban expansion of the site in the second century B.C. The discovery of slags in a high concentration, and the results of our analysis of some of the slag samples [19,20] suggested an *in-situ* byproduct of metalworking which lead us to think about more realistic explanations for solution to these intriguing Nabatean technologies.

2. The Finding

During our survey, slag concentrations have been observed at three places in Petra; Wadi Sabra, Wadi Numair and Wadi Al Mataha. At this stage of our research, we are investigating the materials that have been collected from the slag concentrations in Wadi Al Mataha. The findings' location lies about 800 m northwest of the ancient center of Petra city (Fig. 1). From the exposed stratigraphy by natural erosion of the site sediments, a surface scatter includes material from several stages of the smelting process found in a spatial context with a

southwest facing Nabatean masonry construction located northeast of the famous Sextius Florentinus Tomb number 763 (Fig.2) is attested.

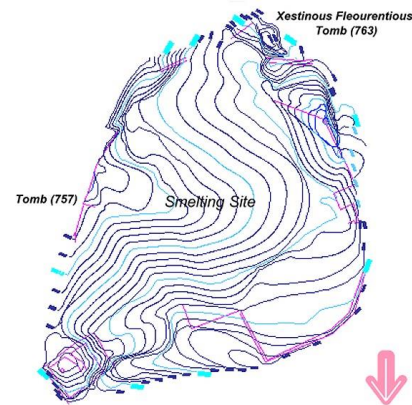


Figure 2: Smelting Site Map of Wadi Al Mataha, Petra.

Here, the slag bearing sediments cover about sixty square meters area and are about 60 centimeters thick in their middle parts. The archaeological remains fall by about some few centimeters along the slope, towards Wadi Al Mataha to the Northwest. The mound of debris shaped as semicircular and enclosed by a construction of crudely worked sandstone blocks. The deposit measures approximately 15 to 20 meters in north south by 45 meters in east-west directions. This anthropogenic sediment formation is a result of distinct special activities superimposed on architectural debris, slags and charcoal rich midden deposits.

The erosion of the fine sediments concentrated the large stones and slag fragments on the surface. Large portions of the exposed slag and other materials have recently been damaged and moved as the site is close to a major tourist track to Petra through Wadi al Mudhlim, and also due to increased tourism at Petra.

At the northern slope of the location and towards Wadi al Mataha sediments and the slag fragments are very loosely packed and mixed with other Nabatean cultural debris which suggests their contemporaneity. Moreover, cyclic dumping formed the heap at the slope by over a quite long period. The incorporated cultural material, especially the pottery indicates a date of the Nabatean/Roman time; it cannot be a colluvial mixture from various deposits.

Thus, the material in the deposit must be considered as representing one specialized operation that is different from the other deposits in the surroundings of the material, especially the slags quantities that suggest the state of being the product of one or of a very limited number of furnaces.

Apart from few small holes dug by looters, there is no record of any excavations at the location. The location of the site refers to the major wind direction (i.e. southwest/northeast) at the foot of al-Khubtha mountains which served to help furnacing. The high amount of charcoal within the site's sediments indicates an abundant availability of this fuel to the Nabatean during their smelting.

3. Sampling and the Analytical Procedure

After a detailed surface mapping and the demarcation of the different sectors of the site that is to be analyzed, sample selection was executed. A total of sixteen samples was documented, collected and analyzed. The samples included finished Nabatean iron and copper objects obtained from archaeological excavations, *in situ* fragments of what look like a copper ore and slag fragments that represent the residue of the ancient Nabatean smelting activities (Fig. 3). The samples also included some potential iron or sources collected from rock formations within the location vicinity.



Figure 3: Some of the fragments selected for the scientific investigations

The analytical procedures were achieved by utilizing mainly the scanning electron microscopy (SEM) and electron beam microanalysis energy dispersion (EDS) to produce quantitative and qualitative valuable elements for samples comparison [19,20,21]. Such methodologies have been already applied in studying the homologous findings as they provide the analytical composition of each phase forming the sample [22,23]. Other methodology like X-ray radiography, XRF, XRD analyses coupled with a preliminary optical examination provides a general idea of the method of manufacture on a macroscopic level. General metallographic studies can give a thorough picture of the history of an object and a much deeper understanding of the metallurgical processes employed.

4. Experimental Work and Results

A variety of schematic examinational techniques were employed. All samples were preliminarily checked under the optical and scanning electron microscope (SEM) to singularize areas of different morphological phases, and to be analyzed by microanalysis (EDS). To accomplish this, some of the samples were cut, cast in epoxy-resin and hand-polished. The mounted samples were then machine-polished to one quarter of a micron and etched by Nital acid solution to observe the metallographic structure. Finished metal artifacts samples, such as the ancient coin or the nail, were surface examined to avoid their destruction and to get their analytical information on their chemical composition and mode of making.

In total more than sixteen samples were collected from different archaeological contexts. Some were obtained from regular excavated sections, while others were taken from the exposed Nabatean sediments of the site and from

the expected raw material sources. Here, we summarize the main results of some of the key investigated samples of metallic consistence (Table 1), and incorporate new discoveries made and acquired during the investigations, which have provided us with information and helped in concluding about the iron-making and the metallurgy technologies in the city of Petra to add further understanding of the Nabatean early metal production.

Table 1. List of Petra's Key analyzed samples

S. No	Location	Date	Description
1	Site No. 1 (Wadi Al Mataha)	Nabatean	Slag fragment found incorporated within the site sediment
2	Site No. 2 (at Wadi Numair on surface)	Nabatean	Slag fragment found incorporated within the site sediment
3	Site No. 1 (Wadi Al Mataha)	Nabatean	Slag fragment found incorporated within the site sediment
4	Found along the vein at Wadi Al Mataha	Geologic Late Cambrian	Hematite deposits (Iron Ore?)
5	Site No. 1 (Wadi Al Mataha)	Geologic Late Cambrian	Possible copper ore found in abundance within the site sediments
6	From the excavation of Winged-lion temple	Nabatean	Iron Nail with square section
7	From the excavation of the erosional section of the Winged-lion temple	Nabatean	Nabatean Coin possibly Bronze

The analysis results of the key samples (in the following they will be quoted by their serial number of first column of Table 1) can be summarize as follows:

5. Sample 1

The slag sample shows a smooth compact frontal surface, with glassy luster, and is mostly homogeneously colored. The dorsal part shows a rough surface with many air vascular and has a metallic luster (Fig. 4)



Figure 4: digital photo Sample 1

To allow a very accurate quantitative determination of the micrometric areas, some very small parts of the sample were mounted in epoxy resin and smoothly leveled and had been cut them with a jeweler saw and polished to 400 mesh alumina and finished with colloidal silica. The samples were all etched with Nital acid solution (Fig 5-A). Then the sample was observed under the SEM-detector (Fig 5-B).

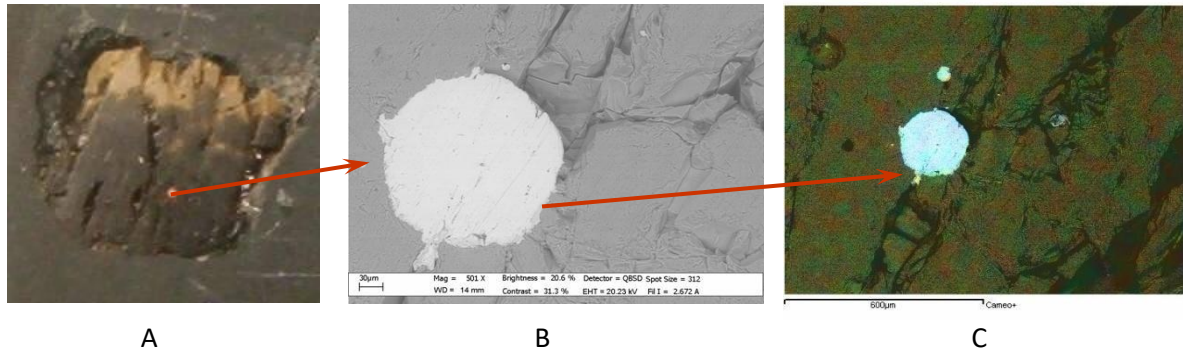


Figure 5. A - Fragment of sample 1 cast in epoxy-resin, B - and enlargement zone of copper inclusion, C - x-ray mapping shows the difference of distribution: Cu (blue) Mn (green), Si (yellow) and O (red).

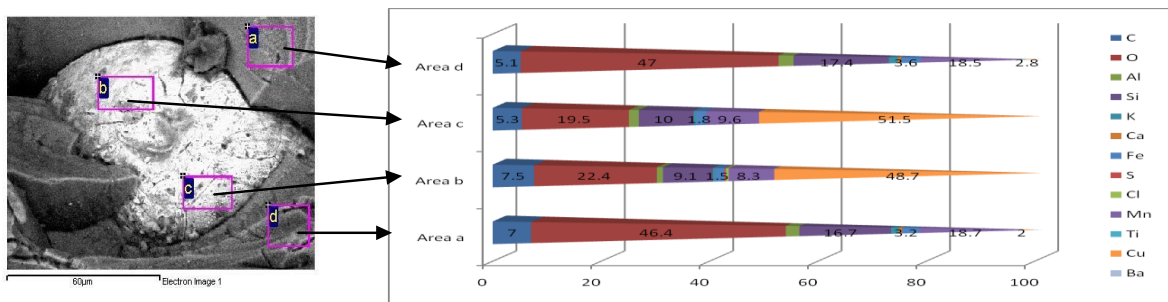


Figure 6. Analyses of the areas investigated by EDS (data in wt% ± 0.2)

By this way, it has been possible to foresee the existence of two phases through the atomic contrast from the use of the detector for the backscattered electrons. EDS punctual analysis detects Cu as a unique element constituting the round particles, and Mn, Si, O as those constituting the sample matrix, this is also evident through the x-ray mapping which shows the inclusions and the different elements distribution (Fig -C).

The composition determinations of the selected micro-areas are presented with their EDS values (Fig. 6) which allow to distinguish better the copper rich phase and the compact matrix that constituted by manganese-silicon compounds phase. Other elements are present in traces and at this stage it is impossible to assign a well determinate percentage values as the instrumental resolution is 0.2%, but their presence could give indications for further scientific investigation with higher resolution methodologies.

The sample indicates a slag product from a copper rich manganese sandstone raw material such as those exposed in the neighboring Wadi Faynan area.

6. Sample 2

The slag sample was collected from a naturally exposed section with incorporated Nabtean sediment at Wadi Numair (Table 1). The part of the sample represented in figure 7 is formed by a homogeneous material well-structured in a lamellar phase. The average elemental composition in EDS is presented in Figure (8) in which the presence of manganese as a principal component is evident.



Figure 7. Slag fragment sample number 2

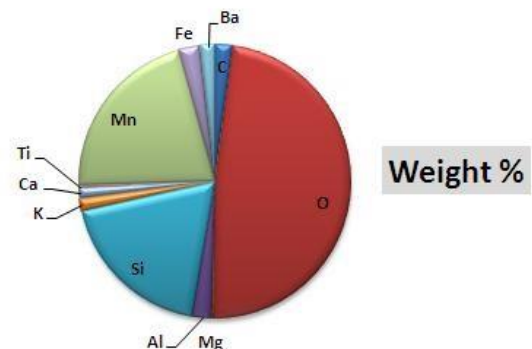


Figure 8. Elemental composition in EDS (data in wt% ± 0.2)

The manganese predominance is well evidenced in the pseudo colours x-ray mapping in the enlargement of analyzed area, Fig.9 Mn (blue) Al, Si (green) O (red)

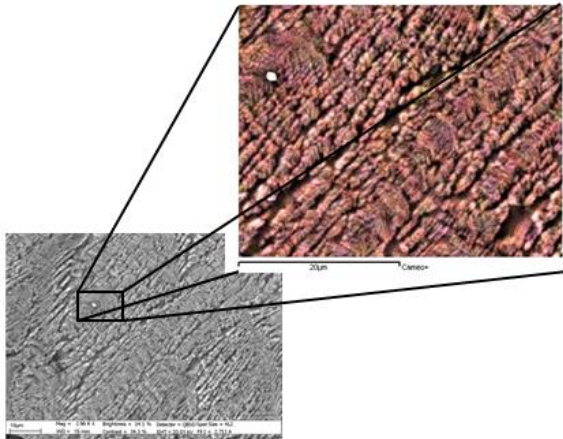


Figure 9. Enlargement zone with Mn presence

In other areas of the same fragment, a radial structure is present. The analytical composition indicates again a compound among Mn, Si, O, but also Al is present at a constant concentration.

Different modes of elements dispersion “visualization:” was made to “visualize” the copper inclusions in a homogeneous matrix (Fig. 9). The sample was characterized by the dominant presence of Mn. Other elements were not traceable even after reaching the resolution limits of the instrument.

In other areas of the same fragment, a radial structure is present. The analytical composition indicates again a compound among Mn, Si, O, but also Al is present at a constant concentration.

Different modes of elements dispersion “visualization:” was made to “visualize” the copper inclusions in a homogeneous matrix (Fig. 9). The sample was characterized by the dominant presence of Mn. Other elements were not traceable even after reaching the resolution limits of the instrument.

The continuation of the analysis of each sample areas presenting some differences in the microstructures; it is not possible to get constant value of elements composition for the complexity of the present phases. Punctual analyses combined with X-ray imaging led us to understand the nature of the investigated sample formation system (Fig. 10).

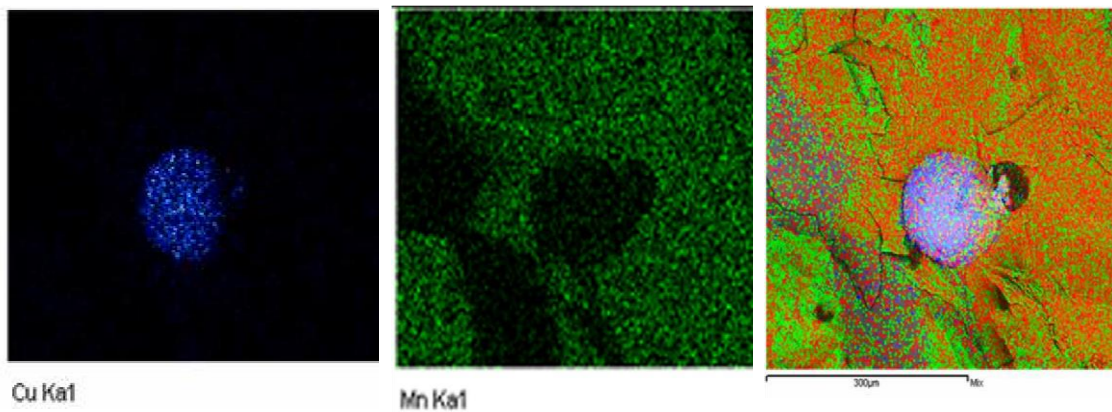


Figure 9: Different dispersion “visualization modes; a – copper inclusion (blue), b - x-ray imaging of an inclusion in a homogeneous matrix characterized by the presence of Mn (green), c - an imaging showing Cu (blue) Mn (green), Si (yellow) and O (red) of an inclusion in Sample 2

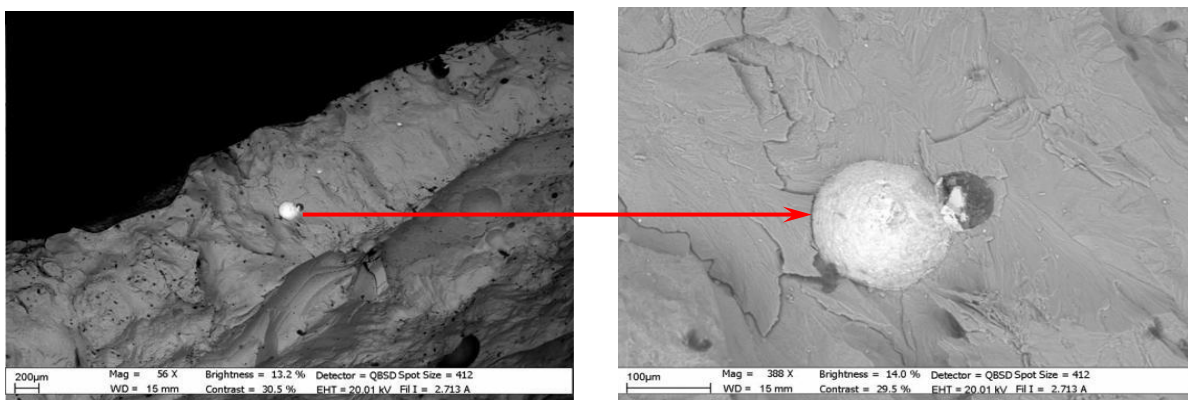


Figure 10. Enlargement zone with copper inclusion

Nevertheless, the spectrum (Fig.11) and the values reported in the chart, obtained from the areas marked in the SEM image (Fig.12), also show higher values only for the same elements.

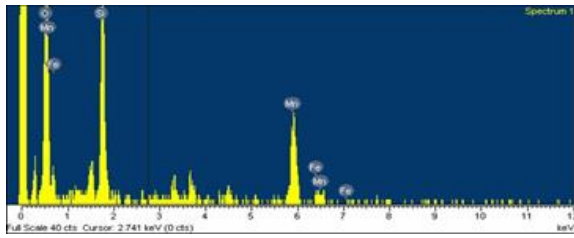


Figure 11. X-ray diffraction spectrum of Sample 4 showing the dominance of Fe, Mn, Si, and O.

7. Sample 3

It represents a slag collected from natural eroded section of site No. 1 at Wadi AlMataha (Fig. 13).

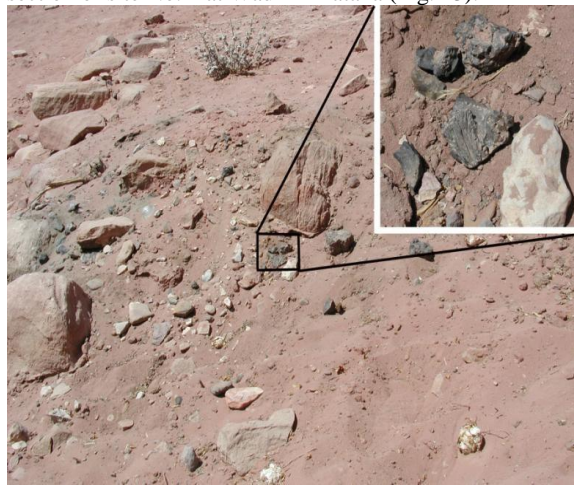


Figure 13. Natural exposed section of site No. 1 with the slag sample 3

The body of the sample mainly consists of a compact mass with glassy surface especially in some parts (areas a, c) of the analyzed fragment of the sample. At higher magnification, some evident change of morphology is represented by an oriented crystal growth appearance (area d). This might have been caused through the interaction with the sounding matrix. In the area “a” (marked by a black frame) a regular dotted morphology is observed (Fig. 14).

The morphological analysis led us to assure that strong thermal stresses followed by slow cooling processes had developed.

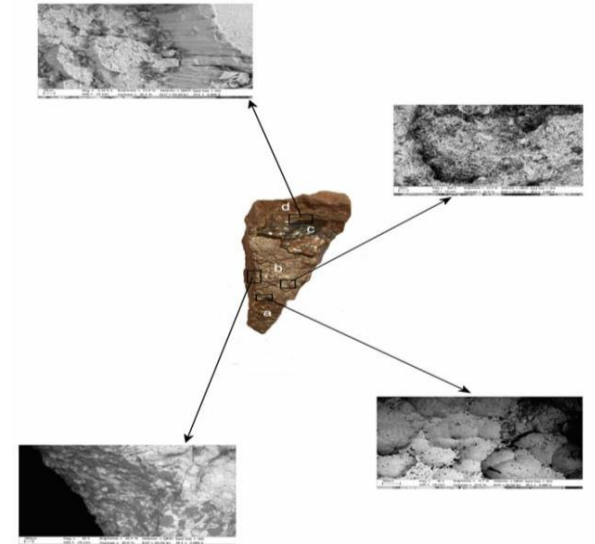


Figure 14: Sample 3 shows the different microphotographs of analyzed areas a,b,c, and d The overall composition of the sample is mainly formed by iron and oxygen. To eliminate the doubt of a physiological superficial oxidation process, determinations on spots along a line from the inner part to the surface have been carried out (Fig. 15).

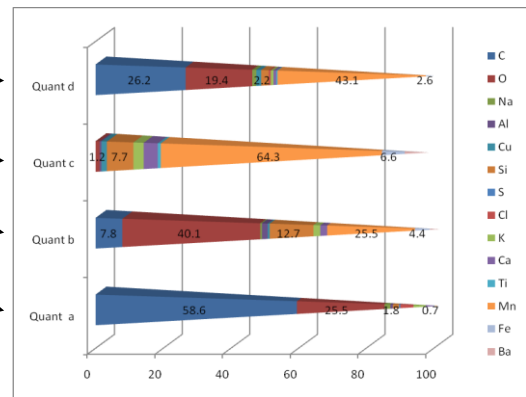
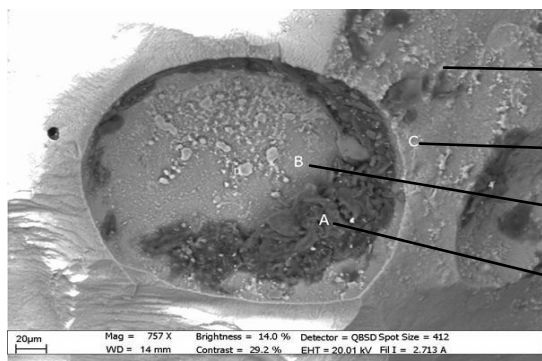


Figure 12: Microphoto of the investigated areas A,B,C & D and their EDS analysis result.

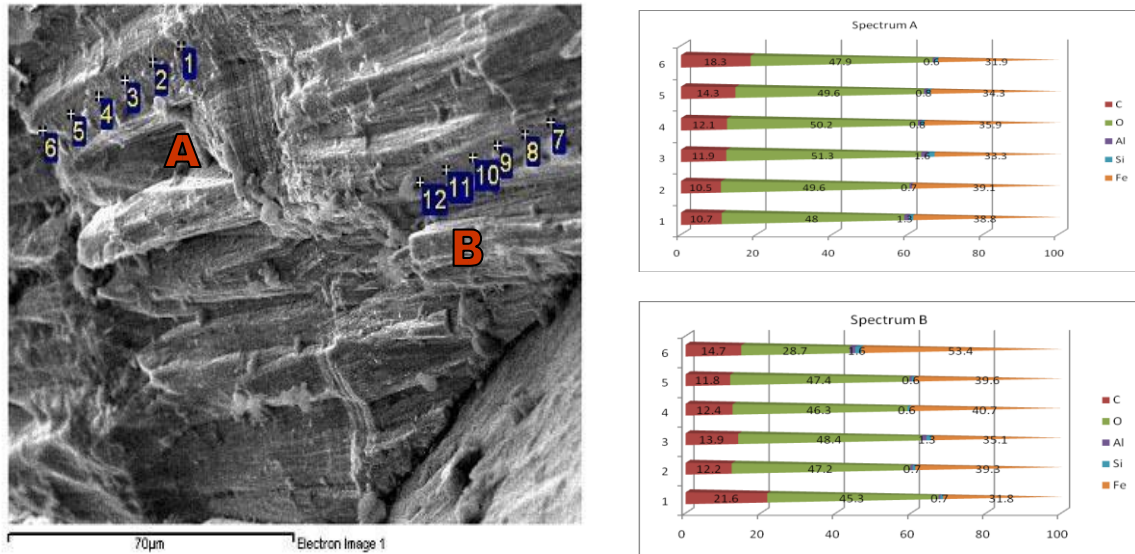


Figure 15: Microphoto of the investigated lines and the EDS analysis for each spectrum An increasing trend of the values of the iron is opposed to decreasing oxygen. The spectrum and the values reported in Fig. 15 Spectrum A & B which is obtained from the areas marked in the SEM image Fig.15.

Element	Zone A							A-B	A- B crystals	B	C
	A1	A2	A on ridge	A on bottom	average zone 1	average zone 2	average zone 3				
C	4.5	4.7	6.5	4.9	4.1	5.7	9.5	3.2	3.4	6.2	5.8
O	44.0	40.4	33.7	39.3	37.0	29.7	39.9	43.9	35.8	32.4	18.7
Al		1.3	0.8	0.8	1.1	0.8	0.7	1.1	2.1	1.0	0.4
Si	0.8	1.8	0.9	0.7	1.8	1.1	0.8	4.2	6.3		0.8
P			0.2	0.2				0.2	0.3		
Cl			0.3	0.27		0.2	0.2	0.1	0.1		
Ca		0.4	0.27	0.2	0.6	0.2		0.3	0.6		
Fe	50.7	50.6	56.6	53.3	55.1	61.9	48.8	46.9	50.4	60.5	74.4
Mg		0.3							0.5		
Na		0.3	0.4								

Table 2. Different areas investigated by EDS analysis, all the results are reported so to point out also trace elements at the limit (or under) of the instrument resolution.

Other analyses carried out in different micro-areas did not reveal any significant element that could be associated to any trace element specific for a possible ore (Table 2). Apart from Fe and O, all the elements seem to constitute soil, and from the ratio of their concentration it

would be possible to establish only comparisons and hypotheses

Analyses on restricted areas with a particular microstructure are reported in order to furnish further comparative elements in the charts and the EDS values of the areas indicated in microphotos (Figs. 16, 17 and 18):

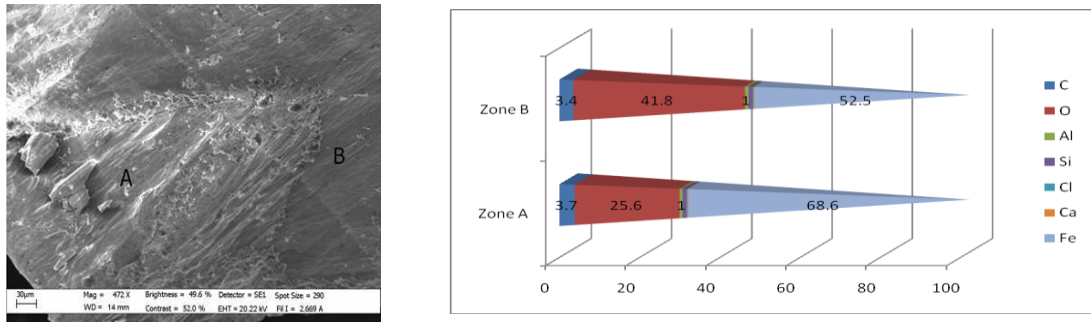


Figure 16 The investigated micro-areas and the EDS analysis values for each spectrum

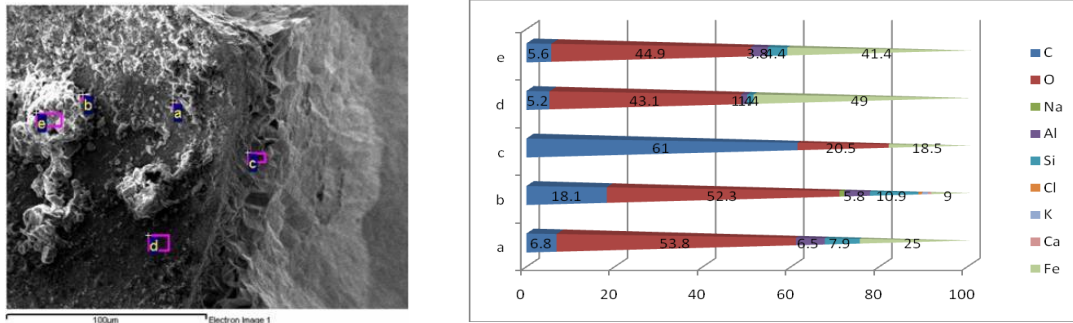


Figure 17: The investigated micro-areas and the EDS analysis values for each spectrum

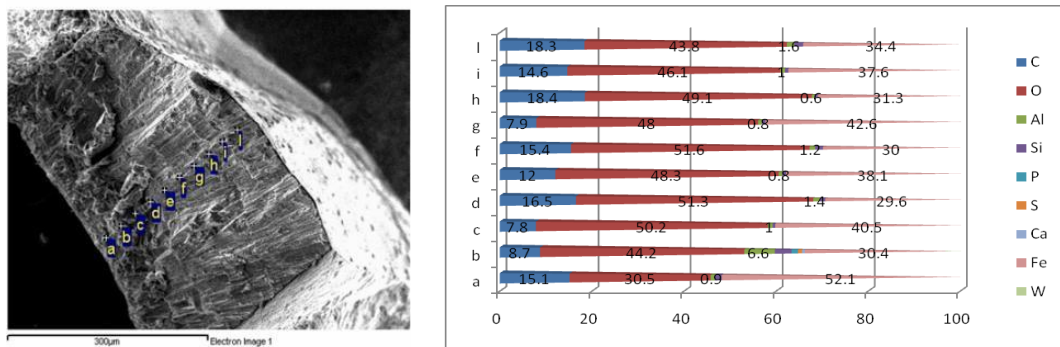


Figure 18: The investigated micro-areas and the EDS analysis values for each spectrum

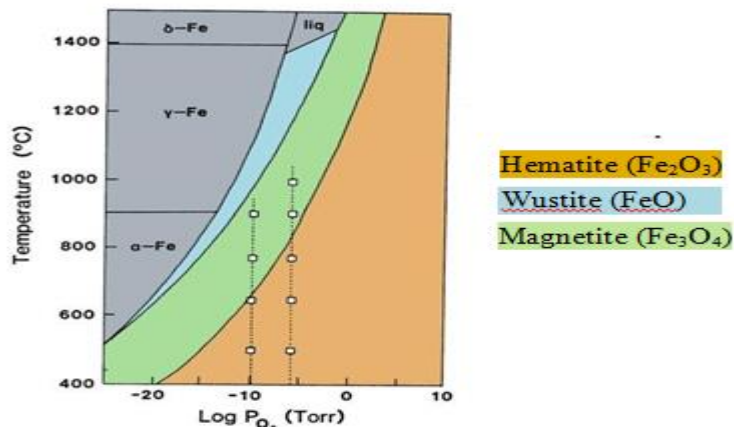


Figure 19: Iron Oxide (Fe-O) phase diagram as a function of temperature and pressure

From the EDS determinations the possibility appears reliable that the composition of the whole sample was a stable and stoichiometric iron compound. To have a confirmation of this, the Xray diffraction method was applied and the results indicate the existence of a single phase Fe₂O₃, hematite.

By considering the reported diagram of the system three Fe-O phases as existence as a function of temperature and pressure, it is possible to derive information about the condition of stability of the mineral (Fig. 19).

8. Sample 4

The sample represents a fragment of a hematite vein interbedded between the local ferruginous sandstone rocks exposed about 500 m northeast of the site along the Wadi Al Mataha. The sample was collected as a possible source of iron ore used by the Nabatean (Fig. 20).

The sample shows the domination of iron oxides with the presentation of Si, Mg, Mn and Al. The rich iron content of the sample with close mineralogical similarities to some slag samples and the close geographical location of the sample may suggest a suitable source for the iron within the Petra area. Other areas were not sampled at this stage of the research.



Figure 20. Sandstone bearing rich hematite veins exposed at the vicinity of the site. Naturally detached small fragments from the sample body allowed us to analyze the upper and the inner parts of the surface (Figs. 21 & 22) the results are summarized in Figure 23.



Figure 21. Digital photo Sample 4

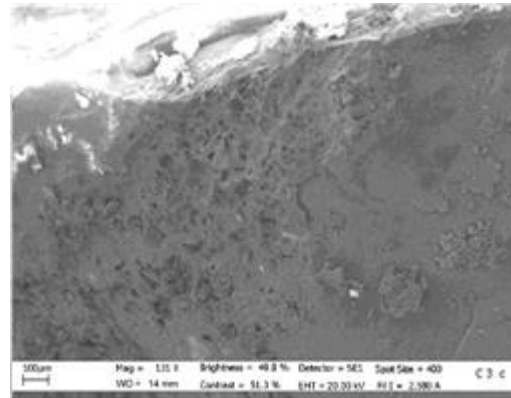


Figure 22. Enlargement of one fragment of sample 4

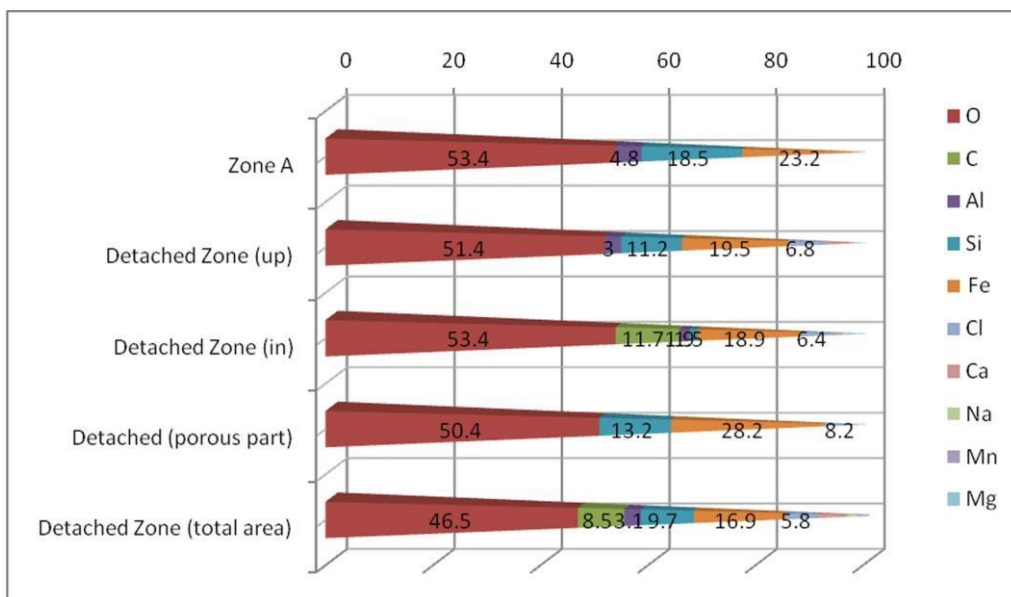


Figure 23. EDS Analyses of Various Fragments of Sample 4

9. Sample 5

Possible copper ore is found in abundance on the surface of the location sediments and has been differentiated for its completely inhomogeneous nature (Fig. 24a). Only spot analysis can be indicative for the nature of the compositing material. From the spectra it is possible to note the strong presence of copper and only from spot “9” small amount of Sn was revealed (microphoto in Fig. 24b).

Even in this case, the visualization of the dispersion of the main elements (Fig 25) can provide a preliminary overview of micro-areas to be investigated at higher

magnification for the individuation of elements as fingerprints of the whole sample. The EDS results exhibit a predominance of copper, but without a constant behavior as some parts of the sample might have been weathered. X-ray diffraction indicates the presence of quartz, cuprite and tenorite (Fig. 26).

By utilizing the correlation diagrams for the experimental results for comparing those with the common minerals containing the oxidation forms of Si, Ca, Al, it is possible to add some other elements of comparison for a more precise identification of the material’s composition (Fig. 27).

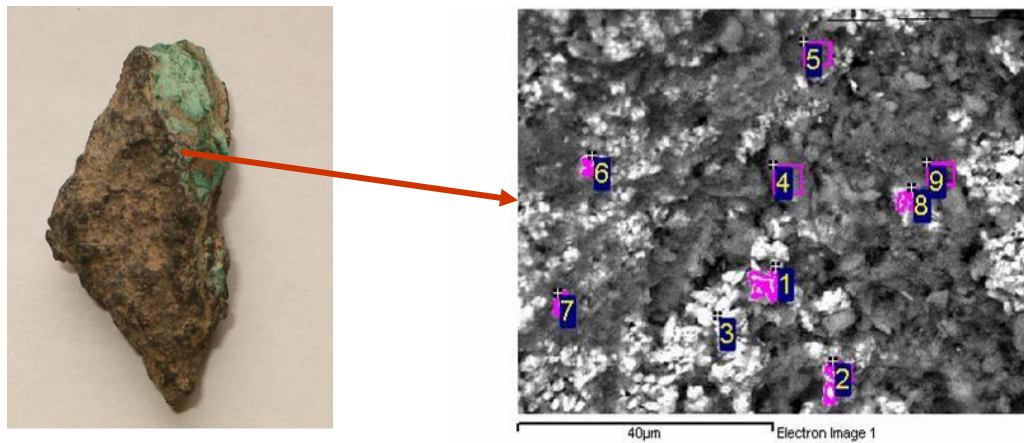


Figure 24. a Sample 5 and b- the enlarged micro-areas

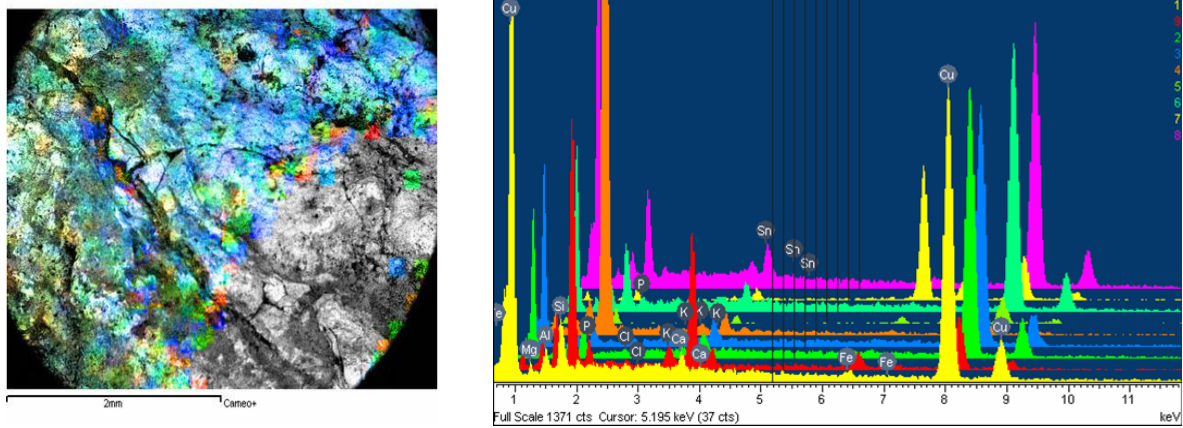
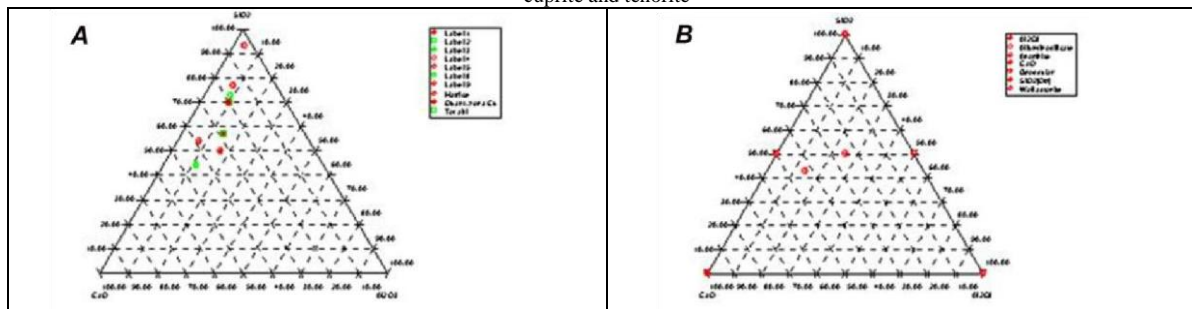


Fig 25. Distribution : Fe (blue) Figure 26: X-ray diffraction spectrum of Sample 5 Cu (sky) Ca (red) showing the presence of quartz, cuprite and tenorite



Common minerals in this System include: Quartz SiO_2 [Qtz], Corundum Al_2O_3 , Aluminosilicate Al_2SiO_5 , Wollastonite $CaSiO_3$ [Wo], Anorthite $CaAl_2Si_2O_8$ [An], Grossular Garnet $Ca_3Al_2Si_3O_{12}$ [Gr]

Figure 27. A - Correlation diagram for experimental data $SiO_2 - CaO - Al_2O_3$ and B - Three component system diagram $SiO_2 - CaO - Al_2O_3$ [24].

10. Sample 6

The archaeological sample is from a nail found at the Nabatean Winged Lion temple in Petra’s central area. The nail is about 5.5 cm long and completely corroded, it had a square section and was made from iron (Fig. 28). In the SEM microphotos, different states of iron degradation are represented. From its shape, it appears as a nail, and to verify this EDS analyses were carried out on the head, shaft and tip of the object (Fig. 28).

The sample shows a good presentation of Fe, O and Si (Fig. 29). This could be the result of weathering. The high percentages of O and Si elements with the presence of Mg show a close compositional similarity with that of the analyzed ferruginous sandstone. Therefore, a local source for some of the iron artifacts can be suggested at this stage of research.

This Nabatean coin was found on an erosional section southwest of the Winged Lion temple in the central area of

Petra. The coin is likely to be made of Bronze (Fig. 30). The piece is of green color on some areas because of copper corrosion (Figs. 31 & 32). The coin is completely covered by corrosion products and it is not possible to associate a real composition to the metallic alloy however, it was possible to observe zones on the sample, (Figs. 31, 32).

Only with superficial enrichments of the elements, separation of phase was achieved, but for the massive presence of Cu, Pb and Sn it is possible to realize the nature of the material as bronze as shown in the qualitative spectra of sample (Fig. 33).

The sample reveals a macrostructure with homogeneous crystals which the EDS analysis indicates as quartz crystals (Fig.32). The X-Ray diffraction revealed quartz, cuprite, and a mineral with aluminum silicate Al₂SiO₅ (Kyanite) (Fig. 33).

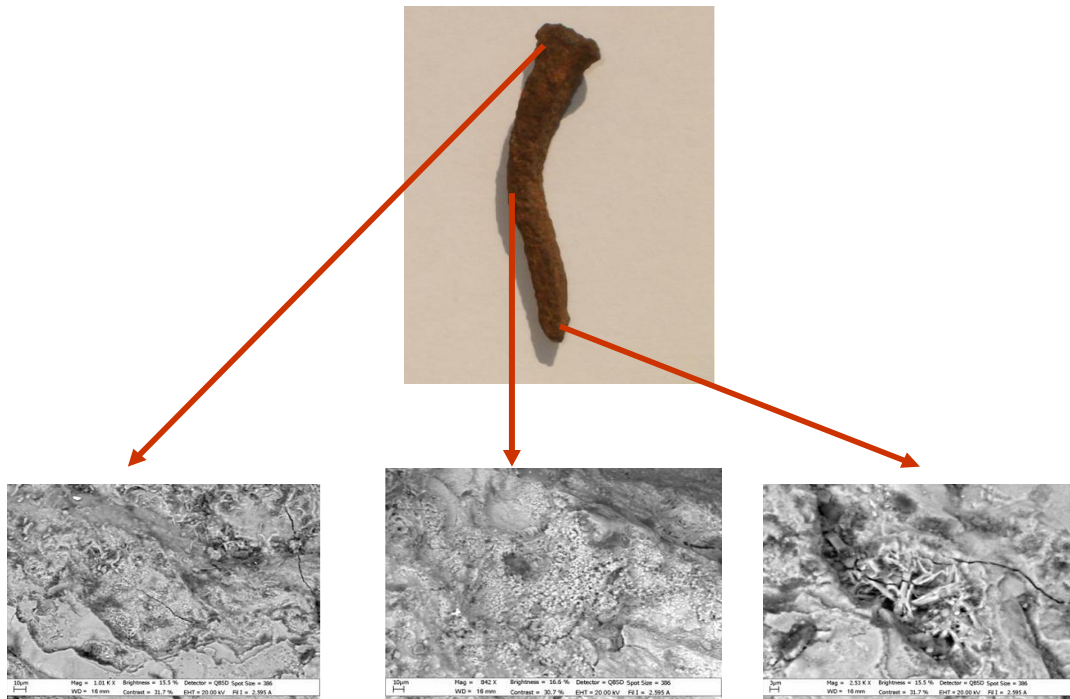


Figure 28. digital image and the SEM enlargements of the head, body and tip of sample 6

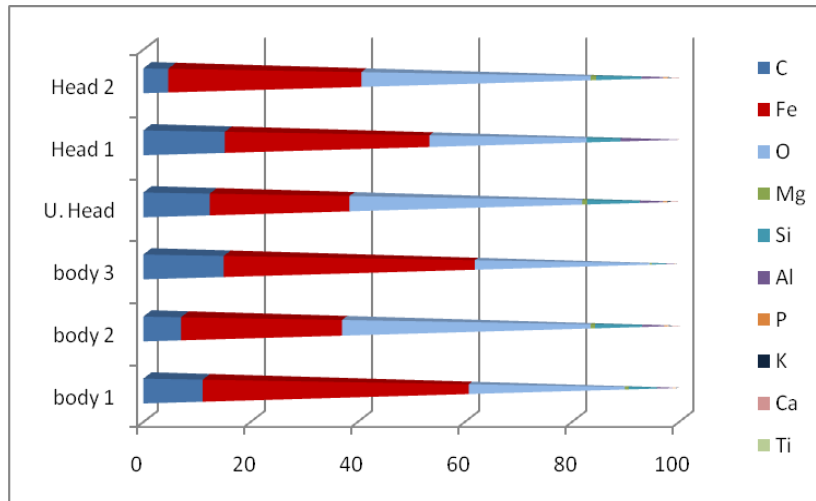


Figure 29 . EDS analysis values for each spectrum of the head, body and tip of sample 6 **Sample 7**

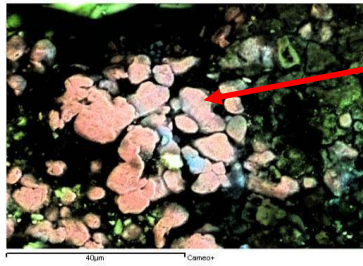


Fig 30. X ray -mapping of copper, red

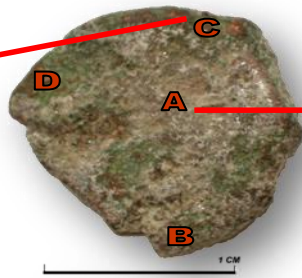


Fig 31. Ancient Nabatean coin

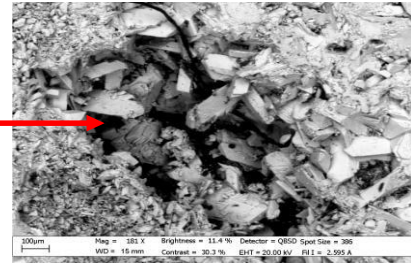


Fig 32. Pb crystals

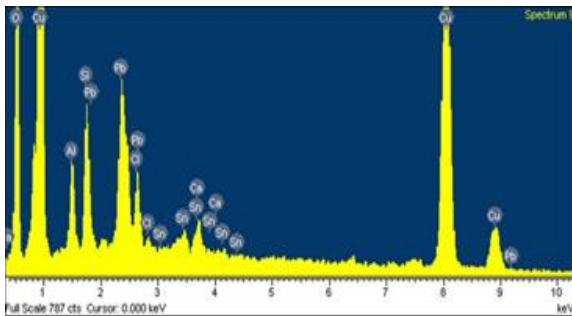


Figure 33: X-Ray diffraction spectra of Sample 7 shows strong presence of Cu, Pb and Sn, From the data summarized in Table 10, the attempt to determine the original composition of brass from the determination of the single element average concentration was performed, unfortunately, the advanced degradation state of the item allows only to point out a big amount of Pb in the alloy (Fig. 34)

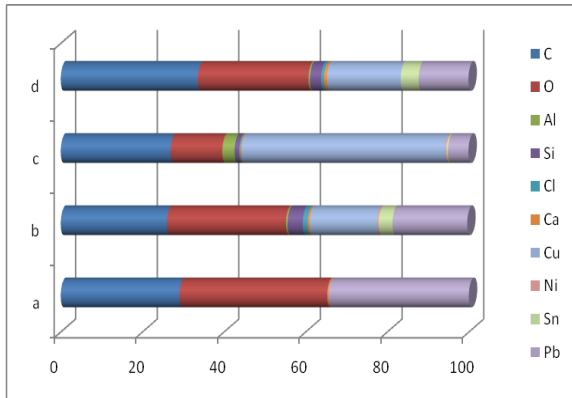


Figure 34: EDS analysis in areas of the dimension of 1 μ m of sample 7 showing high Pb value

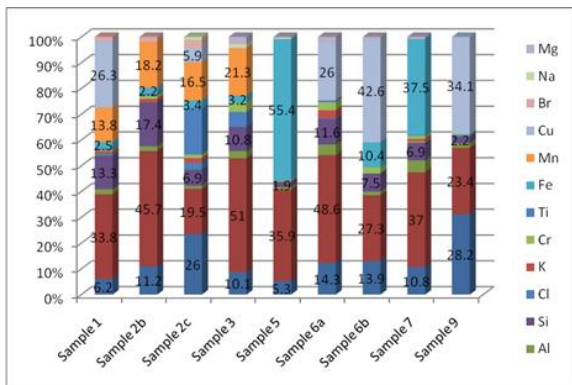


Figure 35. Summary of the chemical composition of the different analyzed samples

11. Discussion

Based on the observation and the analysis results of the investigated site and samples, the following conclusions may be drawn from the present study:

This preliminary approach to the study of the Petra's metallic findings can establish a useful background of knowledge for further investigations in different disciplines encouraging research to understand ancient metallurgy in Jordan. The analyses of the collected slag samples from this location in Petra suggest that the samples were derived from *in situ* smelting of iron and copper ores. This is the first evidence of Nabatean smelting in Jordan. Each sample yielded specific results not only about its nature, but also about its formation history. Some composition values with their constancy in the samples seem to adhere to a well-defined compound presence, but the punctual and zonal investigations suggest inhomogeneity and dishomogeneity of the sample matrix. This also found to be true due to either different processing stages or different preservation conditions of the samples.

Probably the analysis of more and well stratified samples combined with the other actual evidences, can give a more integral image of the Nabatean metallurgical process. At this stage, the results obtained demonstrate the validity of the methodology applied, by considering each sample not in its unity but in all the small parts and each of them containing specific information. The significant presence of the Mg, Fe, Cu and K (Fig. 35) in most of the analyzed slag samples which match with the collected potential raw material samples from the local sandstone outcrop (exposed about 500 m northeast of the site along the Wadi Al Mataha) might indicate the use of the local material by the Nabatean to manufacture their metal objects.

These analyzed raw material samples-though they are indicative-they are still too limited and not covering all the potential metallurgical aspect of the geographic area of the Petra area, and do not allow a general treatment of the matter especially with respect to the copper source. Therefore, copper ore needs to be further researched and more samples need to be collected from expected potential sources in-site and off-site.

This study needs to be proceeded with an archaeological excavation in the coming future to conform the nature of metalworking on the site and more samples needed to be analyzed to further our understanding of the Nabatean metal technology.

Finally, considering all the results obtained, an analytical lecture of the results can propose a reliable answer of the question previously proposed on the source of metal, and to contribute to the understanding of the Nabatean culture and related social and technological behavior.

Reference:

- [1] Hauptmann, A. (1986) Archaeometallurgical and Mining-Archaeological Studies in the Western Arabah, Faynan Area, 2ed Season. *Annual of the Department of Antiquities of Jordan (ADAJ)* Vol 45 pp. 159 -187. Amman Jordan.
- [2] Levy, Thomas, Russel B. Adams, Alan J. Witten, James Anderson, Yoav Arbel, Solomon Kuah, John Moreno, Angela Lo and Mark Wagonner (2001). Early Metallurgy, Interaction, and Social Change; the Jabal Hamarat Fidan (Jordan) Research Design and 1998 Archaeological Survey: Preliminary Report, *Annual of the Department of Antiquities of Jordan (ADAJ)* Vol. 45: 159 -187. Amman, Jordan
- [3] Siran Liu, Thilo Rehren, Ernst Pernicka, Arnulf Hausleiter, Copper Processing in the Oases of Northwest Arabia: Technology, Alloys and Provenance, *Journal of Archaeological Science* 53 (2015) 492-503.
- [4] Akasheh, T., (ed) 2004 Final Report of the Effect of the Weathering on Petra
- [5] Monuments, Submitted to Higher Council for Science and Technology, Amman, Jordan.
- [6] Brunnow, R. and Domaszewski, Von. (1904,1905); "*Die Provincia Arabia*", Vol I&II, Strasburg
- [7] Bachmann, H. G. (1980). Early copper smelting technique in Sinai and Negev as deduced from slags. Investigations. In P. T. Carddock (Ed.), *Scientific Studies in early mining and Extractive Metallurgy*, pp. 103-134. British Museum Occasional Paper No. 20, London.
- [8] Craddock, P. T. (1980). The composition of Copper Produced at the ancient smelting camps in the Wadi Timma, Israel. In P. T. Carddock (Ed.), *Scientific Studies in early mining and Extractive Metallurgy*, pp. 165-173. British Museum Occasional Paper No. 20, London.
- [9] Zwicker, V., P. virdis and M. L. Ceruti, (1980). Copper slag and copper ingots from Sardinia, In P. T. Carddock (Ed.), *Scientific Studies in early mining and Extractive Metallurgy*, pp. 135-164. British Museum Occasional Paper No. 20, London.
- [10] Bchmann, H. G. (1982), *The identification of slags from archaeological sites*. London, Institute of Archaeology, Occasional Publication 6.
- [11] Hauptmann A. (2014) The Investigation of Archaeometallurgical Slag. In: Roberts B., Thornton C. (eds) *Archaeometallurgy in Global Perspective*. pp 91-105. Springer, New York, NY Hammond, P.C. (1973), "*The Nabateans- Their History, Culture and Archaeology*", Paul Astroms Forlag, Sweden. 70-71
- [12] Hammond, P.C. (1964), The Excavation of the Main Theater at Petra. *Annual of the Department of Antiquities of Jordan (ADAJ)* Vol. 9: 81 -85. Amman, Jordan. 83.
- [13] Hammond, P.C. (1973), "*The Nabateans- Their History, Culture and Archaeology*", Paul Astroms Forlag, Sweden. 70-71
- [14] Hammond, P.C. (1982), "*The Excavation at Petra*". Studies in the History and Archaeology of *Jordan (SHAJ)* Vol. 1: 231 -238. Amman, Jordan.
- [15] Kolb, B., Keller D., and Felmann Brogli, R. (1997). Swiss-Liechtenstein Excavations at Az-Zantur / Petra: The Seventh Season, *Annual of the Department of Antiquities of Jordan (ADAJ)* Vol. 41: 231-254.
- [16] Stucky, R. A., Kolb, B. and Schmid, S.G. (1995) Swiss-Liechtenstein Excavations at AzZantur in Petra 1994: The Sixth Campaign. *Annual of the Department of Antiquities of Jordan (ADAJ)* Vol. 39: 297-315. Amman, Jordan.
- [17] Lindner, M. (1992). Survey of Sabra (Jordan) 1990: Preliminary Report. *Annual of the Department of Antiquities of Jordan (ADAJ)* Vol. 36: 39-216.
- [18] Kennedy, Sir A (1925); "*Petra, its History and Monuments*", Country Life, London.
- [19] Browning, Ian (1980); "*Petra*", Chatto & Windus, London.
- [20] Bovani Stefano, Luigi Campanella, Daniela Ferro, Bilal Khrisat, Talal Akasheh, (2006) Contributo chimico analitico nell'individuazione di officine metallurgiche a Petra (III a.c.) attraverso l'interpretazione di reperti ferrosi in *ESTRATTI Archeometria Atti*. IV pp. 579 – 591.
- [21] Campanella, L., D. Ferro, S. Bovani, B. Khrisat, T. Akasheh, (2007), Scientific approach to the comprehension of Petra Ancient Metallurgy. In the *Proceeding of the Second International Conference on Science and Technology in Archaeology and Conservation (December, 7-12, 2003, Jordan)*, T.S. Akasheh (ed.), Pp. 151 – 170. Fundacion El legado andalusi, Spain
- [22] Harald Alexander Veldhuijzen (2003) 'Slag Fun' – A New Tool for Archaeometallurgy: Development of an Analytical (P)ED-XRF Method for Iron-Rich Materials, *Papers from the Institute of Archaeology* 14 (2003): 102-118
- [23] Bedini A., Ferro D., Rapinesi I.A (1999); "*Gold Ornaments of Reticula*": *Microanalytic Research*" 6th International Conference on "Non-Destructive Testing and for the Diagnostic and Conservation of the Cultural and Environmental Heritage, Vol. II, pp. 1361-1379.
- [24] Ferro D., D'Alessio L., Tossini D. (2003), "*Scientific diagnostic methodologies for the characterisation of ancient goldsmith technology*", ARCCCHIP Workshops. ARIADNE 12-15 June (2003) pp 23-29.
- [25] Rostoker W. Bronson B., (1990). *Ferro Pre-Industriale, la sua Tecnologia e Etnologia, Archeomaterials*. Monografia 1 Filadelfia.



الجامعة الهاشمية



المملكة الأردنية الهاشمية

المجلة الأردنية
للمهندسة الميكانيكية والصناعية

JJIMOE

مجلة علمية عالمية محكمة
تصدر بدعم من صندوق البحث العلمي

<http://jjmie.hu.edu.jo/>

ISSN 1995-6665

المجلة الأردنية للهندسة الميكانيكية والصناعية

مجلة علمية عالمية محكمة

المجلة الأردنية للهندسة الميكانيكية والصناعية: مجلة علمية عالمية محكمة الجامعة الهاشمية تصدر عن بالتعاون مع صندوق دعم البحث العلمي والابتكار - وزارة التعليم العالي والبحث العلمي في الأردن.

هيئة التحرير

رئيس التحرير

الأستاذ الدكتور محمد سامي الأشهب

مساعد رئيس التحرير

الدكتور احمد المقدادي

الدكتور مهند جريسات

الأعضاء

الأستاذ الدكتور طارق العزب

جامعة البلقاء التطبيقية

الاستاذ الدكتور محمد الوديان

جامعة العلوم والتكنولوجيا الاردنية

الاستاذ الدكتور جمال جابر

جامعة البلقاء التطبيقية

الاستاذ الدكتور محمد تيسير هياجنه

جامعة العلوم والتكنولوجيا الاردنية

الأستاذ الدكتور محمد الطاهات

الجامعة الاردنية

الدكتور علي جوارنه

الجامعة الهاشمية

فريق الدعم

المحرر اللغوي

الدكتور بكر محمد بني خير

تنفيذ وإخراج

م . علي أبو سليمة

ترسل البحوث إلى العنوان التالي

رئيس تحرير المجلة الأردنية للهندسة الميكانيكية والصناعية

الجامعة الهاشمية

كلية الهندسة

قسم الهندسة الميكانيكية

الزرقاء - الأردن

هاتف : 00962 5 3903333 فرعي 4147

Email: jjmie@hu.edu.jo

Website: www.jjmie.hu.edu.jo